Master's thesis

NTNU
Norwegian University of Science and Technology
Faculty of Natural Sciences
Department of Materials Science and Engineering

Maren Valestrand Tjønneland

Optimizing Microalgae Biomass Production; Using Nanomaterials for Enhanced Light Transport

Master's thesis in Chemical Engineering and Biotechnology
Supervisor: Hilde Lea Lein
Co-supervisors: Matilde Skogen Chauton, Sidsel Meli Hanetho
July 2020

NTNU
Kunnskap for en bedre verden

Maren Valestrand Tjønneland

Optimizing Microalgae Biomass Production; Using Nanomaterials for Enhanced Light Transport

Master's thesis in Chemical Engineering and Biotechnology
Supervisor: Hilde Lea Lein
Co-supervisors: Matilde Skogen Chauton, Sidsel Meli Hanetho
July 2020

Norwegian University of Science and Technology
Faculty of Natural Sciences
Department of Materials Science and Engineering

NTNU
Norwegian University of
Science and Technology

Abstract

The low light utilization of current photobioreactors represents a major challenge in making industrial production of microalgae economically feasible. To improve the volumetric efficiency and thereby the economics of microalgae biomass production, using nanomaterials to enhance the light transport inside such systems seems to be a promising strategy. This study investigates the effect of using either silica or silver nanoparticle suspensions as a scattering medium to promote microalgal growth. Spherical silica NPs with mean diameters of 95 ± 11 nm, 192 ± 24 nm and 256 ± 40 nm have been synthesized by the Stöber method. Absorbance measurements demonstrated increased scattering of light with shorter wavelengths and higher scattering efficiencies for larger sizes and NP concentrations. Colloidal silver prepared by the Lee-Meisel citrate method displayed strong scattering of light in the blue region. After studying the synthesis procedure, quasi-spherical silver NPs were obtained with a mean size of 57 ± 14 nm and a localized surface plasmon resonance at 431 nm. Growth experiments were conducted in a photobioreactor consisting of a Multi-Cultivator from PSI adapted to allow for NP implementation. Cultivation vessels were constructed to have an enclosed compartment containing the NP suspension surrounding the algal cultures. As a model organism, the marine microalgae *Rhodomonas baltica* was used. The following combinations of silica NP sizes and concentrations were tested; 7217 mg/L of 95 nm, 40 mg/L and 160 mg/L of 192 nm and 40 mg/L of 256 nm. Suspensions containing 4 mg/L and 20 mg/L of 57 nm silver NPs were also studies. No positive effect on biomass production could be observed in either of the growth experiments.

Sammendrag

Den lave utnyttelsen av lys i nåværende fotobioreaktorer er en stor utfordring når det kommer til å gjøre industriell produksjon av mikroalger økonomisk lønnsomt. En lovende strategi for å forbedre den volumetriske effektiviteten, og dermed lønnsomheten, til biomasseproduksjon fra mikroalger, kan være å bruke nanomaterialer for å forbedre lystransporten i slike systemer. I denne masteroppgaven har effekten av å bruke løsninger med silica- eller sølv-nanopartikler for å fremme god algevekst blitt undersøkt. Sfæriske silica nanopartikler med en gjennomsnittlig diameter på 95 ± 11 nm, 192 ± 24 nm og 256 ± 40 nm har blitt fremstilt ved Stöber-metoden. Absorbansmålinger viste sterkere lysspredning ved kortere bølgelengder og økt spredning for større partikler og høyere konsentrasjoner. Kolloidalt sølv fremstilt ved Lee-Meisel metoden ga sterk spredning av blått lys. Etter å ha studert synteseprosedyren, ble kvasi-sfæriske sølvpartikler oppnådd med en gjennomsnittlig størrelse på 57 ± 14 nm og lokalisert overflate-plasmonresonans ved 431 nm. Vekstforsøk ble utført i en fotobioreaktor bestående av en Multi-Cultivator fra PSI, tilpasset for å muliggjøre implementering av nanopartikler. Dyrkningskar ble laget slik at nanopartiklene ble tilsatt i et eget, lukket rom som omringet algene. Den marine mikroalgen, *Rhodomonas baltica*, ble brukt som modellorganisme. Følgende kombinasjoner av silica nanopartikkelstørrelser og -konsentrasjoner ble testet; 7217 mg/L med 95 nm, 40 mg/L og 160 mg/L med 192 nm og 40 mg/L med 256 nm. Løsninger med 4 mg/L og 20 mg/L av sølvpartikler på 57 nm ble også undersøkt. Ingen positiv effekt på biomasseproduksjon ble observert i noen av vekstforsøkene.

Preface

This master's thesis is the result of work carried out by the author during the spring of 2020, the last semester of a 5-year Master's degree program in Chemical Engineering and Biotechnology at the Norwegian University of Science and Technology (NTNU).

The work was performed at the Department of Materials Science and Engineering as a part of the Functional Materials and Materials Chemistry Research Group (FACET). Associate Professor Hilde Lea Lein has been the main supervisor. The work has been supported by SINTEF Ocean AS with Senior Research Scientist Matilde Skogen Chauton and by SINTEF Industry with Research Scientist Sidsel Meli Hanetho as co-supervisors.

All of the experimental work was performed by the author, except for X-ray diffraction measurements performed by Senior Engineer Kristin Høydalsvik Wells.

Acknowledgements

The work with this master's thesis has been both challenging and inspiring and I am grateful for the opportunity to work on this particularly interesting topic. Overcoming hindrances encountered during this semester would not have been possible without the help and support from the people around me. First of all, I would like to extend my gratitude to my main supervisor, Associate Professor Hilde Lea Lein. I very much appreciate your feedback, encouragement and guidance throughout the work on this thesis. Secondly, I would like to pay my special regards to my co-supervisor, Senior Research Scientist Matilde Skogen Chauton, for your extensive knowledge and uplifting spirits. Without your help and feedback, the goal of this work would not have been realized. I also want to express my greatest appreciation to my co-supervisor, Research Scientist Sidsel Meli Hanetho, for your advice and valuable insights.

I would also like to thank all of the people who have provided me with instrument training, laboratory equipment, or contributed to my work in other ways. For constructive criticism and helpful feedback, I want to thank the members of the FACET group. Lastly, I want to thank my fellow students for replenishing coffee breaks throughout the work on this thesis and for their invaluable support.

Table of Contents

List of Tables

List of Figures

Abbreviations

ENM = Engineered nanomaterial
ENP = Engineered nanoparticle
FESEM = Field emission scanning electron microscopy
FWHM = Full width half maximum
LED = Light emitting diode
LSPR = Localized surface plasmon resonance
NP = Nanoparticle
PAR = Photosynthetically active radiation
PBR = Photobioreactor
RPM = Revolutions per minute
PVP = poly(vinylpyrrolidone)
RWP = Raceway pond
SD = Standard deviation
SEM = Scanning electron microscopy
TEOS = Tetraethyl orthosilicate
TSC = Trisodium citrate
SPR = Surface plasmon resonance
UV = Ultraviolet
VIS = Visible

1. Background

1.1 Motivation

In the recent years, considerable attention has been directed towards microalgae as a sustainable resource with a vast variety of applications [1]. Through photosynthesis, microalgae can convert solar energy into biomass and oxygen whilst fixating CO_2 from the atmosphere. Depending on the species, different compounds such as proteins, carbohydrates and lipids can be produced. As of today, commercial plants are mainly producing microalgae for use as pharmaceuticals, dietary supplements, animal feed and aquafeed, as well as for other high value products [2, 3, 4]. In addition, microalgae have been proven useful for wastewater treatment [5]. Biomass from microalgae can also be processed into biofuel, providing us with a renewable and potentially carbon neutral energy source [6, 7]. Whilst this idea has been known for decades [8], it is becoming a more widely discussed topic due to the increasing concern about climate change associated with the burning of fossil fuels [6]. Compared to other biofuel sources including plant and vegetable oils such as palm oil and oil derived from corn, soybean and canola crops, microalgal biofuel also has some important advantages. Due to the rapid growth and high oil content of many microalgae species, they have the potential of reaching much higher oil yields than what can be achieved with oil crops [6]. Microalgal biomass production also requires substantially less agricultural land than what is needed to harvest oil crops for biofuel use. Thus, the competition with the food industry as well as other consequences of land use, such as deforestation, degradation of ecosystems and loss of the services they provide, can be minimized [9]. As of today, however, algal fuel is generally more expensive than its alternatives and not an economically competitive energy source [6, 10].

Light-driven microalgae seem to be an attractive resource with potential of meeting the increasing global demand for basic needs such as energy, food and clean water. There is, however, one major bottleneck hindering the industrial growth of microalgae biomass production. Poor light transport inside cultivation systems is contributing to a low light utilization efficiency and thus low biomass productivity [11]. Due to scattering and absorption of light by the algal cells, an inhomogeneous light distribution inside the culture is established. This leads to reduced photosynthetic activity of algae deeper within the microalgae suspension as a result of low light availability. Conversely, supersaturation of cells that are exposed to high light intensities can cause photoinhibition [12]. The resulting poor volumetric efficiencies of cultivation systems puts a large economic constraint on the microalgae industry [13]. Strategies to increase the light utilization and thereby the productivity of microalgae are therefore crucial in order to make microalgae-based industries economically feasible [3, 14].

Some approaches to improving the light-to-biomass conversion in microalgae cultivation include optimization of photobioreactor designs and their mixing and illumination regimes [15, 16]. Other important tools involve selective breeding or genetic modification of algae [14]. Mutant cells with less light-harvesting chlorophyll have, for example, been shown to give a reduced shading effect and greater photosynthetic efficiency under bright illumination [17]. The application of light modulating devices and materials has also been deemed a promising solution. When immersing light guiding fibers into a microalgae suspension, Wondraczek et al. [18] demonstrated a significant increase in reproduction rate due to a larger fraction of illuminated volume. Recent advances in the field of nanotechnology also offer promising light modulating and enhancing methods based on the unique properties of engineered nanomaterials (ENMs) [19]. One approach is to use structures with nanosized patterns to enhance light of certain wavelengths. Inspiration for this can be found in nature, such as in the frustules of diatoms, a skeleton encapsulating the cells of these photosynthetic microalgae. The frustules are made of nanopatterned biosilica and have been reported to enhance certain wavelengths as well as display light trapping properties [20]. The optical properties of plasmonic metal NPs such as silver and gold have also gained considerable attention. When used in wavelength-selective light filtering or backscattering devices, enhanced microalgal growth and altered cell composition and has been reported [21, 22, 23, 24]. Applying waveguides doped with nanoscale organosilicone particles to scatter and redistribute the incident light has also been shown to improve biomass production by 220% [11]. Another nanomaterial known for its light scattering properties is spherical silica NPs [25, 26]. By immersing a tubular PBR in a scattering medium containing silica NPs, a 23% net increase in the final chlorophyll concentration was reported by Giannelli and Torzillo [27]. The silica NP suspension was shown to effectively dilute the incident light, reducing the risk over oversaturation.

Even though enhanced biomass production when using silver or silica NPs already has been documented, the research on this topic is still in its early stages. Especially for the application of silica nanospheres to improve light distribution, the research is limited. To the author's knowledge, only one study, by Giannelli *et* al. [27], implementing silica scattering centers to a microalgae cultivation system has been conducted. In that study, only one particle size was tested, hence the effect of NP size on biomass production is still insufficiently explored. To optimize microalgae biomass production, a better understanding of the optical properties achieved with different nanomaterials as well as NP sizes and concentrations is important.

1.2 Aim of the work

The aim of this work is to synthesize nanoparticles with light enhancing and modulating properties and to evaluate their effect on microalgae biomass production. When implemented to a microalgae cultivation system, the goal is to achieve improved light utilization and higher biomass productivity. In this master's thesis, two different nanomaterials will be studied, namely silica and silver NPs. Absorbance measurements will be used to evaluate the optical properties of the particles, and any effect on microalgae biomass production will be studied through growth experiments with the *Rhodomonas baltica* strain. Any observed effect on the photosynthetic efficiency or growth rate of the algae will serve as a biological indicator of the optical properties of the NPs. To perform the growth experiments, an experimental setup that allows for easy implementation of NPs to a photobioreactor is needed. One of the main objectives of this work will therefore be to design and develop small-scale cultivation vessels and to evaluate their suitability for this application.

Suspensions containing spherical silica nanoparticles will be synthesized by the Stöber method and the size of the particles will be tuned by varying the synthesis parameters. Both the effect of particle size and particle concentration on the scattering properties will be evaluated. For the synthesis of colloidal silver, the Lee-Meisel method will be applied and the NP formation reaction will be studied. The size, size distribution and morphology of the particles will be characterized by field emission scanning electron microscopy (FESEM) and particle size analysis tools. Determination of the nanoparticle concentrations will be done by gravimetry. To confirm the composition and structure of the NPs, X-ray diffraction (XRD) measurements will be performed. During the growth experiments, algal growth and photosynthetic activity will be monitored by measuring changes in phycoerythrin and chlorophyll fluorescence as well as quantum yield and turbidity. As a direct measure of the cell concentration, cell counting analyses will be performed.

2. Introduction

2.1 Microalgae biomass production

2.1.1 Photosynthetic microalgae - an introduction

Microalgae is a highly diverse group of unicellular microorganisms that includes divisions such as diatoms, green algae, dinoflagellates and red algae [2]. They are mainly found in aqueous environments and are one of the oldest life forms on Earth. Through photosynthesis microalgae are able to convert solar energy and a carbon source into biomass and oxygen (O_2). When carbon dioxide (CO_2) is used as carbon source, microalgae can contribute to the reduction of atmospheric and water dissolved CO_2 through biofixation [28, p 1]. As a reflection of the genetic variability of microalgae, the biochemical diversity among them is astonishing. Depending on the species, different compounds including pigments, fatty acids and lipids, oils, hydrocarbons and bioactive compounds can be obtained [2]. The possibility of using microalgae as a renewable energy source by converting algal oils, or lipids, into biofuel has especially gained a lot of interest [3].

2.1.2 Microalgae growth

Unicellular organisms such as microalgae grow, or reproduce, by cell division wherein a single cell divides into two (or more) daughter cells [29]. In addition to light, water and a carbon source, algae also need nitrogen and phosphorus and other potentially essential nutrients to grow [1]. The average size of the algal cells may vary throughout its growth cycle, hence it is sometimes important to distinguish between cell concentration and cell density when discussing algae growth. Cell concentration is often defined as the number of individual cells per unit volume of a culture whilst cell density commonly refers to the dry weight of cells per unit volume [30]. The growth of a batch culture containing unicellular algae, or microalgae, is often divided into some general subsequent phases. Monod [30] defined six phases of growth, namely (1) the lag phase, (2) the acceleration phase, (3) the exponential phase, (4) the retardation phase, (5) the stationary phase and (6) the phase of decline or death. In the lag phase, little increase in cell density is observed. This lag in growth is a result of adaptive processes in the microalgae cells, such as enzymatic adaptation, when they are transferred to a new and nutrient rich medium. The growth rate then starts to accelerate and it reaches its maximum value in the exponential phase where it stays constant. This is a phase of unlimited growth, where the growth and division rate of the algae is solely determined by genetic factors. In this phase, the cell density increases exponentially giving a straight line when plotted on a logarithmic scale. After some time, the growth becomes limited by important factors such as nutrition and light, making the conditions unfavorable for algae growth [29]. The growth rate then starts to decrease in the retardation phase and becomes zero in the stationary phase, resulting in no change in cell density. Eventually, more and more cells start to die, and when the amount of dying cells exceeds the number of dividing cells, we enter into the sixth and last phase where a decline in cell density is observed. A representation of the six standard phases of growth is given in Figure 2.1, as adapted from Monod [30].

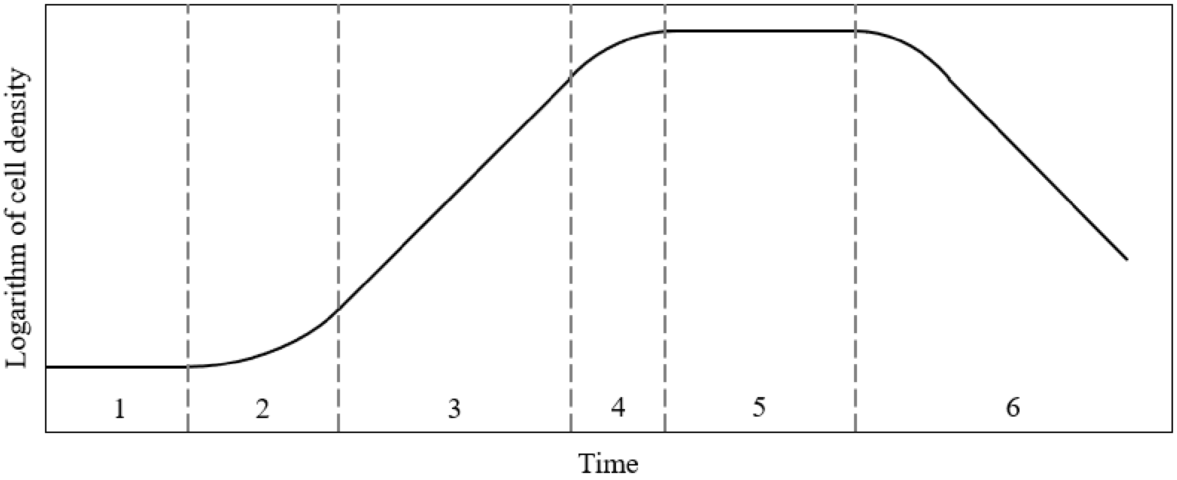

Figure 2.1: Growth curve of a batch culture presented by the logarithm of the cell density as a function of time, going through six phases; (1) lag, (2) acceleration, (3) exponential, (4) retardation, (5) stationary and (6) decline. Adapted from Monod [30].

Commonly, microalgae are able to double their biomass within 24 hours, or within as little as 3.5 hours during exponential growth. Compared to other crops harvested for e.g. biofuel use, their growth rates are extremely high, serving as one of the main advantages of utilizing microalgae for biomass production [6].

2.1.3 Photosynthetic efficiency

Photosynthetic efficiency is the fraction of light energy that is converted into biomass through photosynthesis by the algae or plant [3]. When incoming light reaches an algal cell, it is absorbed by wavelength selective light-harvesting pigments such as chlorophylls. The characteristic green color of chlorophylls stems from them mainly absorbing blue and red light [2]. Whilst Chl *a* is present in all algae, other chlorophylls act as accessory pigments that can be found in varying degrees in different algae groups. The light absorbed by chlorophyll molecules is either used to drive photosynthesis, dissipated as heat, or re-emitted as light (chlorophyll fluorescence). These are competing processes, hence measuring chlorophyll fluorescence can provide us with valuable information about the photochemistry efficiency and heat dissipation [31]. When subjected to stress, the ability of microalgae to metabolize normally can be reduced, resulting in an imbalance between energy absorbed and the energy used to drive photosynthesis. Hence, chlorophyll fluorescence can be used to measure stress in microalgae [31].

The photosynthetic efficiency is commonly given in terms of the quantum yield (QY), Φ, of photochemistry in photosystem II (PSII) and is defined as moles CO_2 absorbed (or oxygen released) per mole of photons absorbed during photosynthesis. Alternatively, the quantum yield can be defined as the ratio of the photosynthetically stored radiation (PSR) to the absorbed photosynthetically active radiation (PAR), ranging from 400 nm - 700 nm, as shown in Equation 2.1 [32].

$$\Phi = \frac{\text{moles CO}_2\text{ absorbed (O}_2\text{ released)}}{\text{moles photons absorbed}} = \frac{\text{PSR}}{\text{PAR}} \tag{2.1}$$

The quantum yield is related to fluorescence parameters through

$$\Phi = \text{qP}\frac{\text{F}_\text{v}}{\text{F}_\text{m}} \tag{2.2}$$

where qP is the photochemical quenching parameter indicating the proportion of the PSII reaction centers that are open [31]. When all centers are open, in the dark, the quantum yield is given by the ratio of variable to maximum fluorescence, $\text{F}_\text{v}/\text{F}_\text{m}$, also known as the intrinsic or maximum quantum efficiency [33]. For green microalgae the maximum values of the $\text{F}_\text{v}/\text{F}_\text{m}$ ratio generally ranges from 0.7 to 0.8 [34]. Lower values can be an indication of poorer photosynthetic performance as a result of the microalgae being subjected to unfavorable conditions such as high irradiance, extreme temperatures or nutrient limitations. Using a chlorophyll fluorometer provides a simple and non-destructive way of estimating the photosynthetic efficiency of organisms and is a widely used analysis technique. In addition to chlorophyll, other light-harvesting pigments such as carotenoids and phycobilins can be present in certain microalgae. The fluorescence of such pigments can also be studied when monitoring photosynthetic performance [35]. Measuring the total pigment yield of an algal culture is also used to monitor the growth and abundance of the algae.

2.1.4 The *Rhodomonas baltica* strain

Rhodomonas baltica is a red microalgae found throughout the North Atlantic ocean [36]. In addition to chlorophyll *a* they contain phycoerythrin (PE), a light harvesting pigment in the phycobilin family which gives it its characteristic red color [2]. Due to the high nutritional values of *R. baltica* it is commonly used as feed for zooplankton which is then fed to larval fish [37]. Its naturally high content of eicosapentaenoic acid (EPA) and docosahexaenoic acid (DHA) makes it a good source of unsaturated fatty acids important in aquafeed and human nutrition [37]. The nutritional benefits of *R. baltica* is especially prominent when grown under nitrogen limitations as it has been found to increase the lipid content in the microalgal cells. When going from moderate to strong N-limitation, *R. baltica* has been reported to nearly double its total lipid content [38]. After some time, however, nitrogen starvation decreases biomass productivity and eventually halts the cell division process [39]. When deprived of nitrogen, microalgae can start to mobilize their stored N-containing compounds, such as their photosynthetic pigments, as an adaptive response [40]. For *Rhodomonas sp.*, another alga in the *Rhodomonas* genus, almost a complete loss of PE was demonstrated when grown in a nitrogen lacking medium [41].

For the growth experiments in the present study, *R. baltica* was chosen due to its relatively easy cultivation and high growth rates. Being naturally occurring and non-toxic, it is also suitable for use in larger scale applications as potential leakages would not lead to the introduction of a foreign species into the ocean ecosystems. Other microalgae strains with suitable attributes could also have been applied for the purpose of this study, however, due to the interest of using *R. baltica* as aquafeed, it was conveniently available for use in this thesis.

2.1.5 Limits of microalgae productivity

There are several factors limiting microalgae productivity. Due to fundamental limits of photosynthesis, the overall maximum efficiency for converting solar energy into biomass is estimated to be $\sim$3% when excluding any practical losses such as reflection, inactive absorption and non-favorable conditions [3]. This partially stems from a poor spectral overlap of only $\sim$45% between the solar radiation and the photosynthetically active region. The light intensity also plays a major role in determining the efficiency of photosynthetic energy conversion. Only light with an intensity of up to 10% of full sunlight is used to drive photosynthesis in microalgae [3]. Higher irradiance values cause light saturation as the large number of light-harvesting pigments inside the algal cells absorbs more photons than what can be used to fix CO_2 [3]. The excess energy is dissipated either as heat or fluorescence whilst causing reversible damage to the photosynthetic apparatus through a phenomenon known as photoinhibition [12]. Excessive light will hence cause the specific growth rate of microalgae to decrease after the point of photoinhibition is reached [6]. Conversely, microalgae that are not sufficiently illuminated will not be able to carry out photosynthesis to the best of their abilities, also limiting biomass production. For dense algal cultures with a significant shading effect, this is a major limiting factor.

2.2 Microalgae cultivation systems

Microalgae cultivation systems are mainly divided into two main categories, namely open or closed systems. Open systems generally consist of a tank, pool or pond containing the algae culture that is widely exposed to air and the surrounding environment. Such systems offer poor control of the cultivation conditions and are easily contaminated, resulting in productivities on the lower end of the scale [7]. Still, open ponds have been the most widely applied cultivation systems used for commercial production of microalgae due to their simple configuration and easy operation [3]. One of the most sophisticated types of open pond systems are raceway ponds (RWPs) (Figure 2.2). In these systems, vertical mixing is provided by mechanically driven paddlewheels to circulate the algae from dark to light regimes, thereby limiting supersaturation and photoinhibition [42].

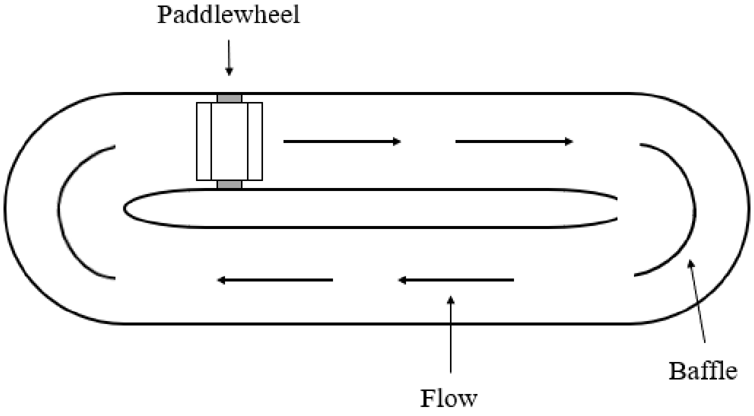

Figure 2.2: Schematic of a simple raceway pond with paddlewheel mixing. Adapted from Moreno-Garcia *et* al. [7].

Whilst being a vital part of RWPs, the high operating costs of paddlewheels present a major drawback [43]. Another challenge for open raceways is the evaporation of culture medium, increasing the already high water requirements of algal production systems. From a sustainability perspective, using marine species and seawater instead of freshwater algae is hence desirable [7].

Closed systems, or photobioreactors (PBRs), consist of an enclosed compartment made out of a transparent material, making them more suitable for implementation of nanoparticles. These systems are generally more complex and require a larger initial investment as well as more expensive maintenance [7]. In return, they offer better control of the cultivation conditions, less contamination, and higher biomass productivity. Compared to open RWPs, more than 13 times larger volumetric biomass productivity can be obtained when using PBR methods [6]. PBRs come in many different configurations including stirred tank reactors, column reactors, flat plate reactors and tubular reactors [15]. One of the most popular types of PBRs are cylindrical, vertical column PBRs where mixing is achieved by bubbling air or CO_2 into the algae culture, doubling as a carbon source (Figure 2.3a) [7]. Their simple design and low shear forces that cause minimal damage to the algal cells are some of the advantages of column PBRs. The main challenge remains in their low light utilization efficiency due to uneven light distribution [7]. Other commonly discussed PBR configurations are the tubular photobioreactors. These typically consist of an array of transparent tubes in which the microalgae culture is circulated by a turbulent flow generated by pumps. The tubes can be arranged in various ways and are orientated towards the light source to improve biomass production [44]. One configuration involves arranging horizontal, parallel straight tubes in a fence-like manner. The stacked tubes form a solar array, capturing energy from the sun, and are connected to a reservoir such as a degassing column (Figure 2.3b). To achieve a high surface-to-volume ratio and minimize light attenuation inside the culture, narrow tubes with a diameter of approximately 0.1 m or less are generally used [6].

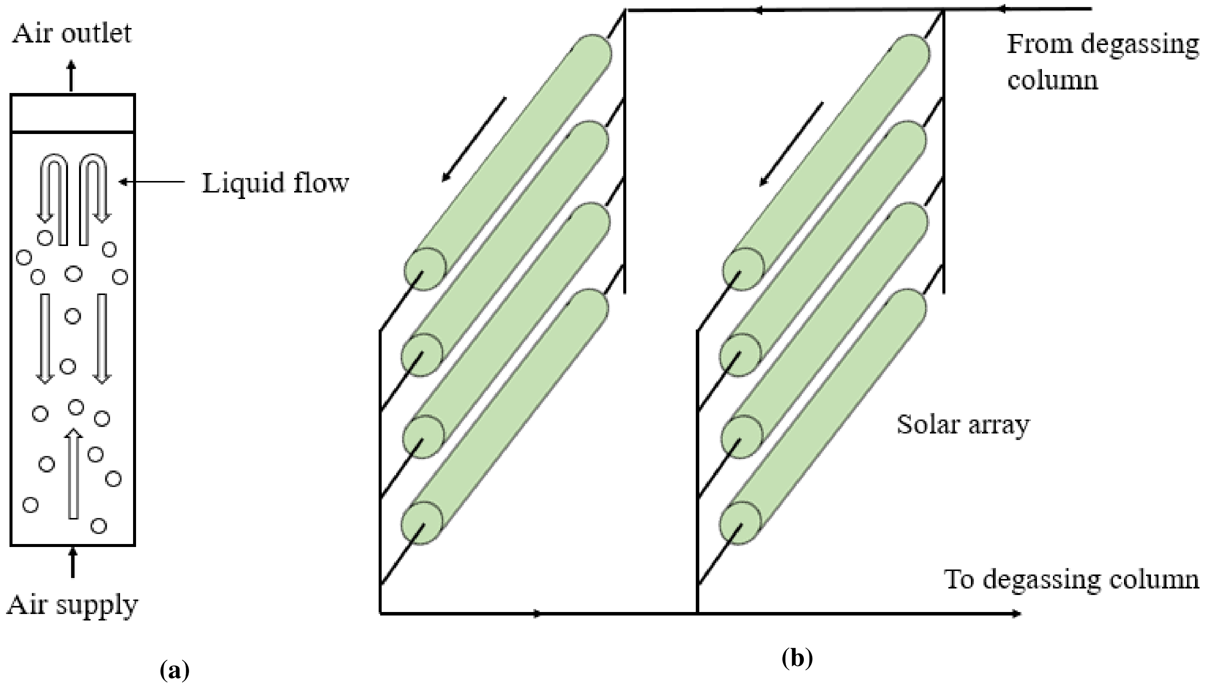

Figure 2.3: Schematic of two typical photobioreactors; (a) a column PBR with air bubbling, adapted from Moreno-Garcia *et* al. [7], and (b) a tubular PBR with fence-like arrangement, adapted from Chisti *et* al. [6].

Tubular PBRs appear to be promising in the scale-up of microalgae cultivation systems for industrial applications due to their higher photosynthetic efficiencies [15]. However, one of their main drawbacks is the uncontrollable growth of microorganisms on the inner tube walls, reducing light permeability [7]. This calls for regular cleaning of the tubes, which adds to the operating costs and can be difficult due to their small dimensions [45]. Another potential issue encountered with tubular PBRs is the accumulation of produced oxygen inside the tubes at high illumination intensities, which can lead to oxygen supersaturation and decreased productivity [46].

2.2.1 Light attenuation inside photobioreactors

One of the main factors dictating the illumination efficiency of microalgae cultivation systems is the photobioreactor design. For optimal biomass production, the PBR should be able to deliver light efficiently and homogeneously to even the darkest regions in the culture. When propagating through the reactor, the incident light is scattered and absorbed by the microalgae cells, causing light attenuation and a heterogeneous light distribution [35]. The light attenuation by biomass was demonstrated by the illumination profile inside a tubular PBR estimated by Fernández *et* al. [47]. The light penetration depth is highly dependent on the volume density of the microalgae species, and a too high algal density can result in oversaturation at the surfaces and little to no light availability at greater depths inside the reactor. To reduce this effect, mixing and agitation of the culture is commonly applied. Optimizing the geometry and design of the PBR is however predicted to play an even larger role in achieving efficient light delivery. The importance of homogeneous illumination to achieve high productivity inside large microalgae reactors with high cell densities has been demonstrated by Wondraczek *et* al. [18]. They reported an increase in algae reproduction rate of up to 93% when increasing the fraction of illuminated volume by immersing side-emitting optical fibers into the reactor medium.

2.3 Optical theory

This section provides an introduction to optical theory relevant to this topic. An identification of the relevant background material was carried by the author out in the project preceding this thesis [48]. A reviewed version of the presentation from the project report is included in the following sections 2.3.1 - 2.3.4.

2.3.1 Light

Light refers to electromagnetic radiation that is known to display wave-particle duality. When propagating through space it behaves in a wavelike manner, yet during processes like emission and absorption, it behaves similarly to that of particles. Quantum mechanics describes light as quantified elementary ”particles” with no mass, known as photons. In classical electrodynamics, however, light is described as a continuous transfer of energy by transverse electromagnetic waves represented by Maxwell’s equations [49, p 36]. The frequency, v, and wavelength, λ, of a wave is related to each other by

$$v = \frac{\lambda}{c}. \tag{2.3}$$

where c is the speed of light. The photon energy E is then related to the frequency through

$$E = hv \tag{2.4}$$

where h is Planck’s constant [49, p 67]. In the order of increasing frequency, the electromagnetic spectrum spans from radio frequency (RF) waves through microwaves, infrared (IR) radiation, visible light, ultraviolet (UV) radiation, X-rays and to gamma rays. The visible region consists of light with wavelengths ranging from approximately 390 nm (violet) to 780 nm (red). When a mixture of radiation with all wavelengths of the visible spectrum is present in a light beam, it appears white to the human eye [49, p 77].

2.3.2 The refractive index

Light which is passing through a homogeneous medium will undergo multiple scattering and rescattering processes, resulting in a phase shift. This is evident through the change in beam velocity and wavelength once inside the medium, compared to that outside [49, p 226]. This phenomenon, called refraction, is expressed by the real refractive index n, defined as the ratio between the speed of light in vacuum, c, and the speed of light in a given medium, v. It can also be expressed in terms of the wavelength in the medium, λ, and in vacuum λ_0:

$$n = \frac{c}{v} = \frac{\lambda_0}{\lambda} \tag{2.5}$$

In the case of light propagation through an absorbing medium a complex refractive index, m, can be defined by

$$m = n(1 - i\kappa) \tag{2.6}$$

where i is the imaginary unit and κ is the index of absorption, or alternatively the index of extinction [50, p 15]. The refractive index for all medium except vacuum is frequency-dependent, meaning that different colored light is refracted differently and will travel at dissimilar phase velocities and [49, p 67].

2.3.3 Absorption and scattering of light by particles

When light hits an obstacle such as a single electron, atom, molecule or particle, two optical processes known as absorption and scattering may occur. If the energy of the photon is equal to the energy required to excite an electron (or higher), the photon causes an electron to jump from its ground state to a higher energy level. The frequency corresponding to the excitation of an atom is commonly referred to as the resonance frequency. Upon absorption, the energy is rapidly converted into other forms such as thermal energy due to atomic motion and collisions. Scattering is a process where light is redirected from its original direction of propagation. Resonant scattering occurs when an electron is excited and immediately drops down to its ground state upon the emission of a photon. Non-resonant, or ground state scattering, can occur when the photon energy is too low to cause excitation of electrons. Instead, the electric charges of the obstacle are accelerated and set into oscillatory motion, generating electromagnetic waves that are emitted in all directions [49, p 67]. If the energy of the scattered light is equal to the incident photon energy, the scattering is said to be elastic. Light scattering can be further divided into other optical phenomena such as reflection, refraction and diffraction [51, p 3]. The combined effect of absorption and scattering is commonly referred to as extinction. To express the total energy that is abstracted from a beam due to extinction, an extinction cross section C_{ext} can be given by

$$C_{\text{ext}} = C_{\text{sca}} + C_{\text{abs}} \tag{2.7}$$

where C_{sca} and C_{abs} is the scattering and absorption cross section, respectively. Corresponding efficiency factors, Q, are obtained by dividing the respective cross section with the geometric cross section of the particle, which for a sphere is πr^2. The extinction efficiency becomes

$$Q_{\text{ext}} = \frac{C_{\text{ext}}}{\pi r^2}, \tag{2.8}$$

and similarly for scattering and absorption [50, p 50]. For a plane, monochromatic wave propagating in a homogeneous medium, the Beer-Lambert law states that the intensity, I, decreases over the path length L [mm] according to

$$I = I_0 \text{exp}(-\alpha_{\text{ext}} L) \tag{2.9}$$

where I_0 is the intensity of the incident light and α_{ext} [mm^{-1}] is the extinction, or the attenuation, coefficient. How effectively light of a specific wavelength is extinct is measured in terms of absorbance, A, defined as

$$A = log_{10} \frac{I_0}{I} = -log_{10} T. \tag{2.10}$$

closely related to the transmittance, T [52, p 348]. The absorbance of a particulate sample can be measured experimentally by spectrophotometry. Light emitted from a source hits the sample at a vertical angle and collected by a detector on the other end (Figure 2.4).

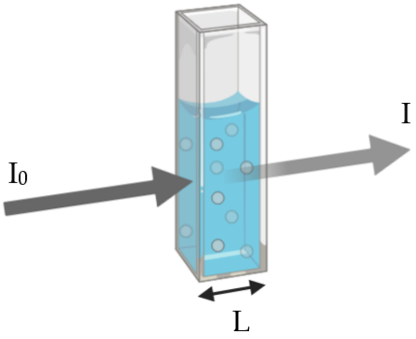

Figure 2.4: Illustration of light propagating through a particulate sample for absorbance measurements. Incident light with intensity I_0 is directed towards a sample with a path length L and transmitted light with intensity I is detected. Created with BioRender.

Absorbance by particulate samples can in principle be measured using the same type of spectrophotometers as for homogeneous liquids or solids. However, unless the detector is able to reject light scattered in the forward direction, forward-scattered light will contribute to the total transmission [51, p 316]. Analyzing absorbance measurements using equation 2.10 hence ignores the contribution from forward-scattered light [53].

2.3.4 Mie and Rayleigh theory

In Mie theory, elastic scattering of radiation by a homogeneous, isotropic sphere of arbitrary size is described. As explained by Hergert and Wriedt [54], the paper published in 1908 written by Gustav Mie [55] described a computational method for solving the scattering problem in the case of a spherical particle. The original Mie theory only applies to spheres in a non-absorbing ambient medium, such as a transparent solvent (e.g. water or ethanol) [54, p 57]. In Mie theory, scattering depends only weakly on wavelength and when for particle sizes larger than λ it becomes independent of it [49, p 226].

A limiting case of Mie scattering is Rayleigh theory, stating that the scattered irradiance by particles small compared to the wavelength is proportional to $1/\lambda^4$ [51, p 132]. Thus, smaller particles scatter light of shorter wavelengths more strongly than others, the phenomenon giving rise to the blue color of the sky. For convenience, a dimensionless size parameter, x, (often also denoted α) is introduced as

$$x = \frac{2\pi r}{\lambda} = \frac{\pi d}{\lambda} \tag{2.11}$$

where r is the radius of the sphere and λ is the wavelength in the medium. The upper limit for Rayleigh theory in terms of particle radius is generally set at r/$\lambda \leq$ 0.05, or alternatively in terms of particle diameter, d/$\lambda \leq$ 0.10 [50, p 37]. The stronger scattering at shorter wavelengths, or higher frequencies, can be explained by the energy of ultraviolet (UV) radiation being large enough to cause resonant scattering in most atoms. As the frequency approaches the resonant frequency when moving from yellow to violet light, the ground-state oscillations get stronger and the scattered intensity increases [49, p 67].

The angular distribution of light scattered by a sphere is also highly dependent on particle size. In fact, the sensitive relation between particle size and scattering properties makes measuring and comparing scattering patterns an accurate method for size-determination of spheres [51, p 384]. For unpolarized light, such as light from the sun or an LED lamp, the scattering pattern by particles in the Rayleigh regime is approximately isotropic [35]. In a simulation study on the use of TiO_2 scattering centres in dye-sensitized nanocrystalline solar cells, more symmetric light scattering for smaller particles (down to 50 nm in radius) was reported [56]. For particles with sizes approaching the wavelength of the incident light, more light is scattered in a forward direction and less is backscattered. Particle sizes in this range are said to be in the Mie regime [35].

2.4 The plasmonic effect

Metallic nanoparticles display unique optical properties, including a phenomenon known as the plasmonic effect. In this section, an introduction to this effect as well as some potential uses is presented.

2.4.1 Localized surface plasmon resonance

In metals, positively charged lattice ions are surrounded by negative valence electrons that are delocalized and free to move around within the material. Initially, the electron distribution is uniform but upon interaction with electromagnetic waves, the electric field causes displacement of the conduction electrons. A restoring force arising from the Coulomb attraction forces between the electrons and the nuclei will then cause the electrons to oscillate collectively, a phenomenon known as plasma oscillation [57]. The excitation of a plasma oscillation is also referred to as the generation of a plasmon, defined as a quantified plasma wave. The frequency of the collectively oscillating electron gas, or the plasma frequency, is given by

$$\omega_p^2 = \sqrt{Ne^2/m\epsilon_0} \tag{2.12}$$

where e and m are the electronic charge and mass, respectively, and ϵ_0 is the vacuum permittivity [58]. The number density of positive ions in the bulk is denoted N. Furthermore, the permittivity of the metal, ϵ, is related to the plasma frequency through the Drude formula

$$\epsilon(\omega) = 1 - \omega_p^2/(\omega^2 + i\gamma\omega) \tag{2.13}$$

where γ is a damping coefficient and i is the imaginary unit [58]. In bulk materials the plasma is unbounded whereas in small systems such as in thin films and spherical particles the collective oscillation of the electrons is affected by the boundaries of the system, and we talk about surface plasmon resonance (SPR) [51, p 255]. In the case of spherical metallic nanoparticles smaller than the wavelength of the incident light, the plasmons oscillate around the particle and are referred to as localized surface plasmons [59].

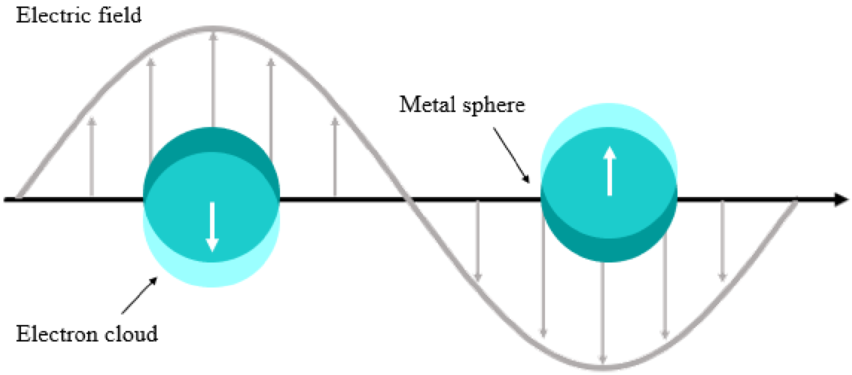

Figure 2.5: Schematic of the localized surface plasmon resonance in metallic spheres. Adapted from Willets and Van Duyne [59].

The frequency of such oscillations is known as the localized surface plasmon resonance (LSPR). When incident light hits a metal NP, the wavelengths in the region of the LSPR of the particle is strongly extinct, either by scattering or absorption, depending on the particle size. The strong extinction stems from the ability of small metal spheres to have absorption and scattering cross sections larger than their geometrical sizes. For particles sufficiently small compared to the wavelength, the absorption and scattering efficiencies are given by the approximation

$$Q_{\text{abs}} \simeq 4xIm\left(\frac{\epsilon - 1}{\epsilon + 2}\right) \tag{2.14}$$

$$Q_{\text{sca}} \simeq \frac{8}{3}x^4\left|\frac{\epsilon - 1}{\epsilon + 2}\right|^2 \tag{2.15}$$

where x is the size parameter and ϵ is the dielectric function. For free-electron metals with $\epsilon \simeq$ -2 at a certain wavelength, the denominator of equations 2.14 and 2.15 will approach zero and the cross sections will reach a maximum. The absorption and scattering cross sections can hence exceed the geometrical cross section even for particles with a small size parameter [51]. Whether the light is mostly absorbed or scattered highly depends on the size of the metallic sphere. For sizes much smaller than the wavelength of light, absorption tends to dominate whilst for increasing particle sizes scattering is the main mechanism [60]. A radiative efficiency, ρ can be defined as

$$\rho = \frac{C_{\text{sca}}}{C_{\text{sca}} + C_{\text{abs}}} \tag{2.16}$$

or equivalently in terms of Q_{abs} and Q_{abs}. The radiative efficiency approaches 1 for larger particles, indicating that they mainly scatter light [61].

The LSPR energy of a metal nanoparticle depends both on the density of free electrons within the conduction band and the dielectric medium surrounding it. The resonance frequencies of noble metal NPs such as Ag and Au lies within the visible part of the electromagnetic spectrum. This gives rise to the strong color of such metals and their colloidal dispersions, which has been an object of fascination amongst scientists for decades [62]. Small gold nanoparticles display LSPR in the blue-green region of the visible spectrum, giving them a red color [62]. Silver nanoparticles, on the other hand, have a yellow-brown color due to their LSPR in the violet-blue region [63].

2.4.2 Particle size- and shape-dependency of LSPR

The resonance frequencies of noble metal nanoparticles is highly size-dependent. With increasing particle volume the molar extinction coefficient has been shown to increase linearly [64]. For gold nanoparticles a red shift in the surface plasmon absorbance accompanied with a wider LSPR band was observed when increasing the particle size in the size region above 20 nm [64]. This is illustrated in Figure 2.6, displaying the absorbance spectra for spherical gold particles of 22, 48 and 99 nm when normalized at their absorbance maximum, as obtained by Link and El-Sayed [62] [64]. For particles very small compared to the wavelength (5 nm - 20 nm) only absorbance can occur, but for increasing particle sizes scattering becomes dominant and the peak broadens [65].

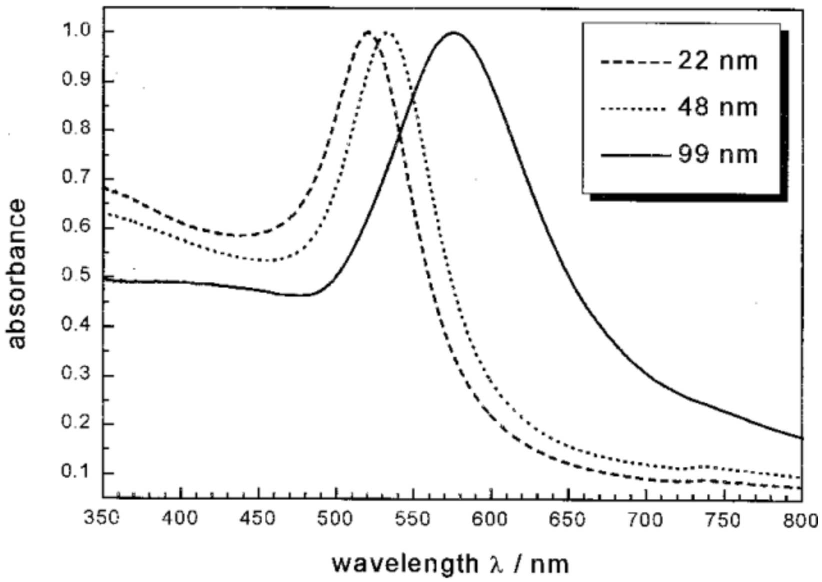

Figure 2.6: Surface plasmon absorbance of spherical Au NPs and its size dependency. Obtained for Au NPs with sizes of 22, 48 and 99 nm. Reprinted from Link and El-Sayed [62] with permission from Taylor & Francis.

The LSPR of nanoparticles is also very sensitive to the particle morphology. For aqueous dispersions containing silver quasi-spheres, cubes and triangular plates with sizes of 80 nm, the sensitivity is evident through the different extinction spectra obtained by Wiley *et* al. [66] (Figure 2.7).

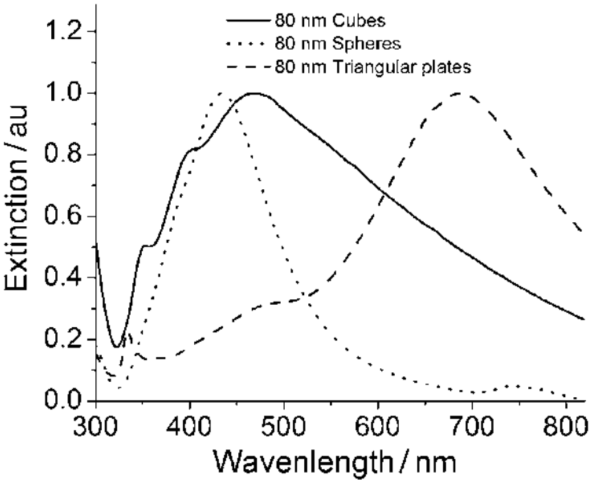

Figure 2.7: Extinction spectra of aqueous dispersions containing silver quasi-spheres, cubes and triangular thin plates with approximately the same lateral dimensions, normalized to the intensities of their strongest peaks. From Wiley *et* al. [66]. Reused with permission from John Wiley and Sons, Copyright © 2005 WILEY-VCH Verlag GmbH & Co. KGaA, Weinheim.

The quasi-spherical particles gave a single symmetric peak at 430 nm whilst an increasing number of SPR peaks were observed when the symmetry of the particles decreased. The cubic nanoparticles exhibited SPR peaks at 350, 400 and 470 nm and the spectra obtained with triangular nanoplates showed peaks at 335, 470 and 690 nm.

2.4.3 Utilizing plasmonic NPs in microalgae cultivation

The strong wavelength specific scattering of metallic NPs can be utilized for light trapping applications. Pillai *et* al. [60] demonstrated an increase in thin film solar cell efficiency when silver nanoparticles were deposited onto the silicon substrate. The efficiency gain was explained by the excitation of surface plasmons trapping the light, thereby increasing the light absorption of the cell. In microalgae biomass cultivation, wavelength selective backscattering of light from plasmonic nanomaterials has been shown to be a promising way to increase the productivity [21, 22, 23, 24]. Backscattering of blue light from Ag NPs caused by LSPR has been found to increase algal growth with more than 30% by Torkamani *et* al. [21]. Gold NPs have also been reported by Ooms *et* al. [23] to increase the growth rate of algae by effectively scattering red light. Whilst essentially functioning as a light reflecting mirror, utilizing the LSPR of metallic nanoparticles have an important advantage in that its properties can be tuned by controlling the size, shape and composition of the particles [67]. This ability to tailor metallic NPs to strongly scatter light intensities favorable for algae growth makes surface plasmon based light management a promising solution to improving PBR efficiency.

2.5 Colloidal chemistry

2.5.1 A brief introduction to colloidal systems

A colloidal system consists of particles with sizes ranging from 1 - 1000 nm dispersed in a continuous phase. Colloids have an extremely high surface-to-volume ratio and display deviating properties from ordinary solutions. When discussing solid particles dispersed in a liquid phase, a stable colloid is commonly referred to as a *sol*. Conversely, if the particles combine to form a continuous network throughout the liquid phase, it is known as a *gel* [68].

2.5.2 Colloid stability

As a way to reduce the total surface energy of a system, individual nanostructures tend to agglomerate due to chemical bonds and physical attraction forces at the interfaces. When formed, such agglomerates have been proven difficult to destroy and for practical applications formation of agglomerates should be prevented. Two main mechanisms are used to stabilize nanoparticles, namely electrostatic stabilization and steric stabilization [69, p 31,38].

Electrostatic stabilization

When a particle is dispersed in a polar solvent or an electrolyte, a surface charge density will be established, for example due to adsorption of charge determining ions onto the solid surface. An example of this the adsorption of citrate ions onto colloidal silver particles, acting as stabilizing agents [70]. This causes an electrostatic force to arise between the particle surface and the charged species in solution, resulting in a higher concentration of counter-ions in the proximity of the solid surface. Two particles approaching each other will therefore experience electrostatic repulsion, and when this force is larger than the Van der Waals attraction force, electrostatic stabilization is achieved [69, p 38].

Steric stabilization

In steric or polymeric stabilization agglomeration is prevented by attaching macromolecules to the nanoparticle surface. The adsorbed polymer layer acts as a diffusion barrier to the growth species in the solution and provides steric hindrance between two particles in close proximity [69, p 50]. A commonly used capping agent is poly(vinylpyrrolidone) (PVP), used for example as a capping agent to stabilize silver nanoparticles [66].

2.6 The sol-gel process

The state of the art and related work has been reviewed, and an identification of the relevant background material was carried out in the project preceding this thesis [48]. This section is adapted from the previous work as relevant new material was found during the work on the thesis.

The sol-gel process is a wet chemical route wherein a colloidal dispersion of particles, a sol, is created and subsequently converted to a viscous gel. It is a commonly used method used to synthesize metal oxide nanoparticles, such as silicon dioxide (SiO_2), or silica, and titanium dioxide (TiO_2). Generally, a metal alkoxide or salt precursor is mixed with a solvent and proceeds to undergo hydrolysis and polycondensation. By controlling the conditions at which the reactions take place, a variety of particle sizes and morphologies can be achieved. Depending on the specific application, different approaches can be taken to produce powders, fibers, thin films, coatings, porous membranes, etc. from the colloidal dispersion. Sol-gel processing hence offers a versatile nanoparticle synthesis route where high purity materials can be obtained without complicated and expensive equipment [69, p 102].

2.6.1 Hydrolysis and condensation of silicon alkoxides

The most commonly used precursors in sol-gel processing are silicon alkoxides ($Si(OR)_4$) such as tetramethyl orthosilicate (TMOS, $Si(OCH_3)_4$) and tetraethyl orthosilicate (TEOS, $Si(OC_2H_5)_4$) [71, 72]. When in contact with water, a hydrolysis reaction takes place where an alkoxide group (-OR) of the precursor is substituted with a hydroxyl group (-OH). This occurs through a nucleophilic attack on the silicon atom performed by the oxygen atom of the water molecule, leading to elimination of an alcohol as given in Equation 2.17 [73].

$$\mathrm{Si(OR)_4 + H_2O \rightarrow Si(OR)_3OH + ROH} \tag{2.17}$$

This shows the partial hydrolysis of a silicon alkoxide, where one of the four alkoxide groups is replaced with a hydroxyl group. With sufficient amounts of water present, further hydrolysis of the remaining alkoxide arms can result in complete hydrolysis. As polar water molecules and non-polar silicon alkoxide molecules are immiscible, a mutual solvent such as an alcohol is normally added. The solvent acts as a homogenizing agent, allowing the hydrolysis reaction to occur between the water and the alkoxide. In some cases, however, the alcohol produced as a by-product of the hydrolysis reaction can provide sufficient homogenization of the initially separated system, making it possible for the silicon alkoxide-water mixture to undergo hydrolysis without the addition of a solvent [71, p 108].

The sol-gel process is completed by a condensation reaction where siloxane bridges (Si-O-Si) are formed between the hydrolyzed precursor molecules upon release of a smaller molecule. This occurs either by oxolation or alkoxolation, where the leaving group is a water or an alcohol molecule, respectively. In the case of oxolation, the condensation reaction between two partially hydrolyzed silicon oxides can be written as

$$\mathrm{(OR)_3Si(OH) + (OH)Si(OR)_3 \rightarrow (OR)_3Si - O - Si(OR)_3 + H_2O} \tag{2.18}$$

where covalent siloxane bonds are formed upon release of a water leaving group. In the case of an alkoxolation mechanism, the hydroxyl group of a partially or fully hydrolyzed precursor molecule reacts with the alkoxide group of a second silicon oxide as follows

$$\mathrm{(OR)_3Si(OR) + (OH)Si(OR)_3 \rightarrow (OR)_3Si - O - Si(OR)_3 + ROH} \tag{2.19}$$

forming a covalent silicon-oxo bond upon elimination of an alcohol. The formation of silica gel through condensation can be regarded as taking place in two stages, according to Iler [52, p 175]. In the first stage, ring structures are formed due to the tendency of silicic acid ($Si(OH)_4$) to condensate in such a way that the number of siloxane bonds is maximized while the number of terminal hydroxyl groups is kept at a minimum. Monomers are then linked together and internal condensation results in larger spherical particles that can continue to grow following the Ostwald ripening mechanism. In the second stage of condensation, particles are linked together by Si-O-Si bonds into branched chains eventually forming a network extending throughout the liquid phase. This results in a rigid and highly porous gel network.

Acidic or basic catalysis and the effect on sol structure

To promote the hydrolysis and condensation reactions, either acidic or basic catalysts are employed, depending on the desired structure of the product. Generally, acids such as HCl are used in acidic catalysis while ammonia is commonly used in alkaline catalysis [74]. Depending on the pH, the particles formed in the sol synthesis will grow into larger particles or aggregate into clusters (or both). This is explained by the relative rates of hydrolysis and condensation in silicates as a function of pH, given in Figure 2.8 [72].

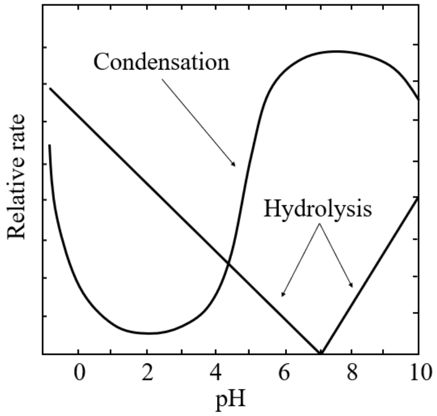

Figure 2.8: pH dependence of the relative reaction rates of hydrolysis and condensation in silicates. Adapted from Schaefer [72].

At low pH, hydrolysis dominates due to rapid protonation of the OR or OH groups bonded to the Si, making it more susceptible to a nucleophilic attack by water molecules. With increasing pH, the condensation rates increases due to higher solubility of silica at alkaline conditions [74]. The pH dependency of the hydrolysis and condensation rates affects the resulting sol structure. In acidic conditions, particles aggregate to create three-dimensional chained networks and form gels. Basic conditions, on the other hand, tend to promote internal condensation of monomers. This leads to particle growth with a decrease in the number of particles in the sol. [52, p 175].

2.6.2 Silica NP synthesis by the Stöber method

In 1986 a simple-to-follow and widely used method for synthesis of monodisperse, spherical silica nanoparticles, known as the Stöber (or Stöber-Fink-Bohn) method, was developed [75]. The reported synthesis route consisted of mixing an alcohol solvent, de-ionized water and an ammonia catalyst before adding the silicon alkoxide precursor under continuous stirring. By a sol-gel mechanism, amorphous silica spheres were obtained, having a narrow size distribution and a mean particle size ranging from 50-2000 nm. When TEOS is applied as precursor the overall hydrolysis and condensation reactions, respectively, can be written as follows [71, p 273].

$$\mathrm{Si(OC_2H_5)_4} + \mathrm{4H_2O} \rightarrow \mathrm{Si(OH)_4} + \mathrm{4C_2H_5OH} \tag{2.20}$$

$$\mathrm{Si(OH)_4} \rightarrow \mathrm{SiO_2} + \mathrm{2H_2O} \tag{2.21}$$

Here, the condensation is shown for a fully hydrolyzed silicon precursor and occurs through oxolation, evident by the water molecule by-product. The total reaction can be written as follows

$$\mathrm{Si(OC_2H_5)_4}(l) + \mathrm{2H_2O}(l) \rightarrow \mathrm{SiO_2}(s) + \mathrm{4C_2H_5OH}(l). \tag{2.22}$$

Upon simultaneous hydrolysis and polycondensation, the result is a spherical silica particle. Some terminal hydroxyl (-OH) groups will be present in the final structure but can be removed by calcination [76]. A simplified schematic of the reaction mechanism in the Stöber process is given in Figure 2.9. As previously discussed, condensation under basic conditions yields a three-dimensional structure instead of longer polymer chains. Hence, the addition of ammonia is a crucial step in the formation of spherical particles [69, p 108].

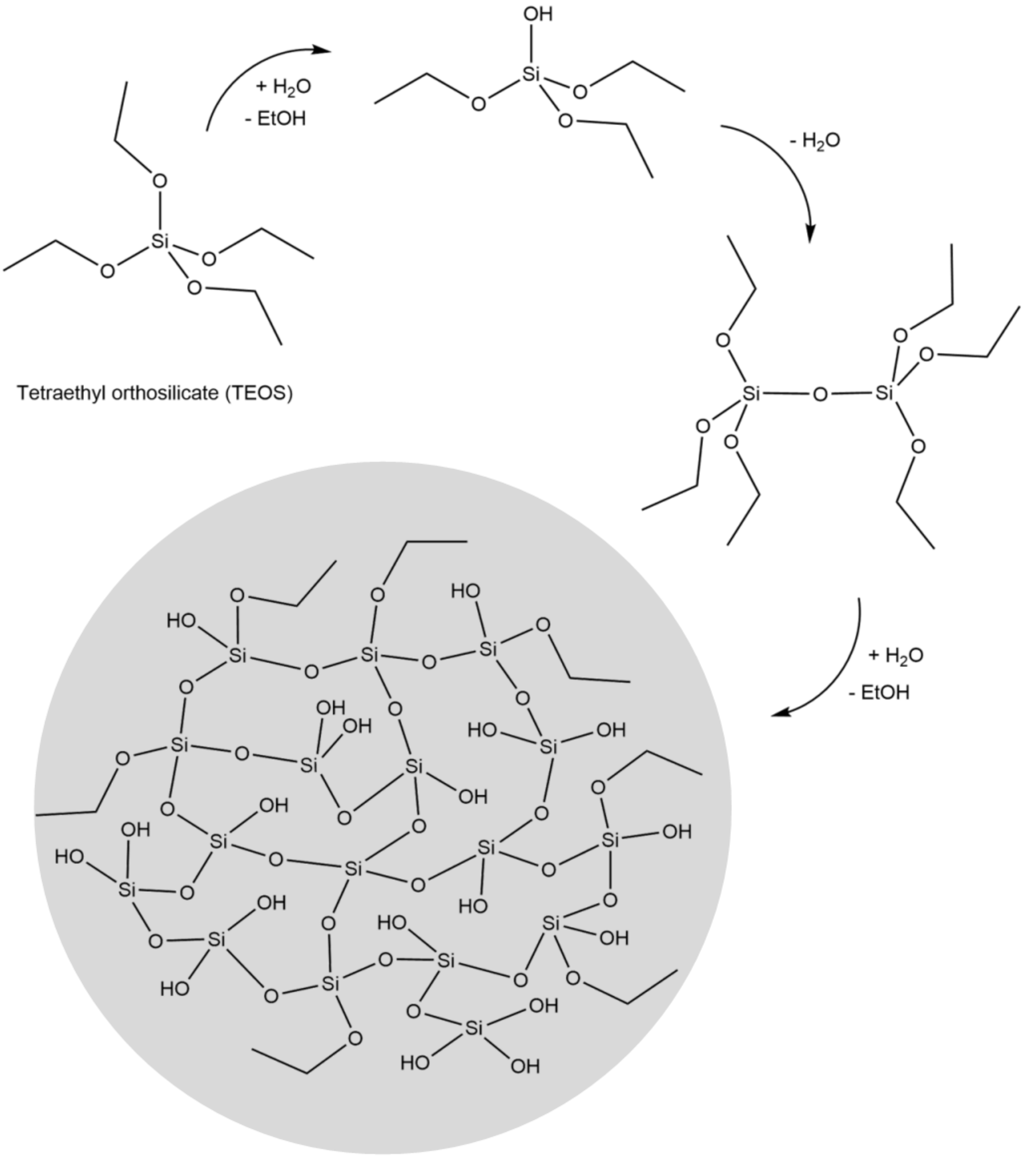

Figure 2.9: Overview of the Stöber process with TEOS.

2.6.3 Synthesis parameters and their effect

Since the Stöber method for synthesizing monodisperse silica NP spheres was demonstrated, efforts have been put towards better understanding of how to control the outcome. Research looking to describe the reaction mechanism and what affects it has contributed to a better tunability of the synthesis route, enabling the Stöber method to be applicable for various applications with different NP requirements.

Effect of reactant concentrations

The size of the colloidal particles obtained by the Stöber method is highly dependent on the reactant concentrations. With a TEOS concentration of 0.28 M, Stöber *et* al. [75] obtained different particle sizes when varying the concentration of water and ammonia. In Figure 2.10 the correlation between particle size and reactant concentrations is schematically presented.

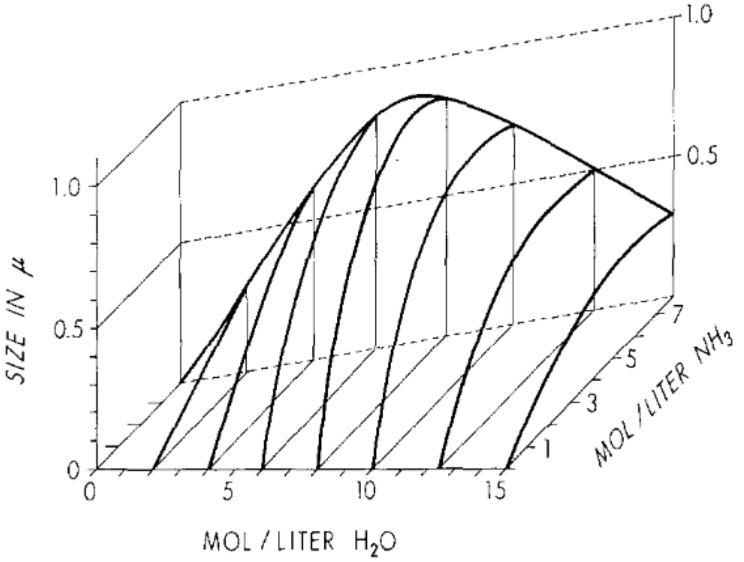

Figure 2.10: Final particle sizes as obtained by reacting 0.28 M tetraethyl orthosilicate (TEOS) with various concentrations of water and ammonia in ethanol. Reprinted from Stöber *et* al. [75] with permission from Elsevier.

Higher concentrations of the ammonia catalyst increases the reaction rate, promoting the formation of larger particles [77]. This trend of increasing particle size with increasing ammonia concentration is easily observed in the results obtained by Stöber *et* al. [75]. More recent studies also report results confirming this correlation [78, 79]. Figure 2.10 also shows that water content significantly affects the particle size. Matsoukas and Galari [77] reported that larger particles are favored at low water concentrations, while excessive water promotes smaller particles. However, very low water concentrations are expected to inhibit the hydrolysis step and potentially limit particle growth.

Effect of temperature

The reaction temperature affects the kinetics of the hydrolysis and condensation processes and thus influences the final sol structure. High temperatures can cause rapid hydrolysis which can lead to a large number of small nuclei being formed [69, 108].

Effect of solvent

Using smaller alcohols as solvents tend to favor smaller particles and narrower distribution [71, p 274]. Stöber *et* al. [75] reported faster reaction rates and more uniform particle sizes when using methanol as solvent compared to n-butanol. Compared to aprotic solvents, protic solvents such as methanol, ethanol and butanol tend to form hydrogen bonds with hydroxyl ions under basic conditions, reducing the catalytic activity [74].

2.7 Metal NPs through homogeneous nucleation

Colloidal dispersions of metallic nanoparticles are generally synthesized by a homogeneous nucleation process involving the reduction of metal precursors in dilute solutions. Through chemical reactions highly soluble chemicals are converted into less soluble substances, establishing a supersaturation. This leads to spontaneous nucleation and precipitation of metallic particles [69, p 64].

Various wet chemical synthesis routes exist for the formation of metallic NPs, applying different precursors, reducing agents, other chemicals and the reaction conditions. The metal precursor can be inorganic salts and metal complexes as well as elemental metals. Commonly used reducing agents include hydrogen (H_2, sodium citrate ($Na_3C_6H_5O_7$), citric acid ($C_6H_8O_7$), hydrogen peroxide (H_2O_2) and sodium borohydride ($NaBH_4$). Often, a polymer such as polyvinyl alcohol (PVA) or poly(vinylpyrrolidone) (PVP) is added to provide steric stabilization of the particles and promote a narrow size distribution. To achieve monosized particles, a low concentration of the metal precursor is also preferred as it limits the diffusion of growth species in solution to the initially formed nuclei [69, p 75].

2.7.1 Silver NP synthesis by the Lee-Meisel method

Colloidal silver particles are commonly synthesized by wet chemical methods. Typically, an inorganic silver salt precursor such as silver nitrate ($AgNO_3$) or silver tetraoxylchlorate ($AgClO_4$) is dissolved in water or an alcohol solvent and reduced by a reducing agent [69, p 76]. One such widely used procedure is the thermal reduction of silver nitrate by trisodium citrate (TSC), commonly referred to as the Lee-Meisel method after Lee and Meisel [63] demonstrated the preparation of a yellow silver sol with an absorbance maximum at 420 nm. The reduction of silver nitrate by TSC can be expressed as follows [80]

$$\begin{aligned} 4\mathrm{AgNO_3(aq)} + \mathrm{Na_3C_6H_5O_7(aq)} + 2\mathrm{H_2O} \rightarrow & 4\mathrm{Ag(s)} + \mathrm{H_3C_6H_5O_7(aq)} + 3\mathrm{NaNO_3(aq)} \\ & + \mathrm{HNO_3(aq)} + \mathrm{O_2(g)} \end{aligned} \tag{2.23}$$

TSC is a mild reducing agent promoting a slow reaction rate. Still, the process can proceed at comparable rates to that achieved with a strong reducing agent, such as sodium borohydride, at room temperature by heating the reaction mixture to at least 70°C [81]. However, the mild reaction conditions of this synthesis procedure using a weak reducing agent and no drastic change in temperature may result in the formation of a polydisperse suspension [82]. Citrate reduced silver colloids tend to be rather stable over time due to citrate molecules providing electrostatic stabilization by binding to the surface of the silver particles [70]. For added stability, poly(vinylpyrrolidone) (PVP) is often also added as a capping agent providing steric stabilization of the colloid [66].

Effect of reaction time

The time in which the reaction is left to proceed at an elevated temperature and vigorous stirring affects the nucleation and growth mechanism and hence the resulting silver particle size, size distribution and morphology. Following the Lee-Meisel procedure, Rinaldi and Latterini [82] demonstrated an increase in the mean Ag NP size with prolonged reaction time due to coalescence of the particles. When increasing the reaction time from 15 to 60 minutes, the mean diameter was found to increase from 15 nm and up to 50 nm. Results obtained by Munro *et* al. [83] however indicated that larger silver particles with a wider size distribution are initially formed, but as the reduction process continues large clusters dissociate into smaller, more stable particles with a more narrow size distribution. To achieve close to monodisperse, relatively spherical silver particles an optimal heating time of 90 minutes was suggested, resulting in particles with a diameter of approximately 20-40 nm.

Effect of reagent mixing procedure

In the classic Lee-Meisel method, the citrate reducing agent is carefully added to a solution containing silver ions. More recent findings by Rinaldi and Latterini [82] however suggest that a more narrow size distribution can be obtained when changing the mixing procedure. Dissolving TSC in water and letting it reach boiling temperature before then adding silver nitrate to the solution can lead to a more homogeneous reduction and nucleation process. This is explained by the high immediate availability of reducing agents upon addition of the silver ions, resulting in a more efficient formation of metallic silver.

Effect of reaction temperature

The reaction temperature can also affect the resulting silver nanoparticle size and shape. At elevated temperatures, there is a trade-off between higher nucleation and growth rates favoring small particles and acceleration of the Oswald ripening process wherein larger particles are formed at the expense of smaller ones [84].

2.8 Development of PBRs for NP implementation

When developing reactor designs that allow for the implementation of nanoparticles for small-scale research experiments, as well as for commercial applications, several considerations should be taken into account. Firstly, it is necessary to consider the potential adverse effects nanoparticles can have on living organisms and the environment. Due to a lack of knowledge and inadequate toxicology data, this is a great concern in nanotechnology. Nanoparticles behave differently than their bulk materials due to their huge area-to-mass ratio and are more biologically active the smaller they get [85]. Upon inhalation, enhanced deposition of small particles in the respiratory tract has been recorded, and from here the particles appear to easily translocate throughout the organism. Eventually, they can end up in vital organs such as the bone marrow, liver and heart. Uptake of NPs may also occur through dermal exposure and ingestion [85]. During the production, use and disposal of nanomaterials, some emissions to the environment are probable. When implementing such materials to microalgae production, taking health and safety precautions is crucial.

Secondly, any toxic effects that the nanoparticles may have on the microalgae species in question must also be considered. During the development of the research design presented in this thesis, this has been highly relevant, based on available documentation on the toxicity of silver and silica NPs. Silver nanoparticles are well known to have effective antimicrobial properties [86] which are utilized in a variety of applications including food packaging to prolong shelf life [87] and wastewater treatment [88]. When exposed to Ag NPs, a decrease in living cells has been reported for the marine microalgae *Chlorella vulgaris* [89]. Silica NPs have also been observed to inhibit the growth of certain algae species, and increasingly so for smaller particle sizes [90, 91]. Implementing such nanoparticles can hence have the opposite effect of what is intended by limiting the biomass production instead of accelerating it. To avoid these implications, a ”no contact” approach is taken in the present study where the NPs are kept outside of the reactor and do not interact with the algal cells. Such an approach has been demonstrated by Gianelli and Torzillo [27] who immersed a tubular PBR inside a silica NP suspension to enhance algal hydrogen production. In addition to eliminating any toxic effects, a no contact approach has multiple other benefits. As emphasized by Eroglu *et* al. [22], effective recycling of the NP suspension can be achieved, reducing material use and costs. Contamination of the produced biomass is also prevented. Avoiding contact between the NPs and the microalgae does, however, set some geometrical limitations to the PBR design and limits any light modulating effects of the studied NPs to occur at the interface between the two compartments. A full contact integration of scattering silica NPs into a microalgae culture could have the potential of providing continuous redistribution of the incident light throughout the algae medium. Still, the trade-off between optimal light transport and the toxicity and practical concerns remain an important factor. For the implementation of Ag NPs this issue is not as relevant. Being mainly used for their backscattering properties, placing them outside the algae suspension at the opposite side of the light source is likely to be a good approach also in terms of optimal light enhancement.

When developing designs for PBRs that utilizes engineered NPs, there is also a question of which medium should be used to contain the particles. From available research on this topic, the most common approach seems to be to keep the particles dispersed in a liquid phase [21, 22, 27]. This allows for efficient backscattering and shape flexible implementation to PBRs. In this case, however, settling of the particles should be limited which is especially challenging for larger particles. For silica NPs, particles with sizes above 100 nm will tend to settle, according to Iler [52, p 22]. Mixing of the NP suspension may therefore be necessary to achieve the desired light enhancing effect, which could potentially add to the costs of NP implementation to larger-scale production systems. Another possibility is to keep the particles embedded in a polymeric film, as demonstrated by Estime *et* al. [24] for silver particles.

In the present study, small-scale vertical column batch reactors are developed, consisting of a compartment housing the microalgae surrounded by an enclosed space for the nanoparticles. A schematic illustrating the design used in this study is provided in Figure 2.11.

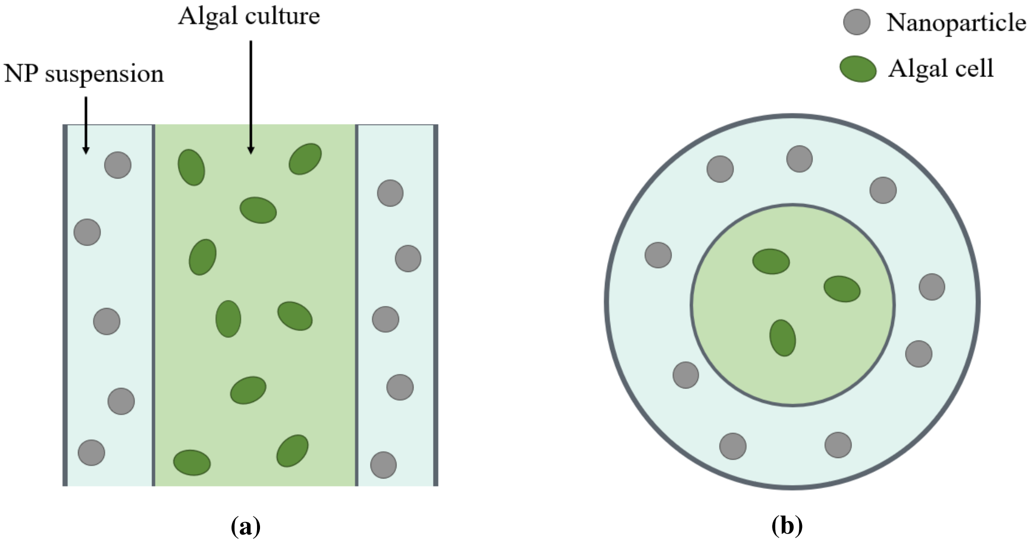

(a) (b)

Figure 2.11: Schematic of the PBR design used to implement NPs in this study, showing (a) as a cross-section and (b) from a birds eye view.

The same cultivation vessels are used in the study of the light enhancing effects of both silica and silver NPs to ensure similar growth conditions as well as for convenience. The synthesized NPs are kept in suspension and if necessary, manual mixing is provided for larger particles. This is predicted to be an appropriate approach for the use of silica scattering centers, but may be less suitable for the implementation of silver NPs. The possibility of coating half of the cultivation vessel with the plasmonic NPs so that they would only surround the backside of the algae culture was considered, however, this was not done in this thesis.

Lastly, to study the effect of light modulation by nanomaterials on biomass production it is important to be aware of the many factors that can affect the results. The growth and photosynthetic activity of a microalgae species are determined by numerous external factors such as the temperature, illumination conditions, CO_2 supply and availability of nitrogen, phosphorous and other nutrients [92, 93]. Keeping as many external factors constant is hence essential when developing suitable PBRs for testing. The algae used as model organisms should not be nutrition deprived or stressed in other ways, and multiple tests should be performed to ensure good reproducibility and to account for the sensitivity of the microalgae to small variations in the growth environment. An additional requirement is easy access to the algae culture to allow for sampling and monitoring of algal growth throughout the experiment, making sure that it can be done in the least invasive way possible.

3. Experimental

3.1 Silica nanoparticle synthesis

Using tetraethyl orthosilicate (TEOS) as precursor, different sols containing silica nanoparticles were synthesized by the Stöber method. The choice of chemicals for the synthesis was inspired by the procedure described by Stöber *et* al. [75]. The quantity of solution was kept around 50 mL for each parallel. The chemicals involved in the silica NP synthesis as well as their material properties are presented in Table 3.1 and Table 3.2, respectively.

Table 3.1: Chemicals used in the synthesis of silica nanoparticles by the Stöber method. The chemical formula, provider and chemical abstract service (CAS) number of each component is listed.

Chemical	**Formula**	**Provider**	**CAS**
Ammonium hydroxide, 28-30% (w/v)	NH_4OH	Sigma-Aldrich	1336-21-6
Ethanol, 96% (v/v)	C_2H_5OH	VWR Chemicals	64-17-5
Tetraethyl orthosilicate, 98% (v/v)	$Si(OC_2H_5)_4$	Sigma-Aldrich	78-10-4

Table 3.2: Material properties for the chemicals involved in the sol-gel synthesis of silica NPs. The molar mass, M_m [g/mol], density, ρ [g/cm^3], refractive index, n, and the boiling point, T_b [°C], is given.

Chemical	M_m **[g/mol]**	ρ **[g/cm^3]**	n **[-]**	T_b **[°C]**
Ammonium hydroxide, 28-30% (w/v) [94]	35.05	0.9	-	-
Ethanol, 96% (v/v) [95]	46.07	0.7895	1.359	78.3
Tetraethyl orthosilicate, 98% (v/v) [96]	208.33	0.933	1.382	168
Silica	60.1 [97]	1.8 [52]	1.472 [98]	2230 [97]

The size of the formed silica particles was varied by changing the amount of ammonium hydroxide catalyst added during synthesis. An overview of the respective amounts of solvent, water, catalyst and precursor added during each synthesis parallel is provided in Table 3.3. For convenience, the different sols will from now on be referred to in terms of their ”sol ID” introduced in Table 3.3. The sol ID includes the mean diameter (in nm) of the particles in the sol, discussed more thouroughly in later sections. That is, the mean particle diameter of the particles in the SNP95, SNP192 and SNP256 sols are 95 nm, 192 nm and 256 nm, respectively. The ”S” is chosen as a notation to indicate silica particles. The SNP95 sol was synthesized by the author during the project work preceding this thesis [48], using the same Stöber method described in this section. However, the characterization methods presented in later sections were performed on the particles during the work on this thesis.

Table 3.3: Respective volumes, V [mL], of ammonium hydroxide, ethanol, tetraethyl orthosilicate (TEOS) and deionized (DI) water used in silica NP synthesis.

Sol ID	V **[mL]**			
	NH_4OH	EtOH	TEOS	DI water
SNP95 [48]	1.0	45.0	1.5	6.0
SNP192	2.5	45.0	1.5	5.0
SNP256	5.0	45.0	1.5	5.0

Ethanol, de-ionized (DI) water and ammonium hydroxide were added to a 250 mL three-necked round bottom flask. Immersed in a water bath, heating to 35°C and magnetic stirring of 350 RPM was supplied by an RCT Basic dry block heater from IKA (Figure 3.1). The flask was connected to a Liebig condenser supplied with water cooling, providing a reflux system. After 10 minutes of heating and mixing the TEOS precursor was added dropwise to the solution using a micropipette. After 50 minutes of constant stirring at an elevated temperature, the heat source was removed and the sol was left to cool to room temperature. The sol was stored in a closed glass container at 6°C.

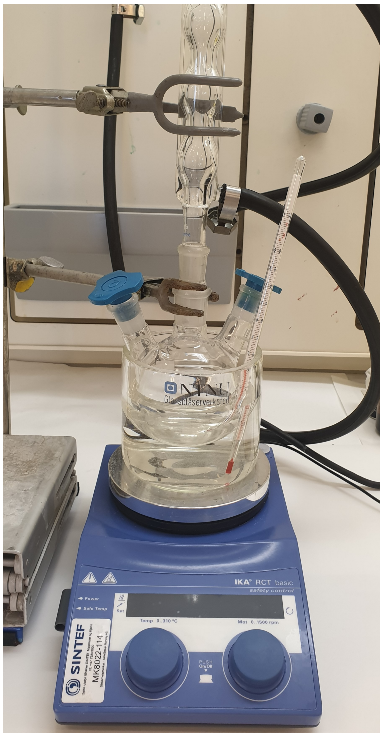

Figure 3.1: Experimental setup used in the silica nanoparticle synthesis. A three-necked round bottom flask immersed in a water bath which is placed on top of a hotplate with magnetic stirring. A reflux system is provided by a Liebig condenser supplied with water cooling through rubber tubes.

3.2 Preparation of silver colloids

Colloidal silver was synthesized by thermal reduction of silver nitrate with trisodium citrate. The experimental procedure and relative concentrations used was inspired by the citrate method described by Lee and Meisel [63]. An overview of the chemicals used to synthesize silver NPs and their material properties is given in Table 3.4 and Table 3.5, respectively. In Table 3.5 material properties for metallic silver are also included.

Table 3.4: Chemicals used in silver nanoparticle synthesis. The chemical formula, provider and chemical abstract service (CAS) number of each substance is listed.

Chemical	**Formula**	**Provider**	**CAS**
Silver nitrate	$AgNO_3$	Sigma-Aldrich	7761-88-8
Trisodium citratedihydrate	$C_6H_5Na_3O_7 \cdot 2H_2O$	Sigma-Aldrich	6132-04-3

Table 3.5: Material properties for the chemicals involved in the synthesis of silver colloids. The molar mass, M_m [g/mol], density, ρ [g/mol] and the boiling point, T_b [°C], is listed.(d = decomposes)

Chemical	M_b **[g/mol]**	ρ **[g/cm^3]**	T_m **[°C]**
Citric acid [99]	192.12	-	d175
Nitric acid [97]	63.0	-	83
Silver [97]	107.9	10.5	2212
Silver nitrate [97]	169.9	4.4	d440
Sodium nitrate [97]	85.0	2.3	d380
Trisodium citratedihydride [100]	294.10	-	$>$ 300

Silver nitrate (9.14 mg) was dissolved in DI-water (50 mL) and added to a 100 mL three-necked round bottom flask connected to a reflux system made up of a Liebig condenser with water cooling. The solution was brought to boiling by an RCT Basic dry block heater from IKA equipped with a H135.20 Flask carrier (Figure 3.2). Magnetic stirring at 600 RPM was supplied. A citrate solution was prepared by dissolving sodium citrate (11.30 mg) in DI-water (1 mL) and added dropwise to the solution by a micropipette. The reaction was left to proceed under heating and vigorous stirring for 60 minutes. The colloid was stored at 6°C in a dark environment.

Figure 3.2: Experimental setup used in the preparation of silver colloids. A three-necked round bottom flask is placed on an RCT Basic dry block heater. Reflux is provided by a Liebig condenser with water cooling.

3.2.1 Study and optimization of the synthesis procedure

Different adaptations of the Lee-Meisel citrate method were applied and the effect of reaction conditions on sol characteristics, particle size and morphology as well as on their optical properties was studied. This was done to gain a better understanding of the synthesis mechanism and to optimize the procedure to achieve silver particles of desired shapes and sizes for the given application. An overview of the amount of reactants and the reaction conditions used in each experiment studying the Lee-Meisel method for AgNP synthesis is given in Table 3.6

Table 3.6: Overview of the mass of silver nitrate and TSC as well as the DI-water volumes in their respective solutions for each experiment. The reaction conditions are given in terms of temperature, RPM and reaction time. ($\star$: Withdrawl of samples started after 3 min.)

Exp.	NP ID	**$AgNO_3$ solution**		**TSC solution**		**Reaction conditions**		
		$m_{\mathrm{AgNO_3}}$ [g]	$V_{\mathrm{H_2O}}$ [mL]	m_{TSC} [g]	$V_{\mathrm{H_2O}}$ [mL]	T [°C]	RPM	t [min]
1	AgNP#1	0.00777	50	0.01296	10	93	650	60
2	AgNP#2	0.00830	50	0.05111	5	100	450	5
3	AgNP#3	0.00946	50	0.01122	1	100	600	90
4	AgNP#4	0.00935	50	0.01122	1	100	600	90*

Experiment 1 / AgNP#1

$AgNO_3$ (7.77 mg) was dissolved in a 50 mL of DI-water and added to 250 mL three-necked round bottom flask equipped with a reflux condenser. Heat was provided by an RCT Basic dry block heater from IKA through a water bath covered with aluminium foil. Magnetic stirring at a rate of 650 RPM was applied. A maximum temperature of 93°C was achieved, insufficient in bringing the reaction solution to boiling. A solution of 0.1296 $\%$ (w/v) sodium citrate (10 mL) was added dropwise and the reaction was left to proceed at elevated temperature and stirring for 1 h. The solution was then removed from the heat and left to cool to room temperature.

Experiment 2 / AgNP#2

Following the modified Lee-Meisel method reported by Rashid *et* al. [80], $AgNO_3$ (8.30 mg) was dissolved in a 50 mL of DI-water and added to a 100 mL three-necked round bottom flask. The solution was brought to boiling by an RCT Basic dry block heater from IKA equipped with an H135.20 Flask carrier whilst stirred at 450 RPM and kept at reflux. A 1.0222 $\%$ citrate solution (5 mL) was then added drop by drop. The solution was kept at boiling temperature and vigorous stirring until a change in color was evident, after 5 min. It was then removed from the heat source and left to cool to room temperature whilst the stirring proceeded.

Experiment 3 / AgNP#3

Prior to the synthesis, the reaction vessel was cleaned with 1M nitric acid (HNO_3) and rinsed with deionized water. Silver nitrate (9.46 mg) was dissolved in 50 mL DI-water and added to a 100 mL three-necked round bottom flask. The rate of stirring was set so that the solution vortex reached the base of the stirrer (600 RPM), inspired by Munro *et* al [83]. The solution was brought to boiling using the same heater equipped with a flask carrier from IKA and reflux system as before. A solution of 1.122 % trisodium citrate (1mL) was added dropwise and the solution was kept boiling under continuous stirring. The solution was removed from the heat after 90 min, as proposed by Munro *et* al. [83] in order to optimize the classic Lee-Meisel procedure [63] in terms of reproducibility and intensity.

Experiment 4 / AgNP#4 - the effect of reaction time on NP size, morphology and stability

The effect of different reaction, or boiling, times on the size and morphology of the formed silver NPs as well as colloid stability were studied. This was motivated by the rapid color change observed after the addition of TSC reducing agent to the silver nitrate solution in the previous experiments. The method used was inspired by the work performed by Munro *et* al. [83] in the study of the colloid formation reaction when following their optimized procedure for use in surface-enhanced resonance Raman scattering (SERRS). The classic Lee-Meisel citrate method [63] was adapted to a 50 mL quantity and applied. A 100 mL round-bottom flask cleaned with nitric acid was used as a reaction vessel. The silver nitrate (9.35 mg) dissolved in 50 mL DI-water was brought to boiling by heater and flask carrier and kept under reflux. A stirring rate of 600 RPM was applied. Then, a 1.122 % citrate solution (1 mL) was added dropwise and the boiling and stirring were continued for 90 min. Samples were withdrawn from the solution at different times after the addition of TSC and rapidly cooled in an ice bath. The first sample was taken when a slight color change from transparent to light yellow was observed, at a boiling time of approximately 3 min. After this, samples were taken every minute until reaching 10 min, and then at 15, 20, 30, 45, 60 and 90 minutes of boiling. The samples were left to reach room temperature and diluted 1:5 with DI-water before being analyzed in a UV-VIS spectrophotometer. Samples taken at 3, 5, 7, 10 and 90 minutes were chosen for FESEM imaging. The effect of reaction/boiling time on the stability of the sols was also investigated by measuring the absorbance spectra off all withdrawn samples one and two weeks after synthesis.

3.3 Characterization of nanoparticles

3.3.1 Particle morphology, size, and size distribution

The morphology of the particles as well as the particle size and size distribution were characterized by field emission scanning electron microscopy (FESEM). This was done with a ZEISS Ultra 55 Limited Edition FESEM using a secondary electron (SE) detector. Images were obtained with a 30 µm aperture, an acceleration voltage of 2 keV and a working distance of approximately 10 mm. To prepare the silica samples for FESEM imaging, a small amount was extracted from the synthesized sol and diluted at a ratio of 1:10 with ethanol. For the synthesized silver NPs, SEM samples were prepared by diluting 1:10 with DI water. The diluted samples were then placed on a 12.5 mm diameter aluminium SEM Specimen Stub from Agar Scientific and dried overnight in a ventilated area to allow solvent evaporation.

Based on the obtained FESEM images, particle size distribution analyses of the silica NPs were performed using the scientific processing program ImageJ (version 1.52). The cross-sectional area of the particles was measured and used to determine the particle diameter, assuming perfectly spherical particles. In Figure 3.3 the outlines of the particles used in the PSD analysis of the SNP256 sol are shown on top of the FESEM image used, as an example. Such overlays are provided for the other samples in Appendix A.

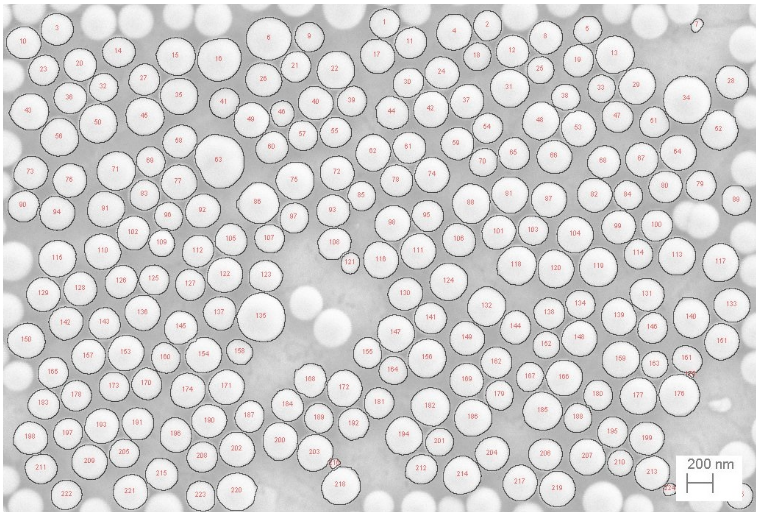

Figure 3.3: Overlay of the FESEM image chosen as a basis for the PSD analysis of SNP256 and the particle outlines identified in Image J.

Overlapping particles were not included in the analysis, and a minimum of 100 particles was used as a basis for the calculations. For the silver particles, a circularity of at least 0.7 (where 1 corresponds to a perfect circle and approaching 0 indicates an increasingly elongated polygon) was chosen as a requirement for the particles to be included in the analysis.

3.3.2 Particle concentration

The particle concentrations were determined gravimetrically by measuring the change in mass upon solvent evaporation. A small quantity of the studied sol (1 mL) was added to a crucible and heated for 1 hour at 150°C in a VENTI-Line Ventilated Drying oven from VWR. This was done for three replicate samples. The sample mass was registered before and after the drying process, and based on this the mass concentration of the NPs in solution was obtained. The number of particles per cubic micron of sol was then calculated using the density of the NP material and the mean particle diameters determined in the particle size distribution analysis. Based on the formation reaction of silica (eq. 2.22) and the material properties of the reaction products (Table 3.2), heat-treating the silica sol samples at 150°C should leave only the silica particles remaining in the crucible (when assuming a complete reaction). For the silver colloids, other formed reaction products will remain in the crucible after the heat treatment, based on equation 2.23 and the boiling/decomposition temperatures listed in Table 3.5. Thus for silver samples, the mass ratio of the metallic silver to the other reaction products not removed during heating was calculated and used to estimate the obtained mass of silver NPs from the measured mass left in the crucible. The calculation is provided in Appendix B. When using this method for concentration determination, it was assumed that there was no contribution from potential contaminants to the measured masses. The calculated particle concentrations given in number of NPs per cubic micron are also based on the assumption that the dispersions only contain spherical particles.

3.3.3 Particle composition and structure

The composition and structure of the particles were studied by X-ray diffraction (XRD) for one of the silica sols (SNP256) and the final silver colloid (AgNP57). Samples for XRD measurements were prepared by placing drops from the NP solutions onto a zero diffraction Si plate and allowing solvent evaporation. To achieve decent coverage on the Si plate, multiple layers were deposited. When dry, the sample was covered with a kapton foil. XRD measurements were carried out by Dr. Kristin Høydalsvik Wells in a Bruker D8 FOCUS Powder Diffraction System with Cu$\kappa\alpha$ radiation. A 2Θ range from 30° to 90° was used, with a step length of 0.014°. The total scanning time was 2 h, giving a time per step of 1.6 s. The measurements were done with a 1 mm divergence slit and an X-ray effect of 40 KV and 40 mA. The XRD raw data was analyzed using the DIFFRAC.EVA version 5.0.1.5. software from Bruker. For phase identification, the obtained XRD patterns were matched with patterns found in the Crystallography Open Database (COD). Crystallite size estimates based on the Debye-Sherrer method were also performed in EVA.

3.4 Absorbance measurements

All silver samples were diluted with deionized water at a ratio of 1:5 and their optical properties were evaluated in an Evolution 220 UV-Visible Spectrophotometer provided by Thermo Scientific. For data handling, the complementary computer software, INSIGHT 2.2.273 was used. Absorbance measurements were carried out with a wavelength range from 350-1100 nm and with an integration time of 0.2 s. Eppendorf UVette disposable cuvettes with a spectral range of 220-1600 nm were used with an optical path length of 1 cm through the sample. To eliminate the effect of any instrumental noise, the absorbance of a blank sample was measured prior to the analyses. The blank sample consisted of either pure DI-water when studying the scattering properties of silica samples, and ethanol when studying the silver samples.

3.5 Calculation of angular scattering distribution

The scattering properties of the synthesized NPs were further studied by calculating the scattered light intensity as a function of scattering angle. The angular scattering distribution was calculated using the code available at `http://omlc.org/calc/mie_calc.html` (accessed 26.06.20), created by Scott Prahl and recently recognized in a paper by Lehmuskero *et* al. [35]. The calculations are based on Mie theory and consider light scattered by a dispersion of monosized, spherical particles. Polar scattering plots were generated for the SNP95, SNP192, SNP256 and AgNP57 colloids based on the mean particle diameters and NP concentrations [NPs/μm^3], determined as described in previous sections. The wavelength of the incident light was set to 400 nm (violet light), and other input parameters were the real and imaginary refractive index of the NPs as well as the refractive index of the medium. For the silica sols, the refractive indices of silica and ethanol were used as retrieved from literature (Table 3.2). As colloidal silica spheres are known to be non-absorbing, their imaginary refractive index was set to zero [101]. For the silver NPs the complex refractive index of 0.173 - 1.95i [102] was applied. A refractive index of 1.33 was used for the aqueous medium [103].

3.6 Study of colloid stability

The stability of the formed colloids over time was investigated by UV-VIS spectroscopy. With the most optimal conditions for microalgae cultivation being between 20 and 25°C [104], the stability of NP suspensions at such temperatures was studied. To get an idea of whether or not the NPs experienced any significant changes during the growth experiments, samples were placed in the dark at 6°C and room temperature and their absorbance spectra were recorded at the start date of the growth experiment and after 1 week. The samples were not sonicated during this period in order to provide more realistic conditions and to be able to observe potential agglomeration. For the previously synthesized SNP95 silica sol, the stability over a longer period was investigated both by UV-VIS spectroscopy and FESEM imaging after being stored at 6°C for 5 months. For the AgNP56 colloid, the effect of reaction time on colloid stability was evaluated by absorbance measurements after 1 and 2 weeks when stored at RT.

3.7 Microalgae growth experiments

3.7.1 The photobioreactor

The photobioreactor used in the growth experiments was a Multi-Cultivator MC 1000-OD from PSI (Photon Systems Instruments) composed of 8 cultivation vessels immersed in a water bath (Figure 3.4). The Multi-Cultivator was equipped with a Cooling Unit AC-625, also from PSI, consisting of an AC-625 water pump and Hailea HC-130A water chiller to allow for regulation of the water bath temperature. An array of cool white light emitting diodes (LEDs) located behind the cultivation vessels served as the illumination source, with the ability to adjust the irradiance independently for each vessel. Plastic dividers between each cultivation vessel limited light penetration between neighboring cultivation slots. To eliminate the effect of the light environment surrounding the MC, a cardboard piece was used to shield the front of the reactor during experiments. Carbon dioxide as well as mixing of the cultures was provided by bubbling air into each vessel at a rate sufficient to avoid algae sedimentation. The air was hydrated by passing it through a humidifier bottle containing DI-water prior to entering the cultures. It was then carried through the main gas dispenser tube and the air flow rate was adjusted manually for each vessel using individual valves.

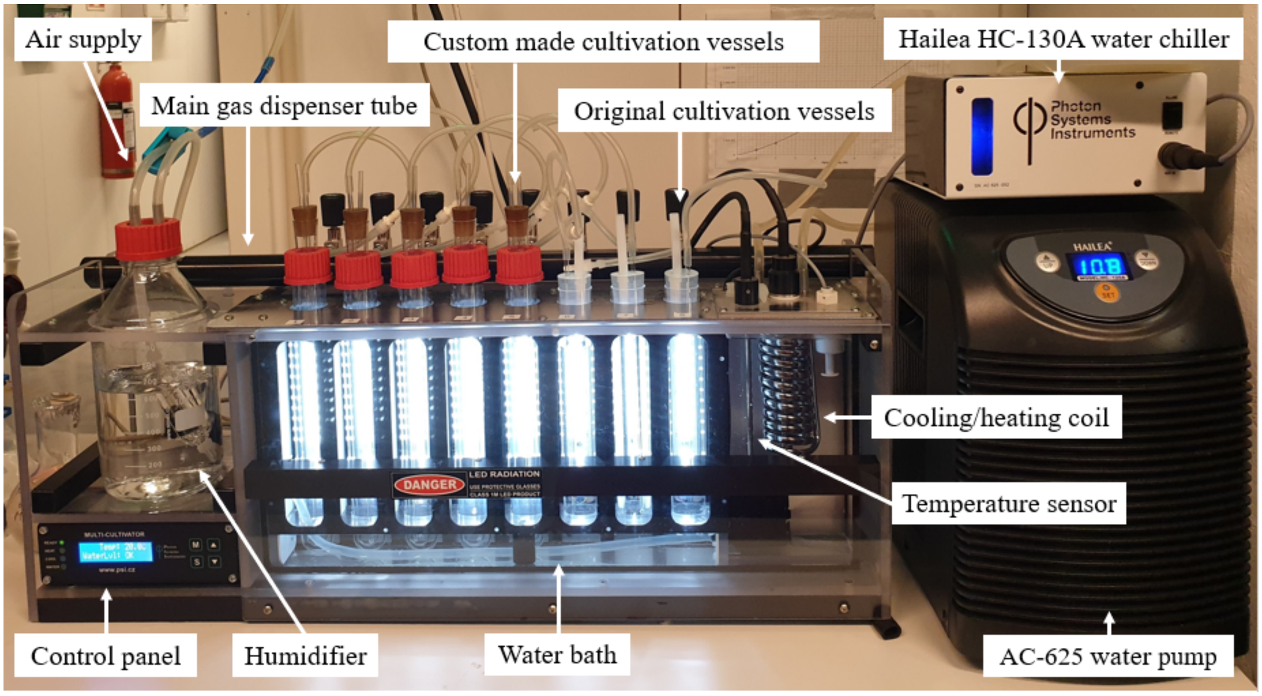

Figure 3.4: Experimental setup used in microalgae growth experiments. Five cultivation vessels designed for NP implementation are placed in a Multi-Cultivator, immersed in a thermostated water bath and illuminated with LEDs from the back. Hydrated air is supplied to each vessel through individual valves on the main gas dispenser tube.

The Multi Cultivator setup was modified by replacing the original cultivation vessels with custom made vessels allowing for simple implementation of the synthesized nanoparticles. Five vessels consisting of an inner and outer borosilicate glass test tube were designed and then supplied by the NTNU glassblowing workshop. The inner tube was 28 cm long with a diameter of 1.6 cm and the outer tube was 25 cm long and had a diameter of 2.6 cm. The tubes were assembled by attaching an open-top screw cap with a sealing ring onto the larger tube and placing the smaller tube inside. This gave an inner and outer volume of approximately 40 mL and 35 mL, respectively. The inner test tube was enclosed with a rubber stopper with two holes, both holding small glass tubes with an outer diameter of 3 mm. The longest glass tube (31.5 cm) was connected to the gas supply through a rubber tube whilst the other one (6.5 cm) acted as a vent hole. A schematic of the designed and developed cultivation vessels is provided in Figure 3.5.

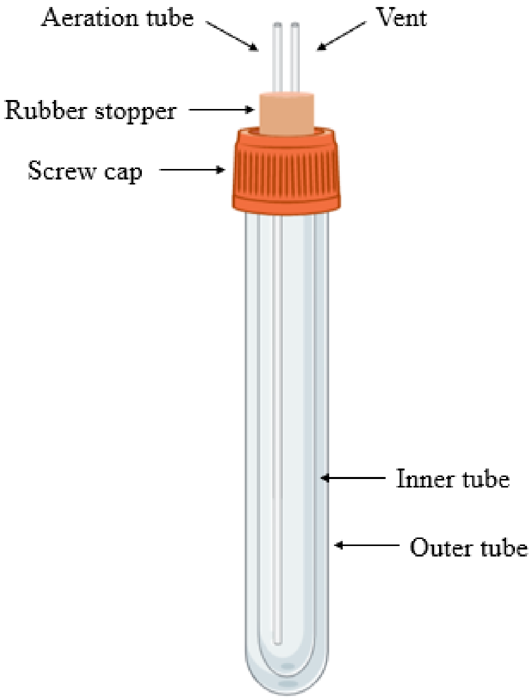

Figure 3.5: Schematic of the cultivation vessels developed for NP implementation, consisting of an inner and outer borosilicate glass tube attached by an open-top screw cap. Through a rubber stopper, aeration and ventilation are provided to the inner tube. Created with BioRender.

The design of the cultivation vessels allows a no-contact approach to be taken when implementing the synthesized nanoparticles. The inner tube provides aeration to the algae culture and the removable rubber stopper allows for easy sampling during the growth experiments. The space between the inner and outer tube acts as an enclosed compartment for nanoparticle storage. In this compartment, no mixing is provided.

3.7.2 Algal strain, growth medium and start cultures

As a model species, a *Rhodomonas baltica* NIVA-F/91 strain from The Norwegian Culture Collection of Algae (NORCCA) [105] was used. For each growth experiment, start algae were supplied from a stock culture kept by Dag Altin at Biotrix. The cells were grown in enriched seawater in a f/2 medium with doubled concentrations of nitrogen and phosphorous nutrients but with the original concentrations vitamins and trace metals [106, 107]. The N and P was added in the form of sodium nitrate ($NaNO_3$) and sodium dihydrogen phosphate dihydrate ($NaH_2PO_4 \cdot H_2O$). Sodium silicate was omitted from the prepared medium as it is only required for cultivation of diatoms and silicoflagellates. The start cultures had a slight red tint due to the Phycoerythrin pigment that the *R. baltica* strain contains (Figure 3.6a). Using an optical microscope, the many cells making up the algal culture can be seen (Figure 3.6b), with cell lengths in the 10 μm size region. The OM images were taken for a more dense culture, at the end of a growth experiment.

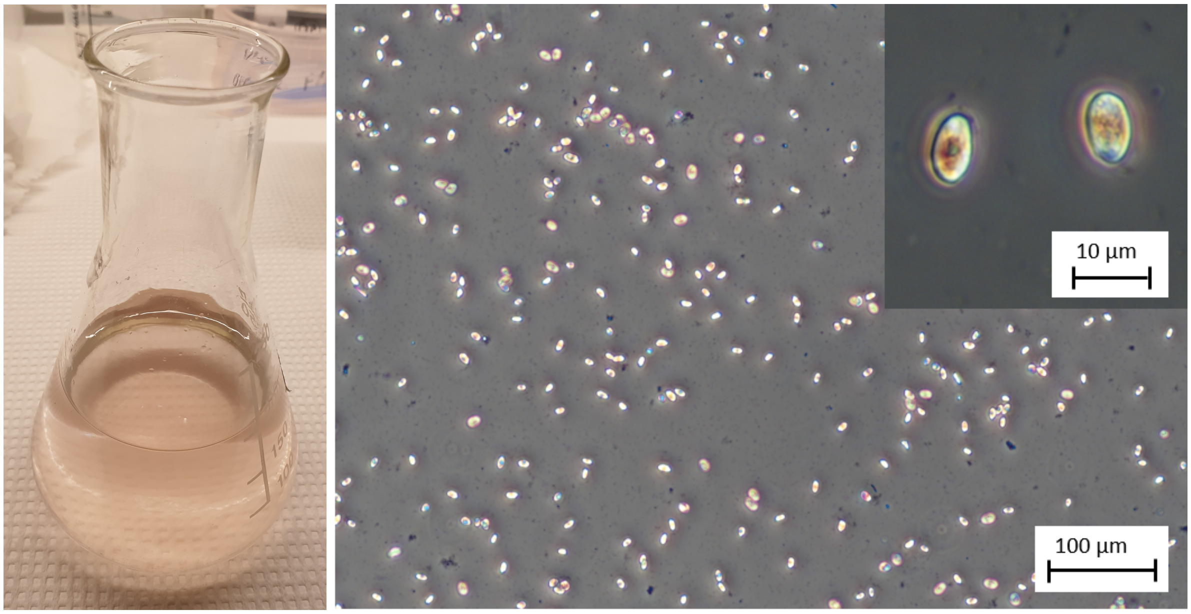

(a) **(b)**

Figure 3.6: Photo of (a) one of the *Rhodomonas baltica* start cultures used in growth experiments and (b) the algal cells, taken with an optical microscope.

The cell concentration in the start cultures was on average 14.5 ± 4.5 cells/μL. The initially recorded PE fluorescence for the cultures varied between 357 and 600, and the chl. *a* fluorescence between 7884 and 16337, all in relative units (r.u.). The starting turbidity varied from 2.546 to 5.020. To ensure that the algae were in good condition at the start of the cultivation, only cultures with relatively high quantum yields were used. The quantum yield is a ratio between 0 and 1, rarely exceeding 0.8. When the ratio is around 0.7-0.75 the cells are generally considered to be in good photosynthetic condition. For the four growth experiments in the present work, the initial QY ranged from 0.66 to 0.75.

3.7.3 Microalgae suspension analyses

To monitor algal productivity and growth, samples were withdrawn throughout the experiments and analyzed by various methods. Samples were added to Polystyrene Spectrophometry Cuvettes from Kartell, and different spectrophotometer measurements were performed. The phycoerythrin fluorescence and the turbidity were determined using an AquaFluor Handheld Fluorometer and Turbidimeter from Turner Designs. The instantaneous chlorophyll fluorescence, F_t, and the quantum yield of the samples were recorded with an AquaPen-C AP-C 100 from PSI. After these measurements, the sample volumes were returned to their respective cultivation vessels to limit the loss of algal cells during the experiments. A direct measure of the microalgae density was obtained through cell counting analyses. For this, 1 mL of algae culture was withdrawn and fixated by adding one drop of Lugol's Iodine solution and mixing thoroughly. The samples were then stored in a cool place up until the analyses were conducted. Cell counting was performed in Karl Hecht Assistant Burker Counting Chambers with a chamber depth of 0.1 mm using a Nikon ECLIPSE TS100 inverted microscope. A volume of 0.025 μL (4 B-squares) was used and 5-10 replicate countings were performed for each sample point.

3.7.4 Overview of the conducted growth experiments

An overview of the different growth experiments is given in Table 3.7. Each experiment is presented in terms of the NP ID of the particles studied in that case. For the vessels containing NPs in their outer tube, the mass concentration of that particular suspension is provided. In the control tubes, 96% ethanol or DI-water was added to the outer compartment to provide the same dielectric environment as in the rest of the vessels.

Exp. no.	**NP ID**	**Cultivation vessel no.**				
		1	**2**	**3**	**4**	**5**
1	SNP95	7217 mg/L	Control	-	-	-
2	SNP192	40 mg/L	40 mg/L	Control	160 mg/L	160 mg/L
3	AgNP57	4 mg/L	4 mg/L	Control	20 mg/L	20 mg/L
4	SNP256	40 mg/L	40 mg/L	40 mg/L	Control	Control

Table 3.7: Overview of the 4 growth experiments conducted, stating the ID of the NP suspension used and the content in the outer compartment of each cultivation vessel. For the tubes containing NPs the concentration is provided. The control tubes containing ethanol or DI-water are denoted as "Control". The vessels have been numbered according to their placement in the Multi-Cultivator, going from "1" to "5" from left to right in the photo of the reactor (Figure 3.4).

In all of the experiments the temperature of the water bath was set to 20 °C and a constant irradiance flux of 100 $\mu\text{mol.m}^{-2}.\text{s}^{-1}$ was used. More detailed descriptions of each growth experiment are provided in the following sections. In later discussions of the results, algal cultures surrounded by NPs will be referred to in terms of the mass concentrations of the specific NP suspension studied in that growth experiment. That is, when discussing the growth experiment applying two different concentrations of the SNP192 suspension, the culture surrounded by 40 mg/L of the silica particles are denoted "the 40SNP culture". Similarly, for the experiment using

AgNP57, the algae surrounded by 4 mg/L of the silver particles are referred to as ”the 4AgNP culture”.

3.7.5 Pilot study with the SNP95 sol

A pilot growth experiment was carried out to test the photobioreactor setup and the analytical procedures used to monitor algal growth. For this, undiluted SNP95 sol (7217 mg/L) was used to test the implementation of silica NPs to the reactor and study any potential effects on algal growth. The initial *R. baltica* culture was divided into two cultivation vessels and the SNP95 sol was added to the outer tube of one of them. In the control tube, 96% ethanol was added. Analytical measurements described in the previous section were carried out on the initial algae suspension and repeated for both cultures after 3, 5 and 7 days.

3.7.6 Growth experiment with 40 mg/L and 160 mg/L of SNP192

In this experiment, the effect of two different concentrations of the prepared SNP192 sol on algal growth was investigated. The chosen NP concentrations were inspired by the study by Giannelli and Torzillo [27] who used a light scattering suspension of silica NPs with a diameter of 540 nm. Among the studied concentrations of 10, 20, 40 and 60 mg/L, the best compromise between perpendicular scattering and light penetration was achieved with an NP concentration of 40 mg/L. Based on this, a solution of approximately 40 mg/L of the SNP192 sol was prepared by diluting with ethanol. The second NP suspension was chosen to have a mass concentration of 160 mg/L. 40 mL of the 40 mg/L suspension was added to the outer tube of two cultivation vessels, acting as replicas. Similarly, 40 mL of the 160 mg/L solution was added to two of the other vessels. The last of the five cultivation vessels served as a control tube, having 40 mL of pure 96% ethanol in its outer compartment. The start algae culture (35 mL) was added to the inner tubes of each cultivation vessel. The PE fluorescence, turbidity, chlorophyll fluorescence and quantum yield were measured initially, and after 1, 2, 5, 6, 7 and 8 days. Samples for cell counting were withdrawn at days 0, 2, 5 and 8.

3.7.7 Growth experiment with 4 mg/L and 20 mg/L of AgNP57

The second growth experiment was carried out using the AgNP57 colloid of two different concentrations. To determine which NP concentrations to study, the absorbance spectra of different dilutions of AgNP57 were compared to the spectra of the 40 mg/L and 160 mg/L SNP192 sols used in the previous experiment. When diluted to a concentration of approximately 4 mg/L, the maximum absorbance intensity of the AgNP57 particles was similar to that of the 160 mg/L SNP192 sol. Hence, for the NPs used in the growth experiments to have comparable optical properties, one of the AgNP57 concentrations studied was 4 mg/L. For the second concentration, initially, 40 mg/L of the silver particles was considered, however, due to its very dark and turbid appearance, 20 mg/L was instead used. Both concentrations were added to two cultivation vessels, and the last tube served as the control, containing DI-water. Analyses of the microalgae samples were carried out on days 0, 1, 2, 4 and 7, and the measurements were repeated three times for each culture. Cell counting samples were withdrawn at days 0, 2, 4 and 7.

3.7.8 Growth experiment with 40 mg/L of SNP256

The final growth experiment was conducted with larger silica nanoparticles, using the SNP256 sol to study the effect of increasing the size of the scattering centers. Only one NP concentration was applied and multiple replicates were used to obtain data with a better statistical basis than in the previous experiments. A concentration of 40 mg/L was chosen. Again, this was inspired by the work of Giannelli and Torzillo [27] although they utilized larger particles and a larger volume of the NP suspensions. Using 40 mg/L of the SNP256 sol would also allow for comparison with the 40 mg/L SNP192 solution used in the previous growth experiment with silica, thus making it possible to observe any potential effect of particle size on the biomass production. The silica suspension was added to the outer tube of three of the cultivation vessels and the other two served as control vessels having ethanol in their outer tubes. For this experiment, extended access to the experiment facilities was gained, hence analyses of the algae cultures were conducted every day for 1 week. The measurements were repeated three times for each of the cultures. Samples for cell counting were withdrawn at days 0, 2, 4 and 7.

3.7.9 Optical light microscopy

A *R. baltica* culture in good condition was chosen for investigation in a Nikon Eclipse 50i optical light microscope. Pictures of the live algae were captured with a Nikon camera using the NIS Elements software.

4. Results

4.1 Synthesized silica NP sols

Two sols containing spherical silica nanoparticles of different sizes were synthesized. In Table 4.1 the calculated mean particle diameter achieved for given concentrations of ammonium hydroxide is given for both sols. The silica NP concentrations are also provided both in terms of mass concentration, c_{m} [mg/L], and number of NPs per cubic micron, c [NPs/µm^3]. Results from the updated characterization of the silica sol synthesized during the project work preceding this thesis [48] (the SNP95 sol) are also presented.

Table 4.1: Mean particle diameter, d [nm], achieved for given ammonium hydroxide concentrations, c_{NH_4OH}. The mass concentration, c_{m} [mg/L], and NP concentration, c [NPs/µm^3], is also given for the synthesized sols referred to by their sol ID.

Sol ID	$c_{\mathrm{NH_4OH}}$ [mol/L]	d [nm]	c_{m} [mg/L]	c [NPs/µm^3]
SNP95	0.08	95 ± 11	7217 ± 553	8.93 ± 0.68
SNP192	0.21	192 ± 24	8153 ± 254	1.22 ± 0.04
SNP256	0.39	256 ± 40	7972 ± 174	0.50 ± 0.01

Larger particles were achieved when more ammonium hydroxide catalyst was added during synthesis. Almost a doubling of the NP size from 95 nm to 192 nm was achieved when increasing the catalyst concentration by a factor of 2.5. For all sols, similar NP mass concentrations were obtained, as expected since the same amount of TEOS precursor was added in all cases. Hence, the sols containing smaller particles had a larger number of NPs per cubic micron than those containing larger silica particles. All three sols had a similar white, milky appearance, but when compared a slight blue tint was observed for the SNP95 sol (Figure 4.1).

Figure 4.1: Image of the synthesized silica sols, with particle sizes of (from left to right) 95 ± 11 nm, 192 ± 24 nm and 256 ± 40 nm.

Inspection of the particles by electron microscopy revealed spherical shapes and relatively uniform sizes with little agglomeration. For the SNP95 sol, some aggregated particles could however be seen. This may be a result of the prolonged storage of this sol prior to the FESEM imaging, as discussed later in section 4.6.1. FESEM images of the particles as well as histograms obtained in the size distribution analysis are provided in Figure 4.2 for each sol. Normal distribution curves generated from the mean particle diameters and standard deviations are also plotted. The size distribution histograms show a wider spread in particle size for the sols with larger particles (4.2). For the sol with the smallest particles, the SNP95 sol, the standard deviation was 11 nm whereas for the SNP256 sol it was almost 4 times higher with an SD of 40 nm. Thus, more monosized silica NPs were obtained for the smaller particle sols.

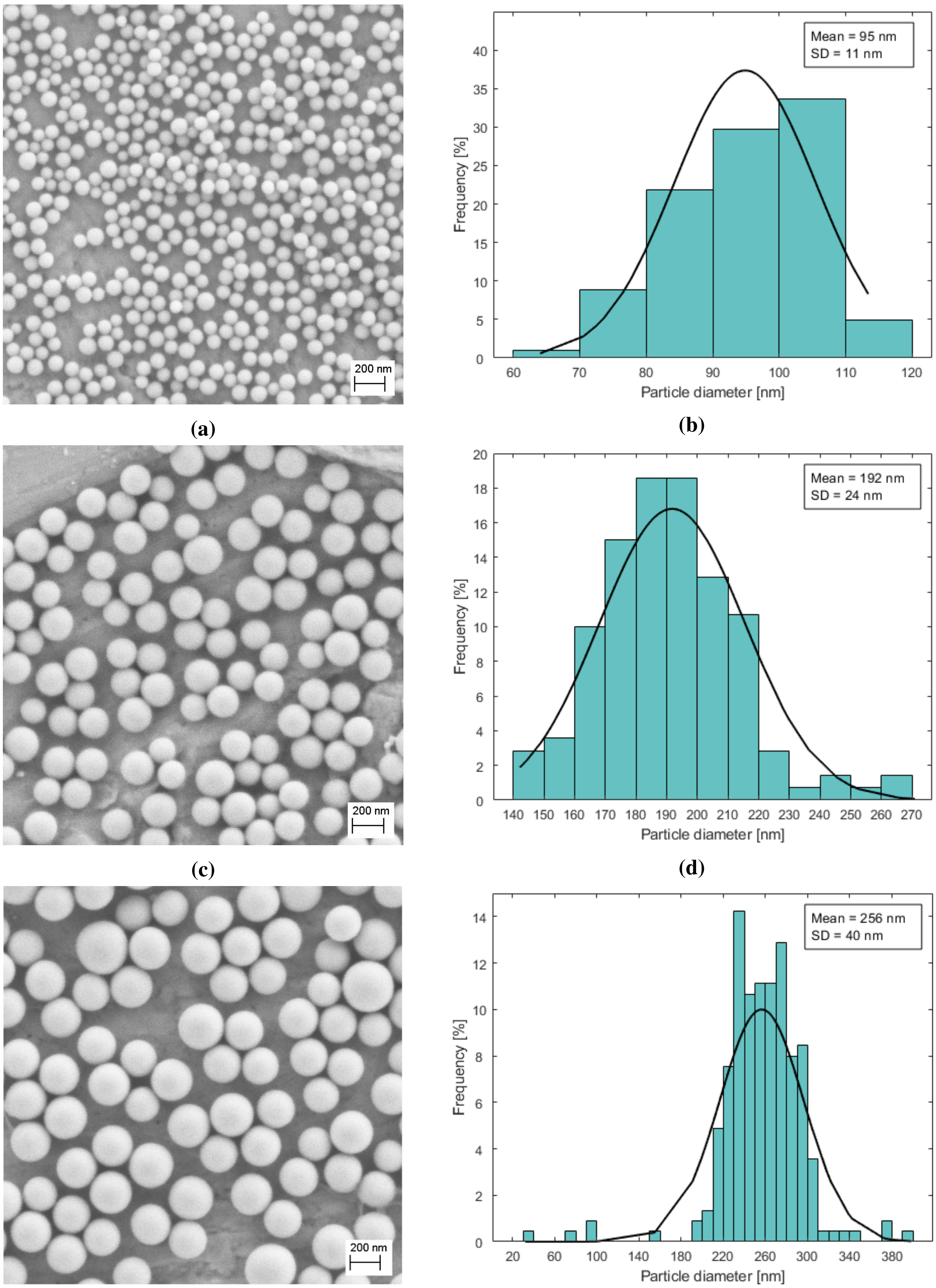

(a) **(b)**

(c) **(d)**

(e) **(f)**

Figure 4.2: FESEM images and particle size distributions of the SNP95, SNP192 and SNP256 silica sols with mean particle sizes of (a,b) 95 ± 11 nm, (c,d) 192 ± 24 nm and (e,f) 256 ± 40 nm, respectively.

4.2 Scattering properties of silica NPs

As colloidal silica is non-absorbing, the measured absorbance is a result of light being scattered away from its original direction of propagation, not absorbed [101]. Hence, absorbance spectra contain information about the light scattering properties of the silica NPs. As the particles are dispersed in a mixture of ethanol and water, both translucent liquids, they do not contribute to the recorded absorbance. The light attenuation thereby stems from the nanoparticles alone. The SNP95, SNP192 and SNP256 sols with initial concentrations given in Table 4.1 were diluted 10, 50 and 100 times prior to the absorbance measurements to avoid hitting the instrumental limit and to view the effect of particle concentration. The recorded UV-VIS spectra for the silica sols gave similar results as in the project work carried out by the author prior to this thesis [48]. For all three sols, a rise in absorbance towards lower wavelengths is observed, corresponding well with Rayleigh theory (Figure 4.3). That is, violet and blue light are scattered more than other colored light, making the sol appear slightly blue in color. The ”blueing” phenomenon is highly size dependent and tend to be less prominent for dispersions of larger particles [51]. This explains the blue tint observed for the SNP95 sol in Figure 4.1 and not for the sols containing larger particles. This is also seen from the close match of the absorbance curve for 722 mg/L of SNP95 with what predicted by Rayleigh theory (Figure 4.3a). The deviation from Rayleigh theory becomes larger with increasing particle size for the SNP192 and SNP256 sols, as seen in Figure 4.3 (a) and (b), respectively. This corresponds well with theory as the upper limit of Rayleigh scattering is $d/\lambda \leq 0.10$ [50]. The factor d/λ exceeds this limit for the SNP192 and SNP256 sols at all wavelengths and is only less than 0.10 for the SNP95 sol when $\lambda \geq 950$ nm.

As expected, higher absorbance was obtained for the more concentrated sols, demonstrating that the total light attenuation is higher when the dispersions contain more nanoparticles. For all three sols, increasing the mass concentration 10 times led to approximately a 10-fold increase in the absorbance at 300 nm.

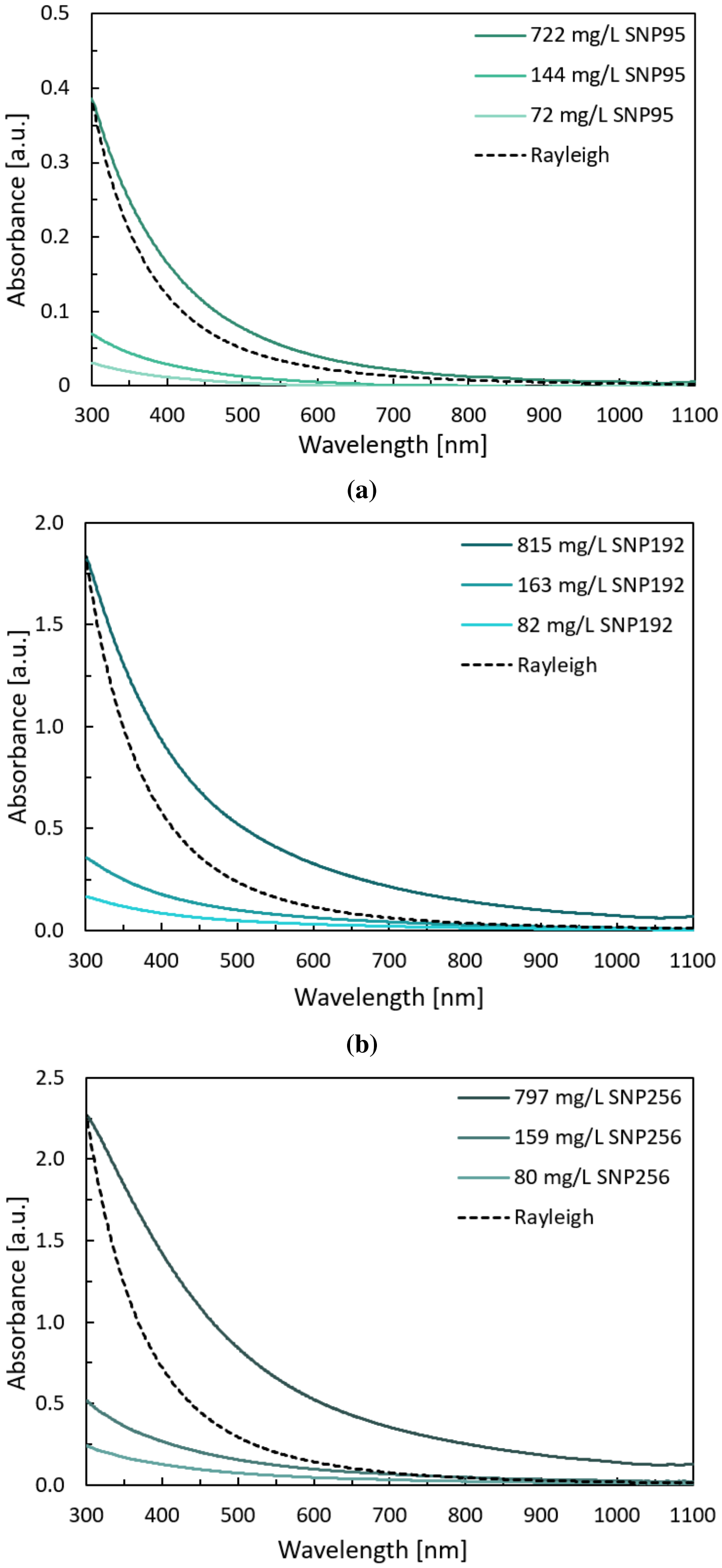

(a)

(b)

(c)

Figure 4.3: Absorbance of silica sols with different concentrations and mean particle sizes of (a) 95 nm, (b) 192 nm and (c) 256 nm. The expected Rayleigh scattering is plotted for the most concentrated samples.

4.2.1 Effect of particle size

To study the effect of particle size on the light scattering properties of the silica sols, absorbance spectra of theSNP95, SNP192 and SNP256 sols diluted to a NP concentration of approximately 0.05 NPs per cubic micron were measured and compared (Figure 4.4).

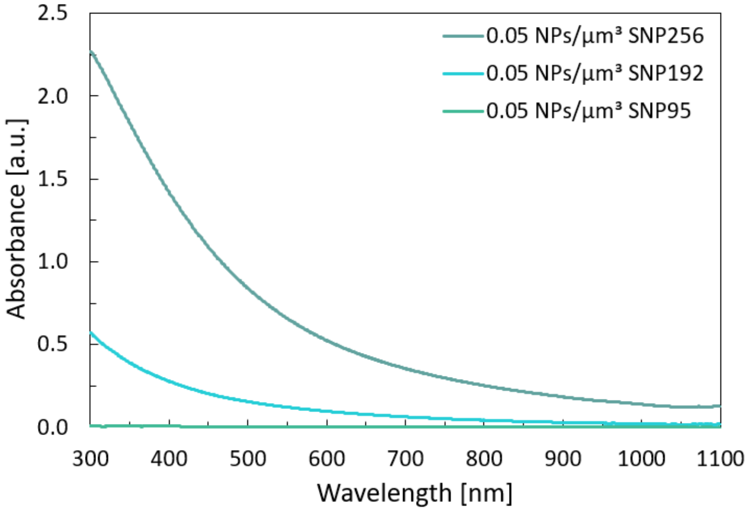

Figure 4.4: Measured absorbance for dispersions of silica NPs with the same NP concentration of 0.05 NPs/µm^3 but different particle sizes. The SNP95, SNP192 and SNP256 sol contains particles with a mean particle diameter of 95 ± 11 nm, 192 ± 24 nm and 256 ± 40 nm, respectively.

Higher absorbance, or extinction, of light was observed for the sols containing larger particles. This shows that more light is scattered away from its original direction of propagation by larger particles. However, with the same number of NPs in suspension, the total volume of silica NPs is larger for the larger particle sols. Whether the increased scattering is a result of the NPs interacting differently with light due to their sizes or simply a result of larger total scattering volume is therefore unclear. To evaluate this, UV-VIS spectra of the silica sols with the same mass concentration of 40 mg/L were also recorded (Figure 4.5).

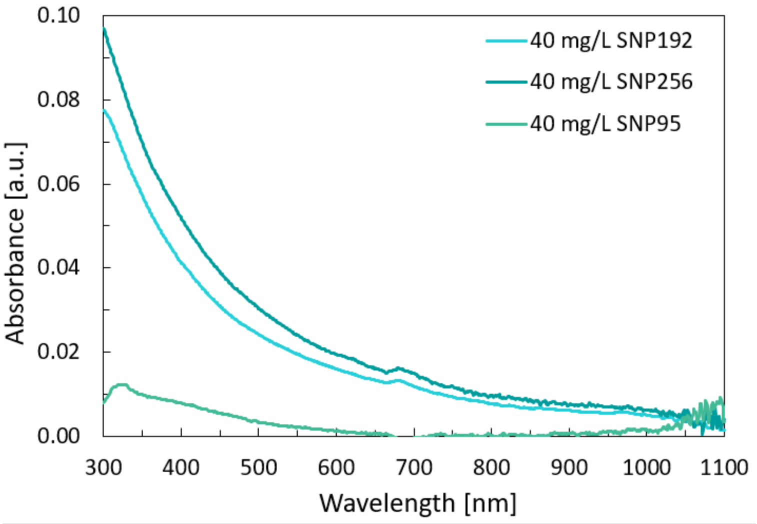

Figure 4.5: Measured absorbance of silica NP sols with the same mass concentration of 40 mg/L but different particle sizes. The SNP192 and SNP256 sol contains particles with a mean particle diameter of 192 ± 24 nm and 256 ± 40 nm, respectively.

With the same mass concentrations, the differences in absorbance between the SNP95, SNP192 and SNP256 sols were significantly smaller than with the same number of NPs per cubic micron (Figure 4.4). The total volume of silica particles hence greatly affects the recorded extinction. Still, the SNP95 sol displayed very little alteration of the light path away from the detector compared to the other sols, even with similar mass concentrations. The smallest particles of 95 nm can, therefore, be regarded as weak scatters. With a mass concentration of 40 mg/L, the measured absorbance for SNP192 and SNP256 were 0.077 and 0.095 a.u., respectively (Figure 4.5). Thus, a 23% increase in absorbance was found when increasing the mean particle size by 64 nm.

4.3 Synthesized silver colloids

4.3.1 Silver NPs obtained in the study of the citrate method

Upon addition of trisodium citrate to the dissolved silver nitrate, the solution was initially clear, but after approximately 2-3 minutes of boiling it became slightly orange. The orange color indicated that spherical silver particles had begun to form, due to their localized surface plasmon resonance in the violet-blue region [63]. Light of these wavelengths are scattered more strongly than the rest, causing the dispersion to appear orange in transmitted light. With increasing boiling time the sol became darker and more milky in appearance with a green/grey color, finally resulting in a turbid appearance. This was observed for all of the AgNP#1, AgNP#2, AgNP#3 and AgNP#4 colloids, prepared by variations of the classic Lee-Meisel method (Figure 4.6). Similar observations has also been done by others [108, 109].

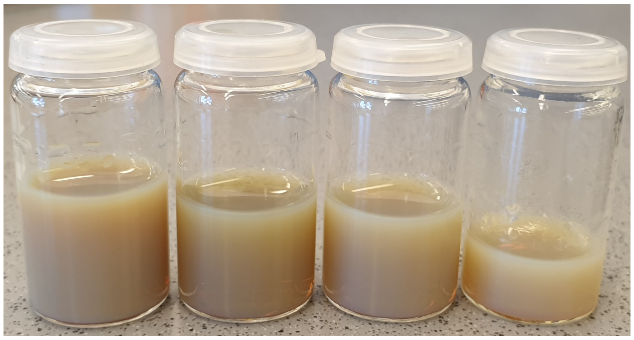

Figure 4.6: Image of the final colloids prepared by variations of the Lee-Meisel citrate method. From left to right, the AgNP#1, AgNP#2, AgNP#3 and AgNP#4 colloid.

When diluted 1:6 with DI-water and studied by spectrophotometry, a peak in absorbance was observed in the region of 400 nm to 450 nm for all of the AgNP#1-#4 colloids (Figure 4.7). At the time that the UV-VIS spectra were recorded, the AgNP1 colloid had been stored for 13 days and AgNP#2 for 7 days at room temperature whilst the AgNP#3 and AgNP#4 samples were analyzed straight after synthesis. Based on the stability tests presented in later sections, it is likely that the absorbance curve of AgNP#2, prepared with a short reaction time of 5 minutes, has increased some during this period. If measured directly after synthesis, the curve for AgNP#2 may have been shifted downwards.

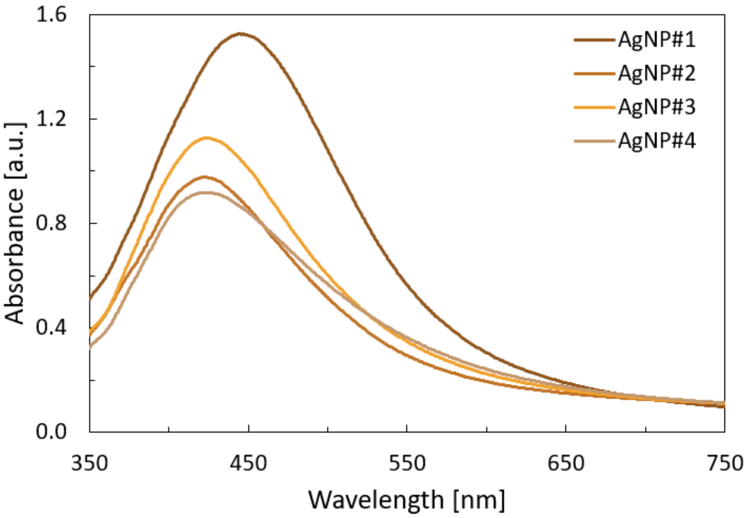

Figure 4.7: Measured absorbance of the AgNP#1, AgNP#2, AgNP#3 and AgNP#4 silver colloids prepared by variations of the Lee-Meisel citrate method.

The AgNP#1 colloid gave a higher absorbance peak than the others, indicating the presence of larger silver spheres or a higher NP concentration. For all four colloids, the relatively broad LSPR bands indicated a wider size distribution. This is a common result when applying variations of the citrate reduction method, as demonstrated by Meng *et* al. [110], due to the continuous nucleation and growth of silver seeds. The wavelength of maximum absorbance, λ_{max}, the maximum absorbance intensity, Abs_{max}, and the full width half maximum of each spectrum were calculated and are presented in Table 4.2.

Table 4.2: Wavelength of maximum absorbance, λ_{max} [nm], corresponding absorbance intensity, Abs_{max} [a.u.] and peak width given by the full width half maximum, FWHM[nm], for the synthesized silver colloids diluted at a ratio of 1:6.

Colloid	λ_{max} [nm]	Abs_{max} [a.u.]	FWHM [nm]
AgNP#1	444	1.525	153
AgNP#2	423	0.976	140
AgNP#3	424	1.126	137
AgNP#4	423	0.918	155

As well as displaying the highest maximum intensity, λ_{max} was also largest for the AgNP#1 colloid, again implying the presence of bigger particles. In the AgNP#1 synthesis a lower temperature of 93°C was applied, reducing the reaction rate and slowing the nucleation process. This can lead to the formation of fewer, but larger, silver particles [110]. For the other colloids, λ_{max} was around 423 nm, corresponding well with literature [63]. The AgNP#2 colloid had one of the lower Abs_{max} of the group. During this synthesis, a higher concentration of TSC was used which can have led to an initial higher reaction rate and faster nucleation. The solution was removed from the heat after only 5 minutes, which then would have slowed the reaction. The same procedure was applied in the synthesis of both the AgNP#3 and AgNP#4 colloids, however, when comparing their absorbance spectra, some difference was observed. This may have been caused by the withdrawal of samples throughout the synthesis of AgNP#. This can potentially have affected the resulting particles, as it interfered with the reaction solution and reduced the total reaction volume after each withdrawal. Also, the AgNP#4 sample withdrawn at 90 minutes were rapidly cooled in an ice bath which the AgNP#3 colloid was not.

Investigation in FESEM confirmed that nanoparticles had been achieved in all four experiments applying different adaptations of the Lee-Meisel citrate method. The images revealed that not only spherical particles had been obtained, but also cubic, hexagonal and elongated nanoparticles as well as nanorods (Figure 4.8). The spherical, or quasi-spherical, particles do however appear to dominate. The different shapes also varied in size. In the AgNP#3 colloid, however, some agglomerates or aggregates be observed, as seen in Appendix C.

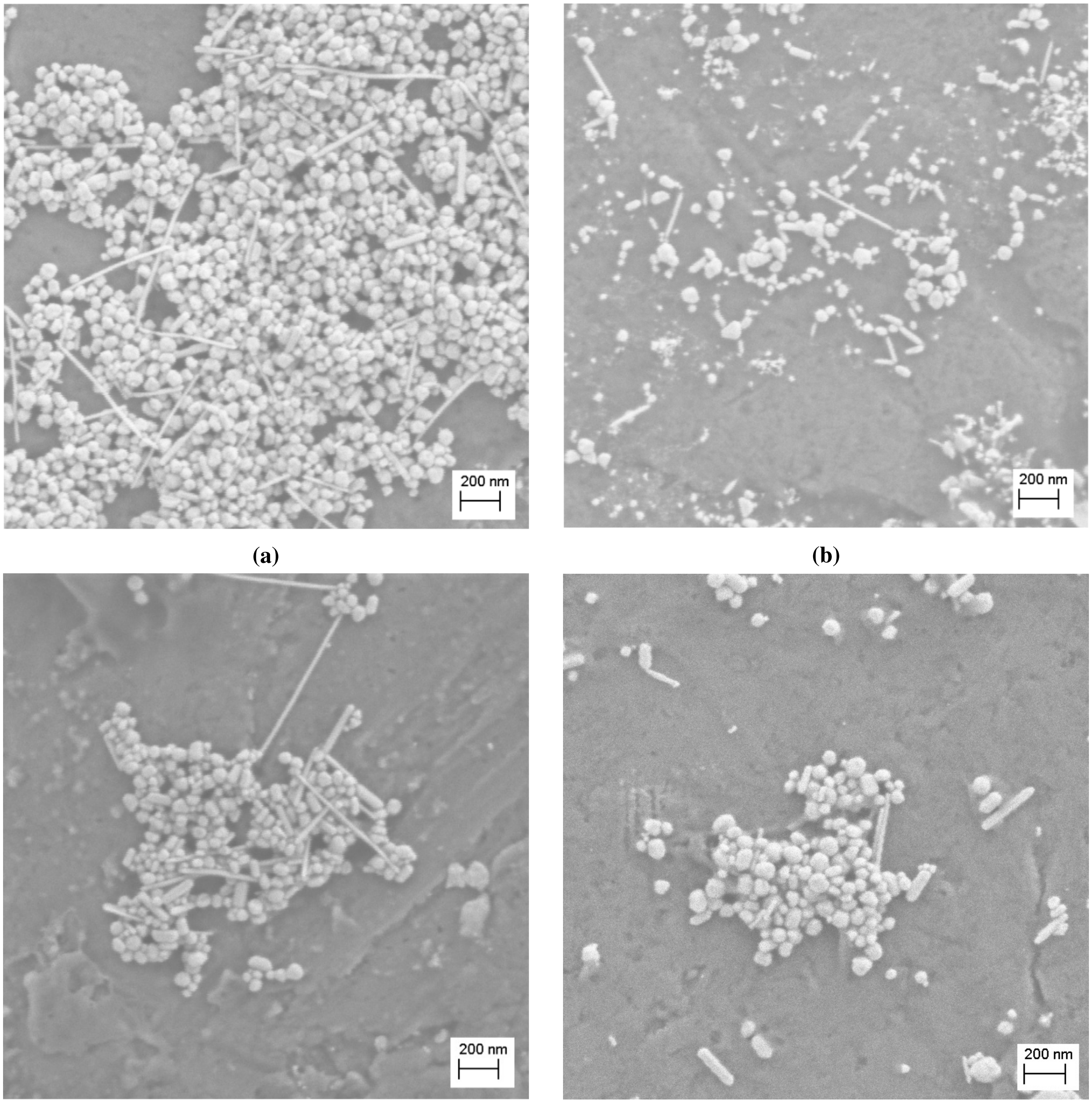

(a) **(b)** **(c)** **(d)**

Figure 4.8: FESEM images of silver NPs from the synthesized colloids (a) AgNP#1, (b) AgNP#2, (c) AgNP#3 and (d) AgNP#4.

The varying shapes and sizes are common for this synthesis due to the weak reducing agent being used, and have also been reported by others [65, 84, 110, 111]. As seen in Figure 4.8, when leaving a drop of the NP dispersions on the specimen stub to allow for solvent evaporation, the particles have a tendency of gathering together. This makes it hard to view the individual particles and to determine the particle size distribution using ImageJ. Due to the uneven surface of the specimen stubs, particles were also observed to fall into cracks and pits. It should therefore be noted that the presented FESEM images not necessarily are representative for the colloid. In Figure 4.8 (a) from AgNP#1 a large number of particles were imaged compared to the other images, corresponding well with the absorbance spectrum. During the investigation of the sample from AgNP#2 (Figure 4.8b) no large clusters of nanoparticles were observed. As shown in 4.8 (b), some particles with similar shapes and sizes as in the other cases was obtained, but a large number of much smaller particles were also observed. This indicates that with a shorter reaction time of 5 minutes the reduction of silver nitrate might not have gone to completion, resulting in fewer and smaller particles. For the AgNP#3 and AgNP#4 colloids presented in 4.8 (c) and (d), respectively, visual inspection in FESEM did not reveal any obvious differences.

4.3.2 Effect of reaction time

Following the original Lee-Meisel citrate method but applying a different boiling time was considered as a way to obtain silver colloids with optimal characteristics for the application in this thesis. Spherical silver particles are wanted for a maximum plasmon resonance effect and uniform sizes are valued in order to relate any observed effects to silver particles with a specific size and shape. Additionally, the colloid should be stable for some time to avoid the optical properties changing during growth experiments. Good stability is also important for potential up-scale implementations of such NP dispersions to microalgae biomass production. The effect of reaction time was studied based on the UV-VIS spectra obtained for samples withdrawn from the AgNP#4 solution at different reaction times. As previously seen, a color change from clear to light yellow was observed after approximately 3 minutes after the TSC reducing agent was added. During the first 10 minutes of reaction, the color evolved rapidly from yellow to orange, and eventually to a darker brown-grey turbid appearance (4.9).

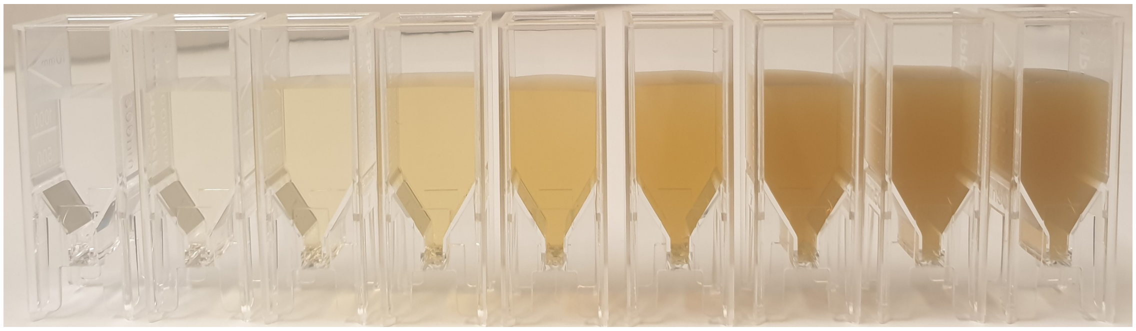

Figure 4.9: The color evolution of the AgNP#4 colloid prepared by the Lee-Meisel citrate method during the first 10 minutes of reaction. From left to right, a blank sample containing water and samples withdrawn at a boiling time of 3, 4, 5, 6, 7, 8, 9 and 10 minutes.

When left to boil for more than 10 minutes, only slight variations of a dark brown-grey color could be observed. The initially rapid color change is a reflection of the reduction of silver nitrate and the subsequent nucleation and growth mechanism. The darker color corresponds with the growth of silver seeds and higher NP concentrations. The measured absorbance spectra for each sample withdrawn from the AgNP#4 colloid and diluted with DI-water at a ratio of 1:6 is presented in Figure 4.10. As in previous UV-VIS analyses, diluting the samples prior to measurements was necessary in order to avoid hitting the instrumental limit.

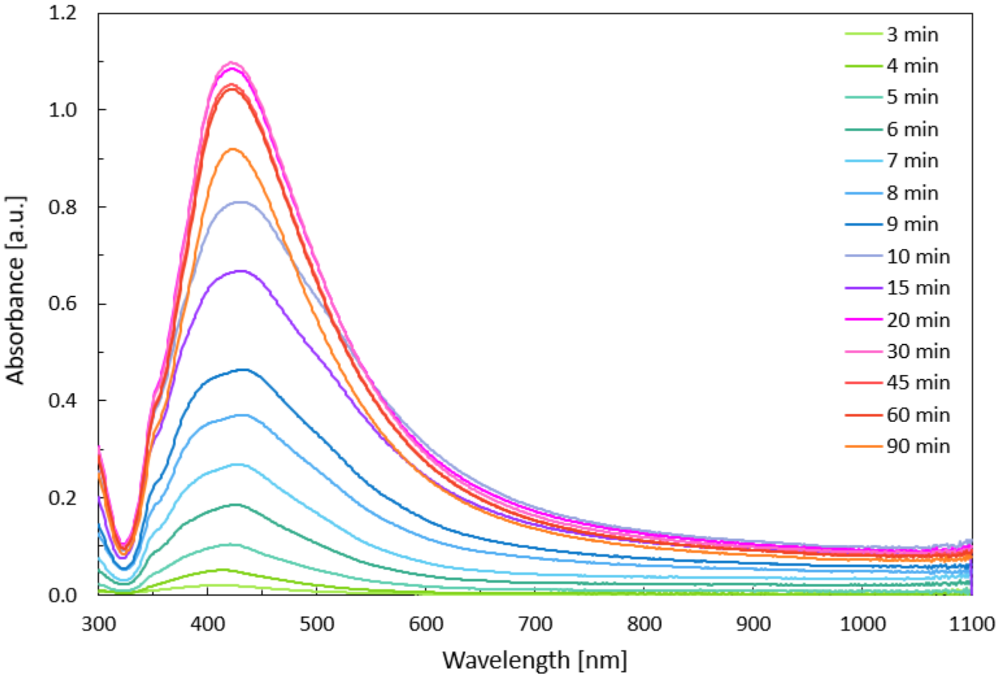

Figure 4.10: Effect of reaction time on the measured absorbance of the AgNP#4 silver sol prepared by the Lee-Meisel citrate method. Samples were withdrawn after 3, 4, 5, 6, 7, 8, 9, 10, 15, 20, 30, 45, 60 and 90 minutes of boiling.

As seen from the absorbance spectra, the maximum absorbance intensities, corresponding peak positions, and the peak widths were all affected by the reaction time (Table 4.3). After 3-4 minutes, the solution displayed weak absorbance at around 413 nm. This is a sign that the reaction was in its stage of nucleation and silver seed formation. As the reaction proceeded, both λ_{max}, the absorbance peak intensity and the FWHM increased rapidly up until the 10 minute mark. This indicates growth of the already formed silver seeds as well as continuous nucleation and formation of new seeds. After 20 minutes, a shift towards lower wavelengths was observed for the LSPR peak position, going from 432 nm to 421 nm in 5 minutes. This implies that the mean particle size became smaller, likely due to the dispersion of previously formed agglomerates. The blue shift of λ_{max} was accompanied by a reduction in band with, which also is a sign of smaller sizes [62].

Table 4.3: Wavelength of maximum absorbance, λ_{max} [nm], corresponding absorbance intensity, Abs_{max} [a.u.] and broadening of the absorbance band given by the full width half maximum, FWHM[nm], for samples withdrawn from the AgNP#4 silver sol at given reaction times [min].

Time [min]	λ_{max} [nm]	Abs_{max} [a.u.]	FWHM [nm]
3	411	0.020	118
4	414	0.051	119
5	421	0.104	138
6	425	0.185	157
7	428	0.269	168
8	432	0.371	186
9	432	0.464	191
10	430	0.811	204
15	432	0.668	200
20	421	1.084	159
30	421	1.097	157
45	422	1.053	156
60	422	1.043	155
90	423	0.918	155

Based on the reaction stages reported by Meng *et* al. [110], the onset of the blue shift is correlated with there not being any silver ions left in solution, and hence no nucleation. Therefore, the observed increase in Abs_{max} after 20 minutes should be a result of the more narrow size distribution and not a larger total particle volume. When left under boiling and stirring for more than 20 minutes, the λ_{max} started to slightly increase again from 421 nm to 423 nm when left to boil until a total reaction time of 90 minutes (Table 4.3). At the same time, the LSPR band became slightly more narrow, going from 159 nm to 155 nm where it appeared to eventually stabilize. These observations may be a sign of Ostwald ripening, where larger particles grow at the expense of smaller ones, resulting in a larger mean particle size. The peak position stabilized at around 422 nm, similar to what expected according to Lee and Meisel [63].

The reaction time also affected the shape of the measured absorbance spectra. A shoulder at around 350 nm can be observed for all samples, which based on the results obtained by Wiley *et* al. [66] can imply that cubic nanoparticles were present. At around 380-400 nm another small shoulder could be observed, which again can be related to cubic shapes. The two shoulders may also originate from particles coalescing or forming aggregates. The relative intensity of the shoulder at 350 nm compared to the maximum absorbance intensity appeared to be higher earlier in the reaction. During the first 15 minutes, this shoulder became less noticeable with increasing reaction time. This suggests that more monodisperse NP populations are achieved when heat is supplied to the reaction solution for a longer period.

Lastly, the stability of the silver sols was also found to be influenced by the reaction time. The evolution of the absorbance spectra after being stored for 1 and 2 weeks is presented in Figure 4.11 for some chosen samples. For reference, the corresponding absorbance spectra measured for the freshly prepared samples are also included.

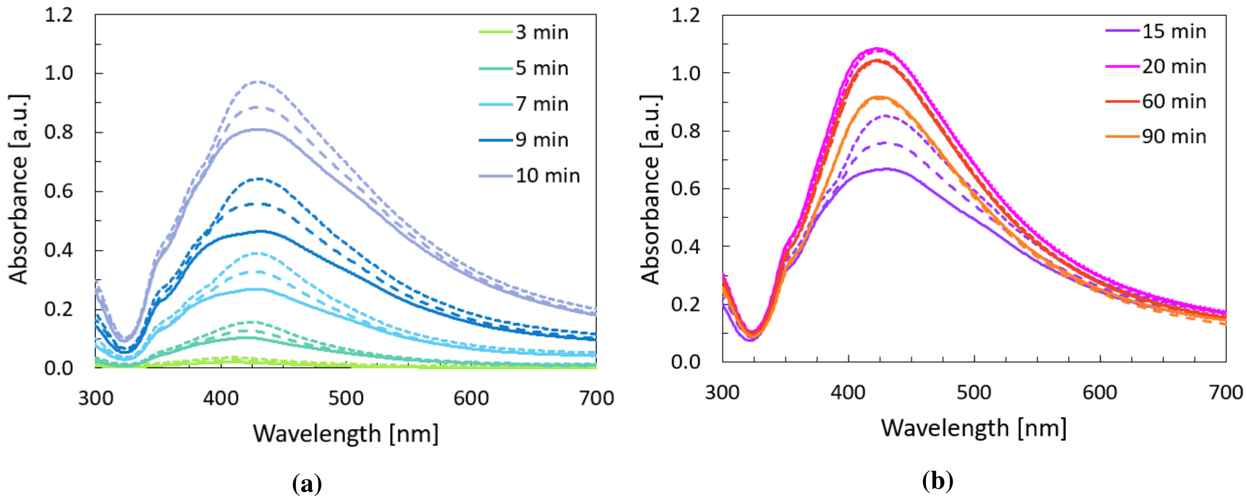

(a)

(b)

Figure 4.11: Evolution of the absorbance spectra after 1 and 2 weeks for samples withdrawn from AgNP#4 (a) after 3-10 minutes and (b) after 15-90 minutes of boiling. The solid curves show the initial spectra and spectra obtained after 1 and 2 weeks are given by large and small dotted curves, respectively.

For the sols withdrawn after 30, 60 and 90 minutes the solid and dotted curves are closely overlapping, indicating little to no change in particle size, morphology and concentration. Samples taken earlier in the reaction process, however, displayed a noticeable change in absorbance after 1 week and even more so after 2 weeks. An increase in maximum absorbance intensity as well as higher total scattering was observed. This implies that the reduction of silver ions continued after the synthesis, leading to particle growth. Improved colloid stability is achieved when the reaction is allowed to proceed for more than 15 minutes.

Based on the observations done in this study, a boiling time of 60 minutes was adopted for the synthesis of the silver NPs used in the later algae growth experiment. Thus, the same boiling time as reported in the classical citrate method by Lee and Meisel [63] of about 1 hour was used. Boiling times of 15 minutes or less were not considered due to their poorer colloid stability. Even though the highest peak intensity was obtained with a boiling time of 30 minutes, the FWHM was lower and appeared to stabilize after a boiling time of 60 minutes (Table 4.3). In this application, where the effect of a certain silver NP suspension on biomass productivity will be evaluated, particle stability and a narrow size distribution were deemed to be especially important in order to better correlate any observed effect to a specific particle size or characterization. More so than achieving a particular particle size, which, if having a broad size distribution or changing throughout the experiments, would not be as easily correlated to the observed effects. When comparing to the reaction time of 90 minutes, 60 minutes was chosen due to its larger plasmon resonance effect with an SPR intensity of 1.043 a.u. compared to 0.918 a.u.

4.3.3 Silver colloid prepared for use in algae growth experiment

The silver colloid used in the growth experiment was obtained with a mean particle diameter of 57 ± 14 nm and a mass concentration of 113 ± 12 mg/L. This corresponded to a NP concentration of 0.11 ± 0.01 NPs/μm^3. From now on, this colloid will be referred to in terms of its sol ID, AgNP57. Upon inspection in FESEM, quasi-spherical particles of similar sizes were observed, as well as some elongated shapes and nanorods (4.12).

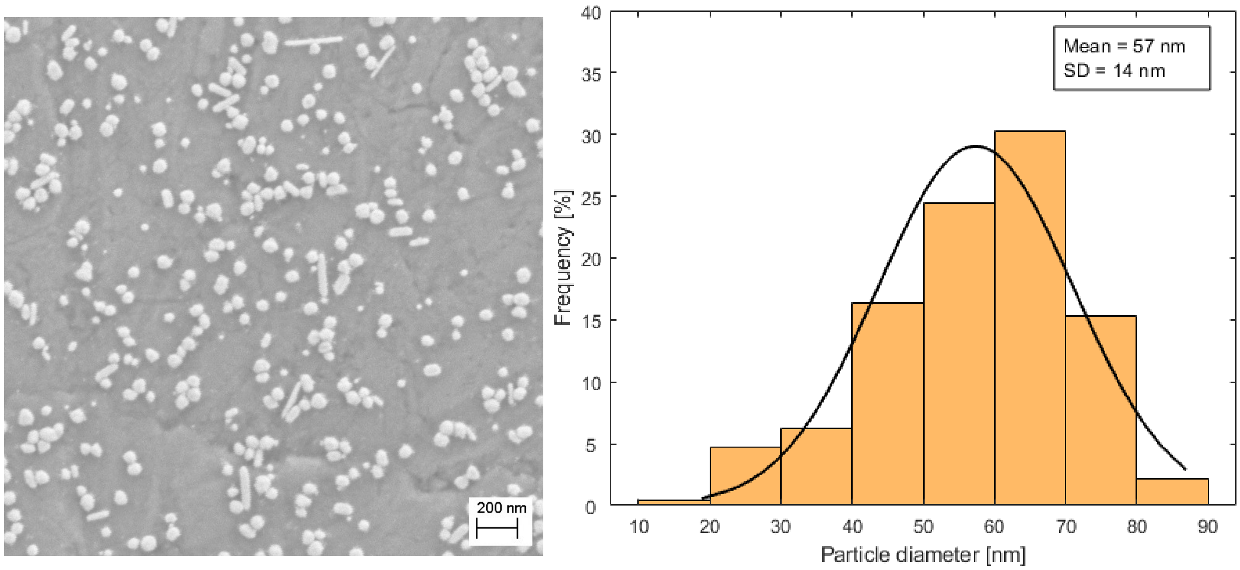

(a)

(b)

Figure 4.12: (a) FESEM image and (b) particle size distribution of the AgNP57 colloid with a mean particle size of 57 ± 14 nm, synthesized for use in the algae growth experiment.

Again, the final colloid was dark gray/brown, but displayed the characteristic yellow/orange color of silver colloids when diluted 1:6 with DI-water (Figure 4.13).

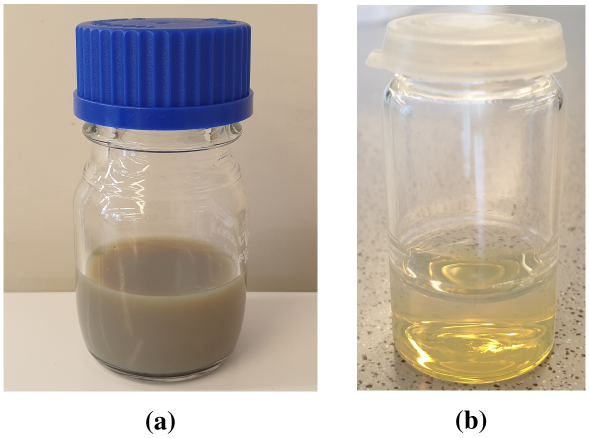

(a) (b)

Figure 4.13: Photo of the AgNP57 colloid with mean particle size of 57 ± 14 nm (a) as synthesized with a mass concentration of 113 mg/L and (b) diluted 1:6 with DI-water to 18.8 mg/L for UV-VIS measurements.

The AgNP57 colloid displayed strong scattering at 431 nm with a maximum LSPR intensity, Abs_{max}, of 1.570 a.u. and a FWHM of 123 nm. Again, a shoulder at around 350 nm was observed, associated with the presence of less symmetrical shapes such as cubic particles (Figure 4.14).

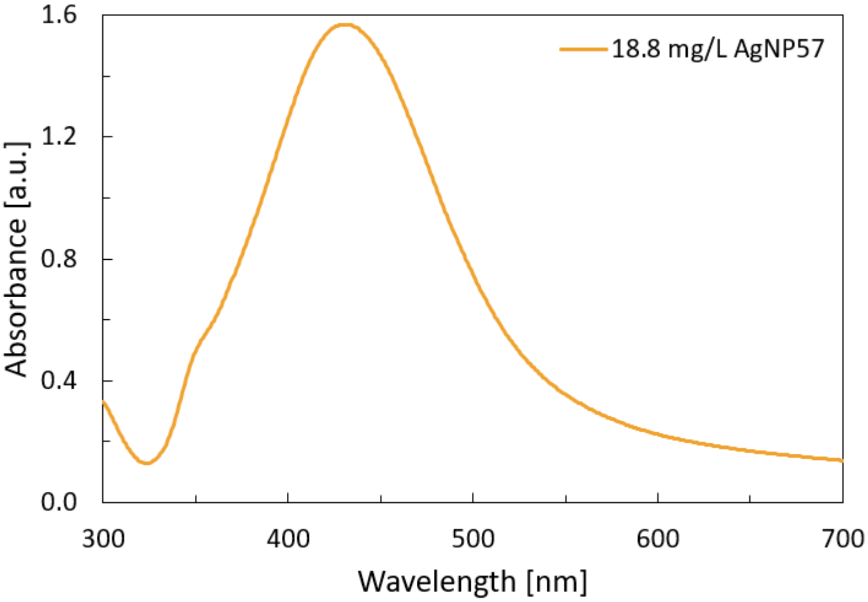

Figure 4.14: Measured absorbance of the freshly prepared AgNP57 silver colloid diluted 1:6 with DI-water. Synthesized by the Lee-Meisel citrate method with a reaction time of 60 minutes.

Compared to the AgNP#4 sample withdrawn after 60 minutes, which were prepared by the same method, λ_{max} for AgNP57 was shifted more towards longer wavelengths, indicating larger particles. Generally, the LSPR band for larger particles is expected to also have wider peaks. However, in this case, the contrary was observed. For AgNP57, the FWHM was found to be 123 nm whilst for the AgNP#4 sample it was 155 nm even though $\lambda_{\max}$ was smaller. This suggests that a more narrow size distribution was obtained for the AgNP57 suspension. The relatively high maximum absorbance intensity of 1.570 also indicates that the total volume of silver particles with strong plasmon resonances was higher in this case.

4.4 Angular scattering distribution

Different angular scattering distributions were obtained for the SNP95, SNP192 and SNP256 silica particles as well as for the AgNP57 silver particles used in the growth experiments (Figure 4.15). Natural light entering from the left is scattered by either a silica or silver sphere located at the center of the plot. For all four curves, the intensity of the scattered light has been normalized to the scattered intensity in the forward direction (at a scattering angle of 0°).

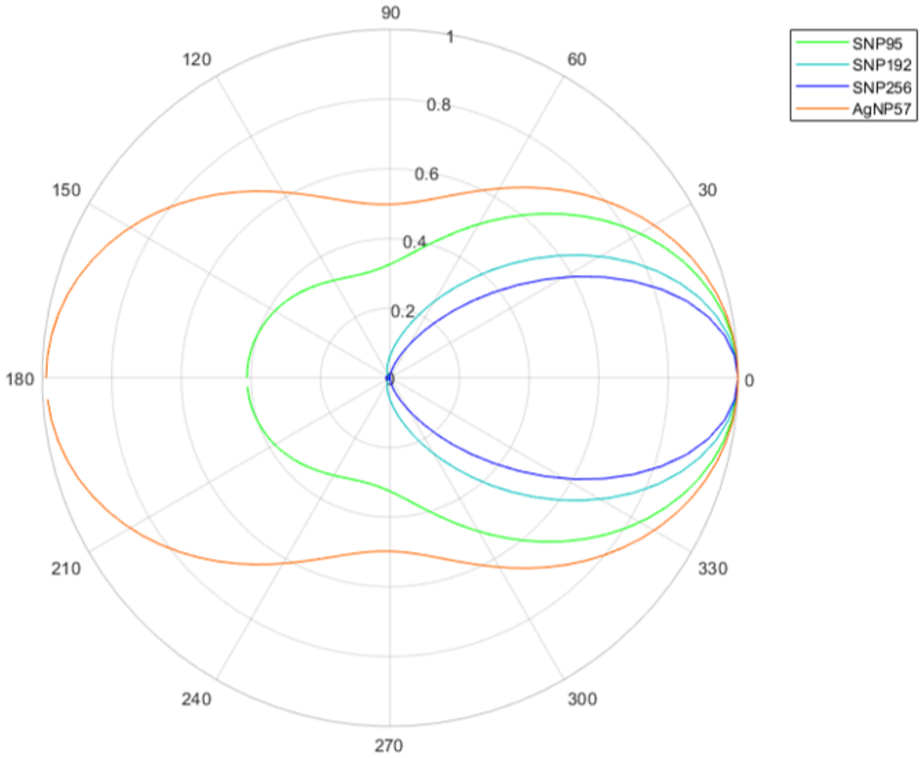

Figure 4.15: Angular distribution of violet light (400 nm) scattered by silica spheres dispersed in ethanol or silver spheres in an aqueous medium. The SNP95, SNP192 and SNP256 curves represent scattering by silica spheres with a mean size of 95, 192 and 256 nm, respectively. AgNP57 shows scattering by silver spheres of 57 nm. The intensity of the scattered light has been normalized to the intensity scattered at an angle of 0°. Calculated with the code created by Scott Prahl available at `http://omlc.org/calc/mie_calc.html` (accessed 26.06.20).

Upon interaction with the smallest silica NPs of 95 nm, a portion is seen to be backscattered whilst the majority is scattered at varying angles in the forward direction. With larger particle sizes the pattern of the scattered light becomes increasingly anisotropic and forward peaking, as expected from literature [35]. For the 256 nm silica spheres, a narrow angular scattering range of ± 30° is obtained in the forward direction. Conversely, the scattering pattern obtained for silver spheres of 57 nm is more symmetric, with a large portion scattered back towards the light source.

4.5 Nanoparticle structure and composition

The X-ray diffraction (XRD) pattern of the SNP192 sample was diffuse and showed no signs of crystallinity . The particles synthesized by the Stöber method [75] were hence found to be amorphous, as expected from literature [52]. The XRD pattern of the silica particles as well as that obtained with the silver AgNP57 sample are presented in Figure 4.16 (a) and (b), respectively.

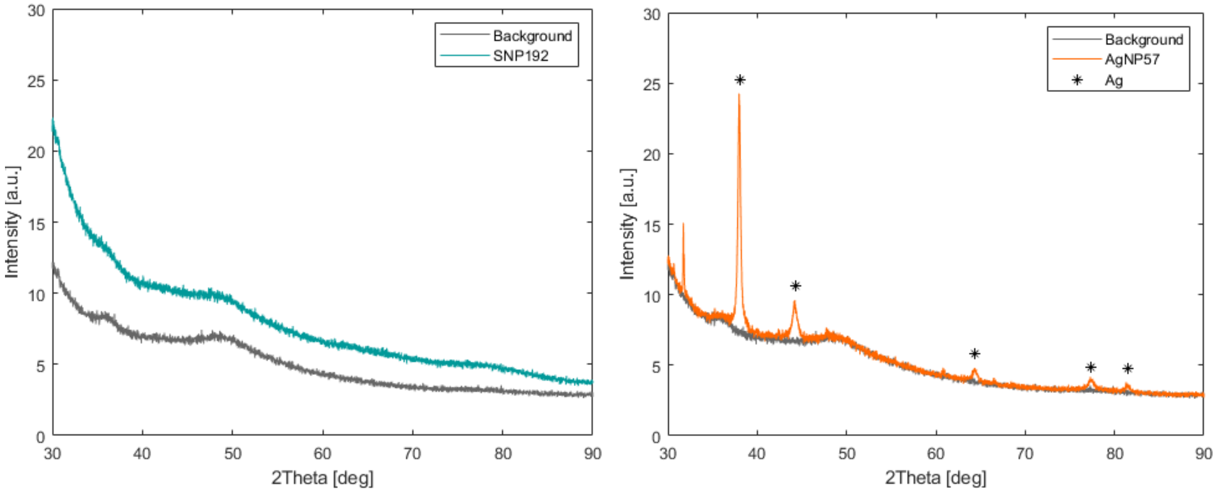

(a) (b)

Figure 4.16: XRD pattern of (a) the SNP192 silica particles and (b) the AgNP57 silver particles.

The XRD pattern obtained for the AgNP57 sample is discrete, indicating a crystalline structure. The five marked peaks in Figure 4.16 (b) at 2Theta values of 38.138, 44.276, 64.414, 77.379 and 81.488 correspond with that of pure silver, listed in the Crystallography Open Database (COD) with COD-ID 9008459. The peak at 31.724 is much more narrow than the rest and does not match with elemental silver, hence it likely stems from an unidentified impurity. The XRD study confirms that the particles formed using the Lee-Meisel citrate method are indeed crystalline silver (FCC, space group Fm$\bar{3}$m). The narrow peaks obtained for the AgNP57 sample indicates small particles. When using the Debye-Scherrer method in EVA on the peak at 38.138, the crystallite size was estimated to be 29 nm. This corresponds well with the particle size 57 nm that was obtained based on the

FESEM images, as the observed particles can be made up of one or more crystallites with the same sizes or a range of sizes.

4.6 Stability of the synthesized colloids

4.6.1 Effect of prolonged storage on SNP95 sol stability

For the SNP95 sol previously synthesized by the author in the project work preceding this thesis [48], the stability after being stored at 6°C for a prolonged period was investigated. After 5 months, a small decline in the measured absorbance intensity was observed (4.17). This indicates that the silica sol may have had a slightly lower scattering effect after the storage period, still the change is very small .

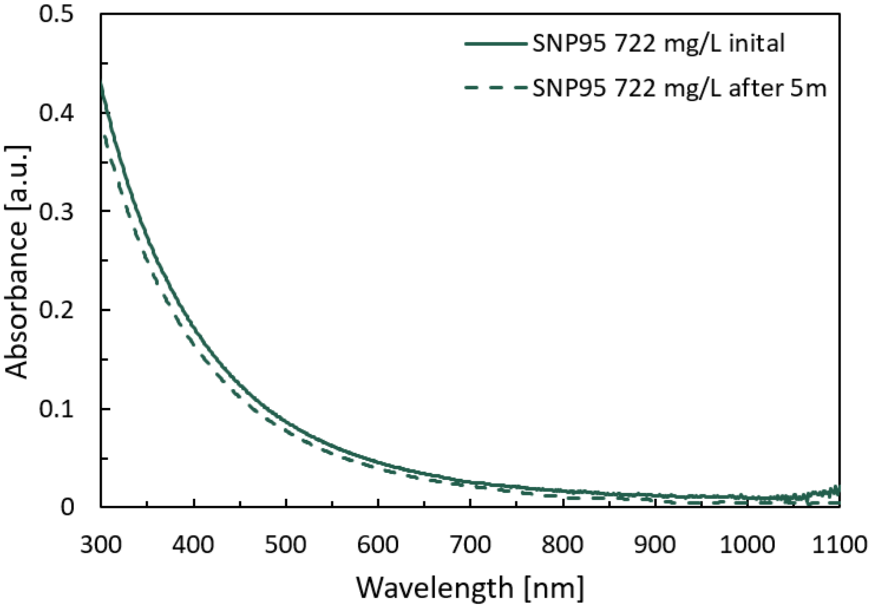

Figure 4.17: Measured absorbance of the SNP95 sol with a mass concentration of 722 mg/L 2 weeks after synthesis and after being stored at 6°C for 5 more months. The initial spectra was recorded by the author during the project work preceding this thesis [48].

The particles were also examined in the FESEM to check for any changes in particle morphology and size compared to the original images obtained 2 weeks after synthesis. A slight increase in particle size is observed (Figure 4.18), as reflected with the initially calculated mean particle size of 67 nm [48] and the larger mean size of 95 nm obtained in the present work. However, the calculated size is highly dependent on the specific FESEM image and selection of particles used in the PSD analysis. Uncertainty in the PSD determination may therefore have contributed to this.

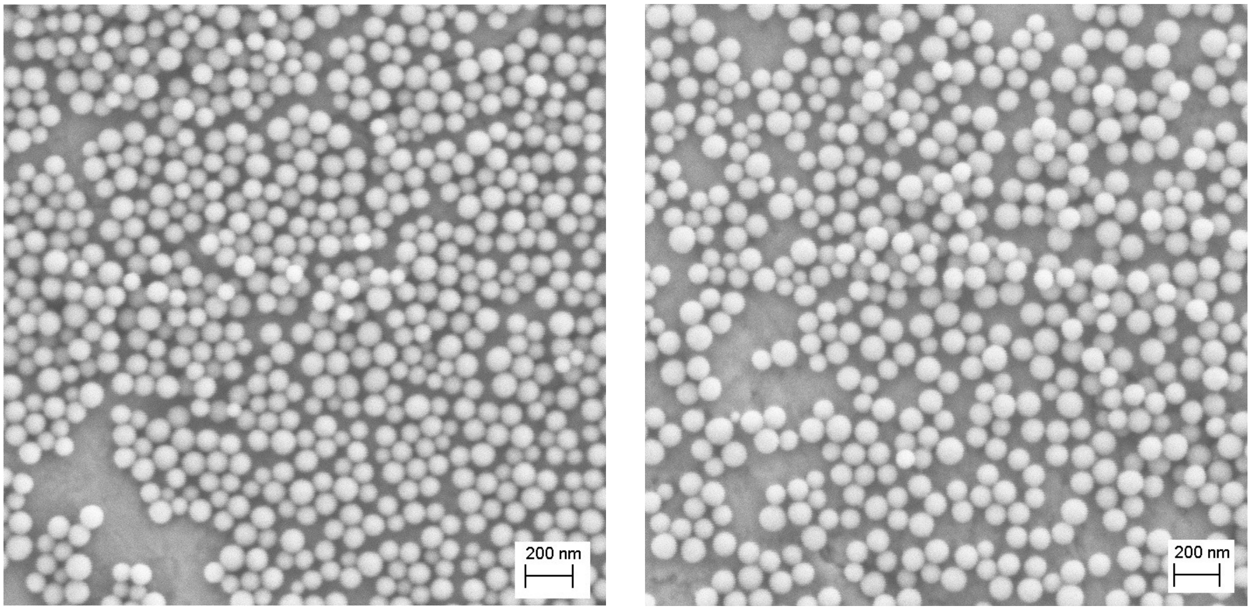

(a) (b)

Figure 4.18: FESEM images of the SNP95 particles obtained (a) 2 weeks after synthesis (taken by the author in the project work preceding this thesis [48]) and (b) after 5 more months of being stored at 6°C.

Investigation in FESEM of the SNP95 sol after 5 months also revealed the presence of aggregated particles (4.19).

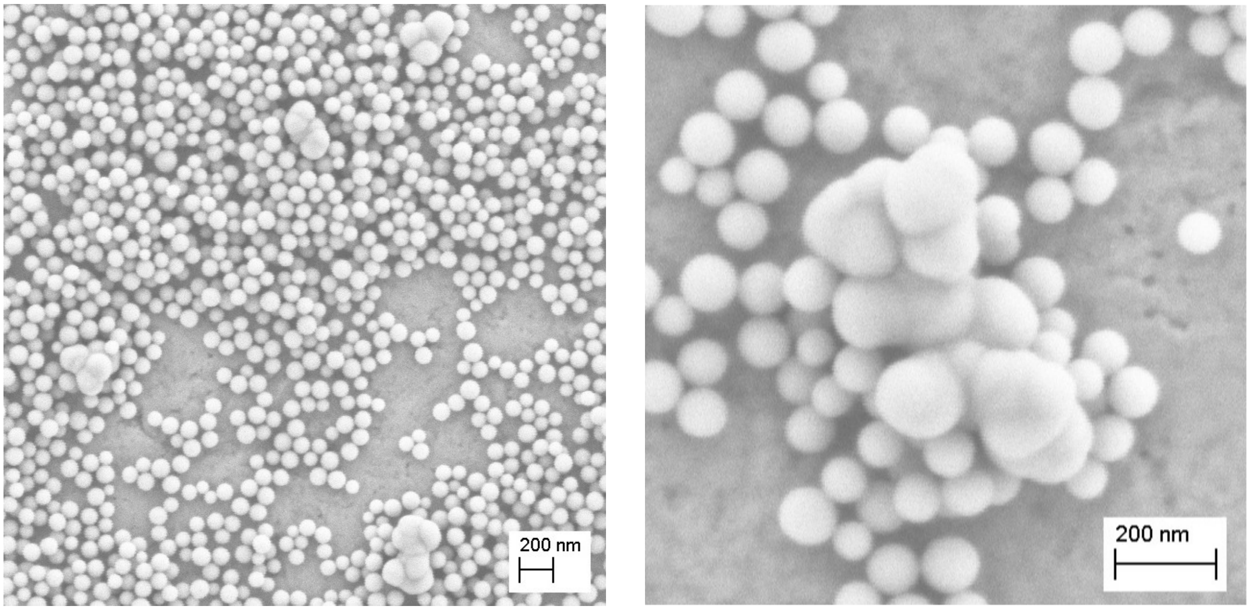

(a) (b)

Figure 4.19: Aggregated particles in the SNP95 sol after 5 moths of storage at 6°C. Showing (a) four aggregates in close proximity and (b) a close-up of a larger aggregate.

This could indicate that increased particle coalescence occurs when stored for a longer period of time. Still, the possibility that the aggregates also were present in the freshly prepared sol cannot be ruled out.

4.6.2 Effect of storage temperature on silica and silver NP suspensions

The effect of storage temperature on colloid stability was investigated for the NP suspensions used in the later growth experiments. The absorbance spectra of the NP suspensions were recorded at the start of each respective growth experiment and after 1 week of being stored at 6°C or at room temperature. In Figure 4.20 the evolution of the absorbance spectra are plotted for (a) SNP192, (b) SNP256 and (c) AgNP57.

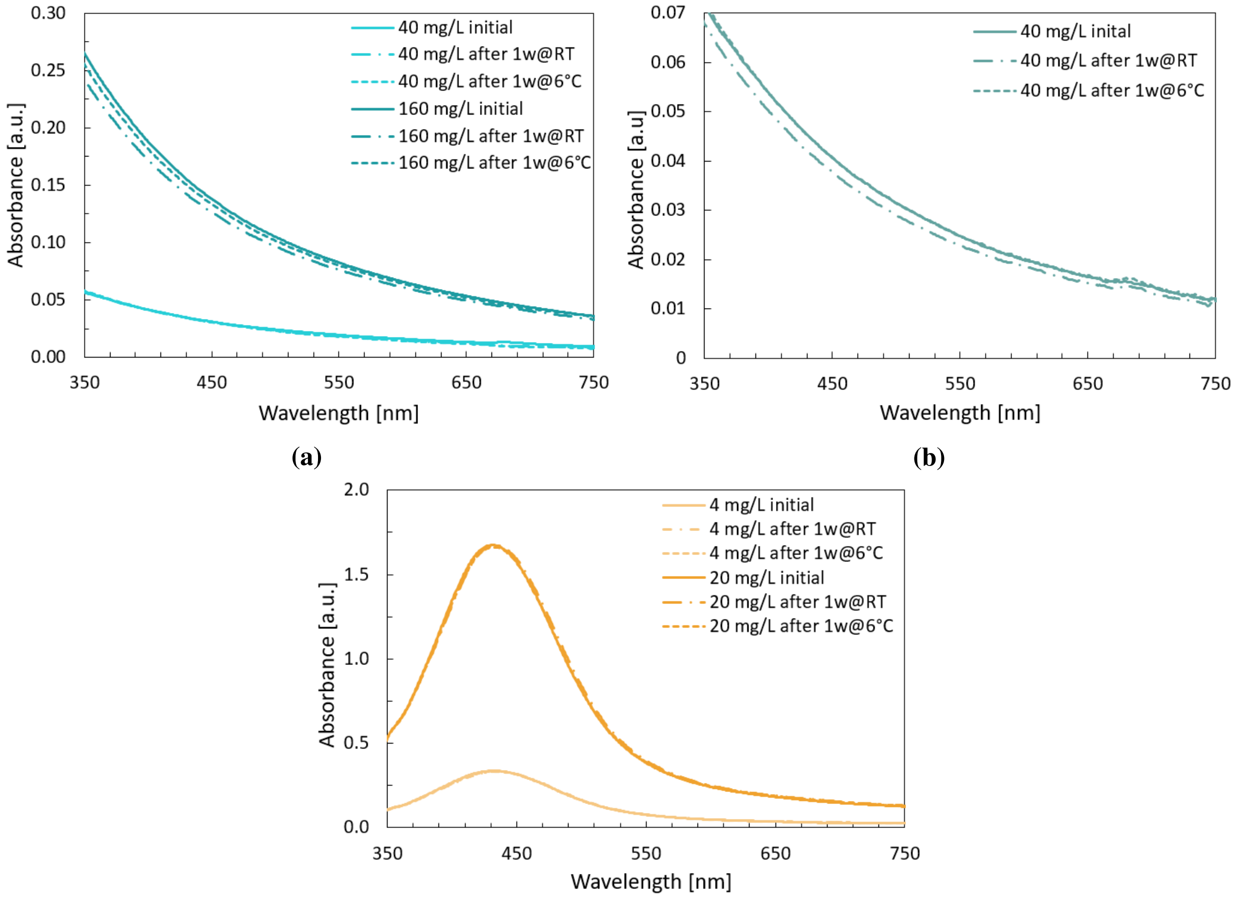

(a) **(b)**

(c)

Figure 4.20: Evolution of the absorbance spectra of the colloidal dispersion used in the algal growth experiments when stored at different temperatures. The spectra of (a) 40 mg/L and 160 mg/L SNP192, (b) 40 mg/L SNP256 and (c) 4 mg/L and 20 mg/L AgNP57 has been recorded after being stored in the dark at 6°C and RT for 1 week.

As small reduction in the absorbance spectra of the silica sols was observed after 1 week, and more so when stored at RT compared to 6°C (Figure 4.20 (a) and (b)). This might be due to settling, expected to occur for silica particles of these sizes when stored for some time [52]. However, the samples were shaken prior to the absorbance measurements to avoid contributions from this effect. The samples stored at 6°C did not experience much of a change in absorbance for any of the silica samples. For the AgNP57 colloid, no noticeable change was observed after 1 week at either of the temperatures.

4.7 Effect of NPs on the growth of *Rhodomonas baltica*

4.7.1 Pilot study with SNP95

In the pilot experiment applying 7217 mg/L of the SNP95 suspension, no replicates were used and the analytical measurements were not repeated. Therefore, no standard deviations are given for the plotted data points in Figure 4.21.

For both the algae surrounded by silica NPs and the control algae, the phycoerythrin fluorescence (Figure 4.21a) and chlorophyll *a* fluorescence (Figure 4.21c) increased up until day 5. This indicated microalgae growth or a higher pigment production per cell. The turbidity in both cultures also increased, indicating microalgal growth either in terms of larger cell sizes or a higher total number of cells, or both (Figure 4.21b). At day 7 the growth appeared to have subsided, based on the flattening of the turbidity curve. This is a result of the conditions inside the cultivation vessels becoming less optimal for microalgae production during the course of the experiment. The quantum yield, and hence the photosynthetic efficiency, of both cultures was also observed to decrease from 0.75 to 0.55 on day 5, correlated well with the declining algae growth. On day 7, ”overflow” was recorded during the QY measurement for both cultures. Hence, due to instrumental limitations, the QY on day 7 could not be recorded. The less optimal growth conditions towards the end of the growth experiment can also be seen from the observed reduction in pigment production per cell. This is evident from the simultaneous decline in PE and chl. *a* fluorescence and increase (or stagnation) in turbidity from day 5 to 7. On day 7, the mean cell concentration (when considering both the 7217SNP culture and the control) had increased from 160 to 1578 cells/µL (Figure 4.21d). That is, the cultures experienced an almost 10-fold increase in the number of cells in 1 week.

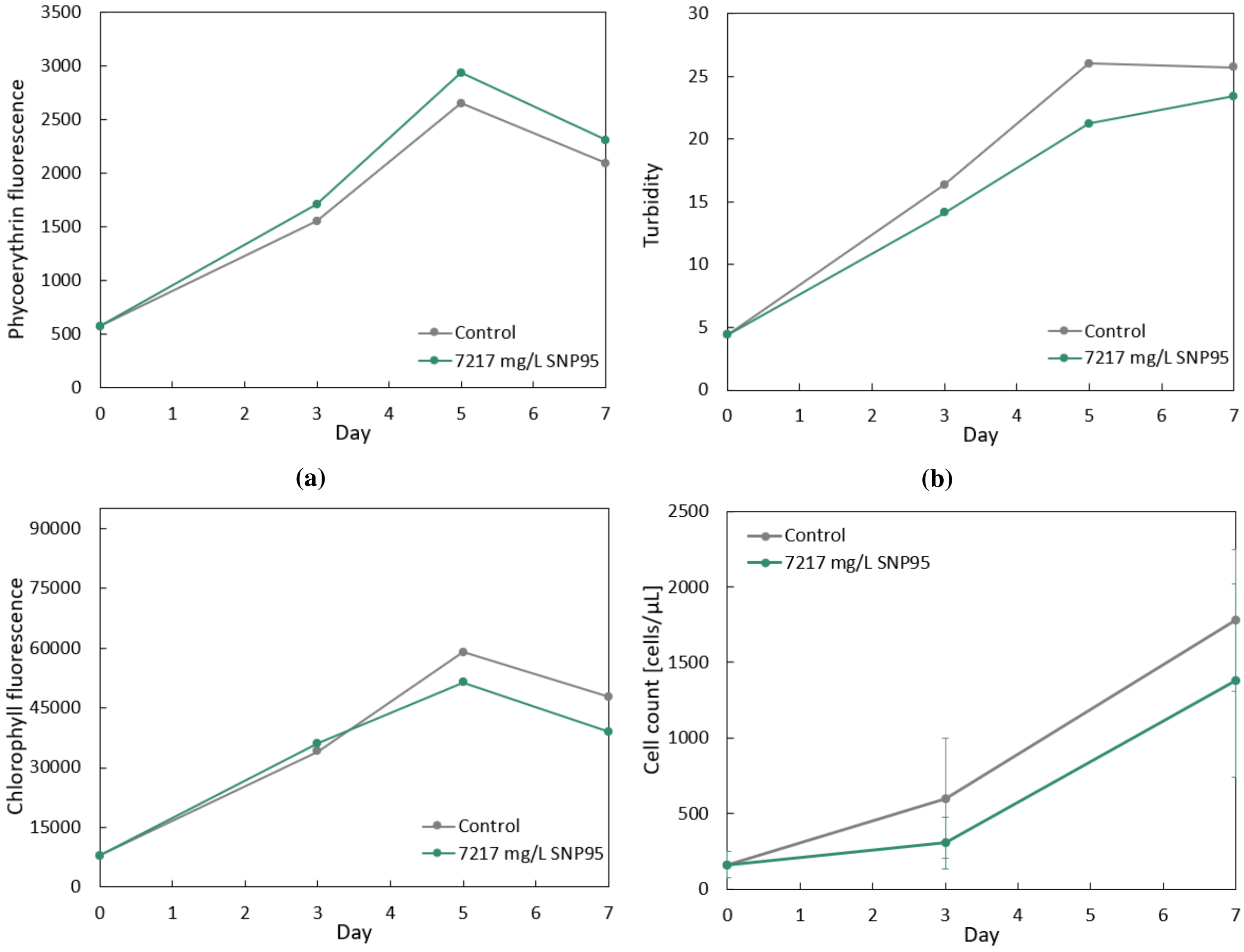

(a) (b)

(c) (d)

Figure 4.21: Measured values for (a) phycoerythrin fluorescence, (b) turbidity, (c) chlorophyll fluorescence and (d) cell count of *R. baltica* cultures in the pilot experiment with the SNP95 sol.

The microalgae hence seem to have grown healthily in the 5 first days of the experiment and to have reached the retardation phase, or even the stagnation phase, on day 7. This indicates that the experimental setup and growth conditions were suitable for cultivating *R. baltica*. The irradiance, temperature, aeration regime and nutrient profile used in the pilot were therefore deemed sufficient for algal growth and applied in the later experiments. Also, in the preparation of the start cultures for the rest of the growth experiments, efforts were made to ensure similar starting points in terms of their initial pigment content, turbidity and quantum yield. This was done by diluting the stock culture with growth medium if it was too dense. When it comes to the effect of the SNP95 particles on algal growth, however, no significant difference between the 7217SNP culture and the control was observed.

4.7.2 Growth experiment with SNP192 - the effect of silica NP concentration

During the first two days of cultivation, little change in PE and chl. *a* fluorescence as well as turbidity was observed, indicating microalgae growth was in the lag phase (Figure 4.22a, c and b, respectively). This was confirmed by the results obtained in the cell counting analysis, given in Figure 4.22d. On day 1, it was observed that the air flow into the cultivation vessels was less that the initially set flow rate. The air flow was therefore increased by manually adjusting the pressure valves for each cultivation vessels. On day 5, the bubbling of air had ceased completely. The inconsistent air supply is not likely to have caused carbon limitation of the algae, as this generally becomes an issue for much denser cultures. However, it did affect the mixing regimes, meaning that the environments in the cultivation vessels will vary slightly.

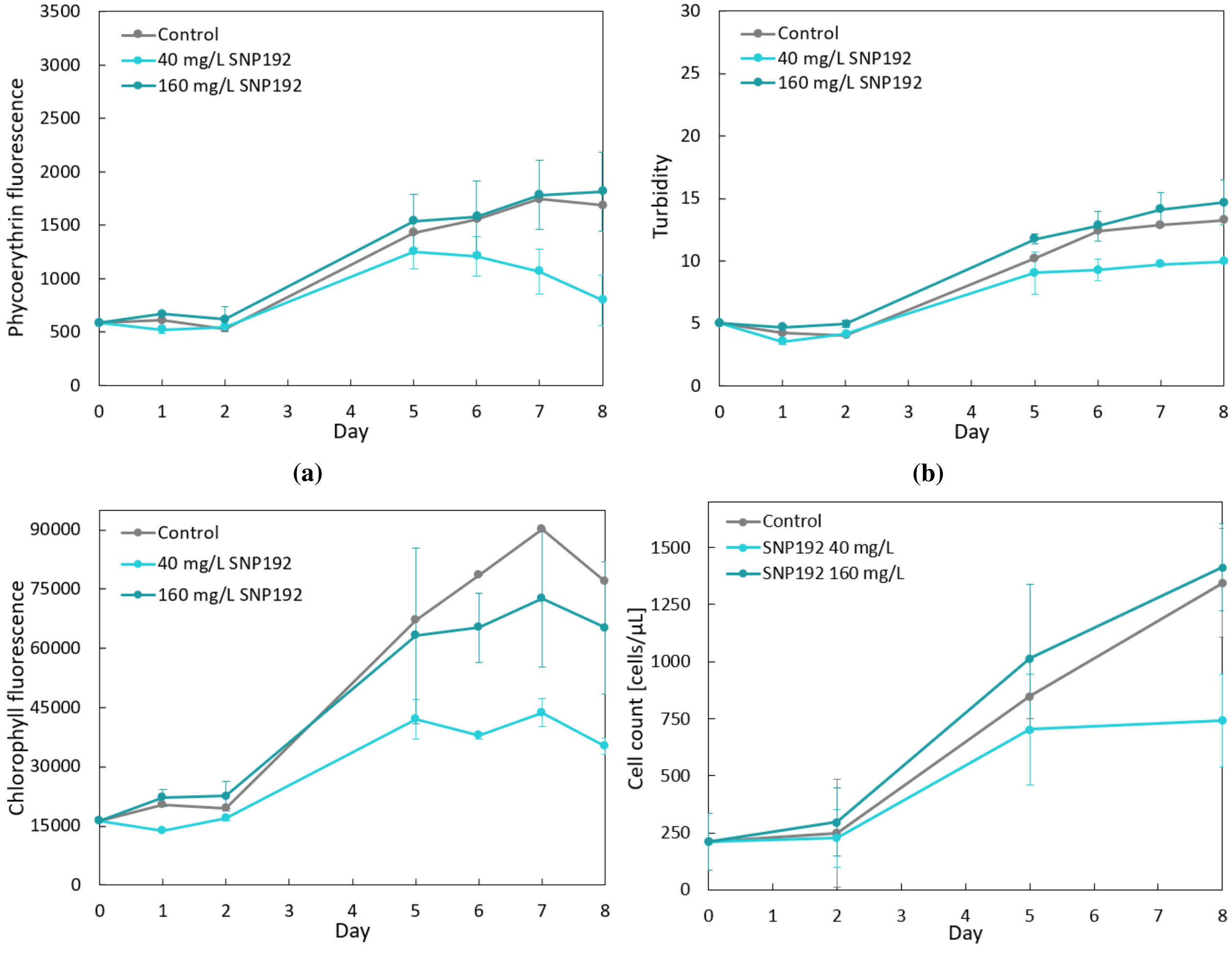

(a)

(b)

(c)

(d)

Figure 4.22: Measured (a) phycoerythrin fluorescence, (b) turbidity, (c) chlorophyll fluorescence and (d) cell count of algae cultures surrounded by 40 mg/L and 160 mg/L of the SNP192 sol. The plotted standard deviation bars represent the variation between replicate cultures.

Despite the varying air supply, algal growth was recorded on day 5 in all tubes. No significant difference was, however, observed between the 40SNP culture, the 160SNP culture and the control. From here on out, the 160SNP culture and the control culture continued to grow in similar fashion, as seen in Figure 4.22. However, in the 40SNP culture, the growth stopped at a lower cell concentration (Figure 4.22d). The minimal growth of the SNP40 culture was accompanied by a significant reduction in the PE content (Figure 4.22a), and the chl. *a* fluorescence and turbidity also stayed significantly lower for the 40SNP culture. In addition, the culture experienced a drop in quantum yield, as shown in Figure 4.23a. For the 160SNP culture and the control culture, QY values were not obtained after day 2 as the instrumental limit was reached. To provide a visual of the silica suspensions studied, a photo of the two SNP192 concentrations is also included (Figure 4.23b).

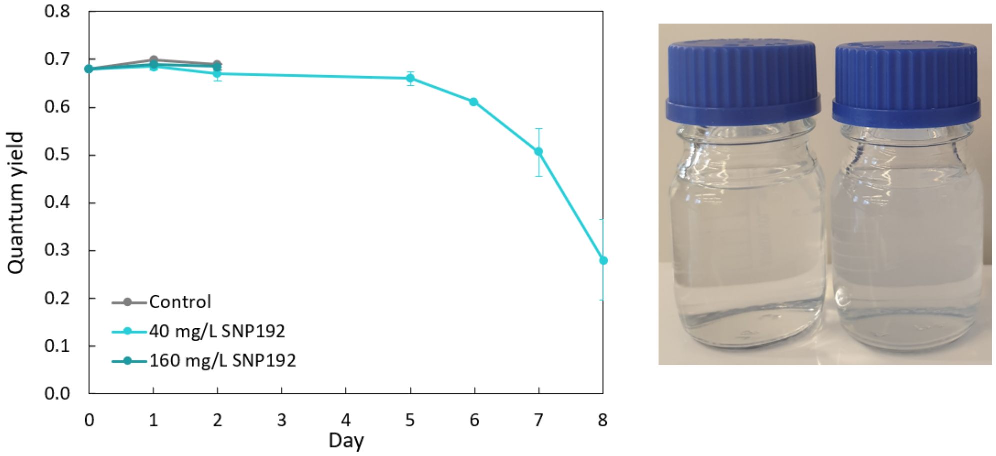

(a) **(b)**

Figure 4.23: (a) Measured quantum yield of the 40SN culture, the 160SNP culture and the control. The plotted standard deviations represent the variation between replicate cultures (b) Photo of the two different concentrations of the SNP192 sol used in the growth experiment. From left to right, 40 mg/L and 160 mg/L.

The reason for the poor photosynthetic efficiency and growth in the 40SNP culture is unknown. As the concentration of N and P was the same in all cultures, the reduced growth is not likely due to nutrition deficiency. Also, since the cultures surrounded by higher concentrations of the same particles did not experience this, any potential negative shading effects from the particles can be discounted. Whilst the 160SNP culture appeared to follow a healthy growth pattern, no significant differences in cell concentration compared to the control culture could be seen. Hence, the desired effect of enhanced biomass production was not demonstrated.

4.7.3 Growth experiment with AgNP57 - the effect of Ag NP concentration

As in the previous growth experiment, little change was observed for all of the measured parameters during the first two days of cultivation (Figure 4.24). During the first two days, the quantum yield in all cultures increased from 0.66 to 0.71, indicating that the algae were in good condition and that their photosynthetic efficiencies were increasing. The small detected change in the start of the experiment is therefore likely due to the algae being in their lag phase of growth, and not due to poor growth conditions. On day 4, increased turbidity as well as higher chlorophyll *a* and PE fluorescence yields were recorded, indicating algal growth. Generally, the control culture displayed the highest values for all of the photosynthetic parameters, closely followed by the 4AgNP culture. The cultures surrounded by the more concentrated colloid, the 20AgNP culture, consequently displayed the lowest values. Corresponding well with the turbidity measurements, the cell concentration was also found to be higher in the control culture whilst less and less growth was observed with increasing concentrations of the silver NPs up until day 4 (Figure 4.24d). On day 7, however, the same trend could no longer be observed. The slight pink cultures had become yellow in appearance, except for one of the 20AgNP cultures. The observed color change corresponds well with the drop in PE fluorescence (Figure 4.24a) and suggests that the algae had become nutrition limited. For one of the 20AgNP parallels, the red pigment continued to increase instead of dropping like the others, remaining pink in color. Due to the deviating behavior of one of the 20AgNP parallels, data for both of the replicas were plotted individually. The dotted lines in Figure 4.22 (a), (b), (c), and (d) represents the values obtained for the 20AgNP culture displaying the most deviating behavior compared to the rest of the cultures.

On day 7, crystallized salt was also found on the rubber stoppers on all cultivation vessels, indicating that the gas pressure had changed during the 3 day period, causing some of the culture to bubble over. With the setup used in this thesis, evaporation should be counteracted by humidifying the air before it is supplied to the cultures, and by using rubber stoppers with only small openings for venting and pressure regulation. However, when the pressure becomes too high, which appears to have been the case in this experiment, this can cause the cultures to bubble over. This may have affected the salinity of the remaining cultures in the vessels.

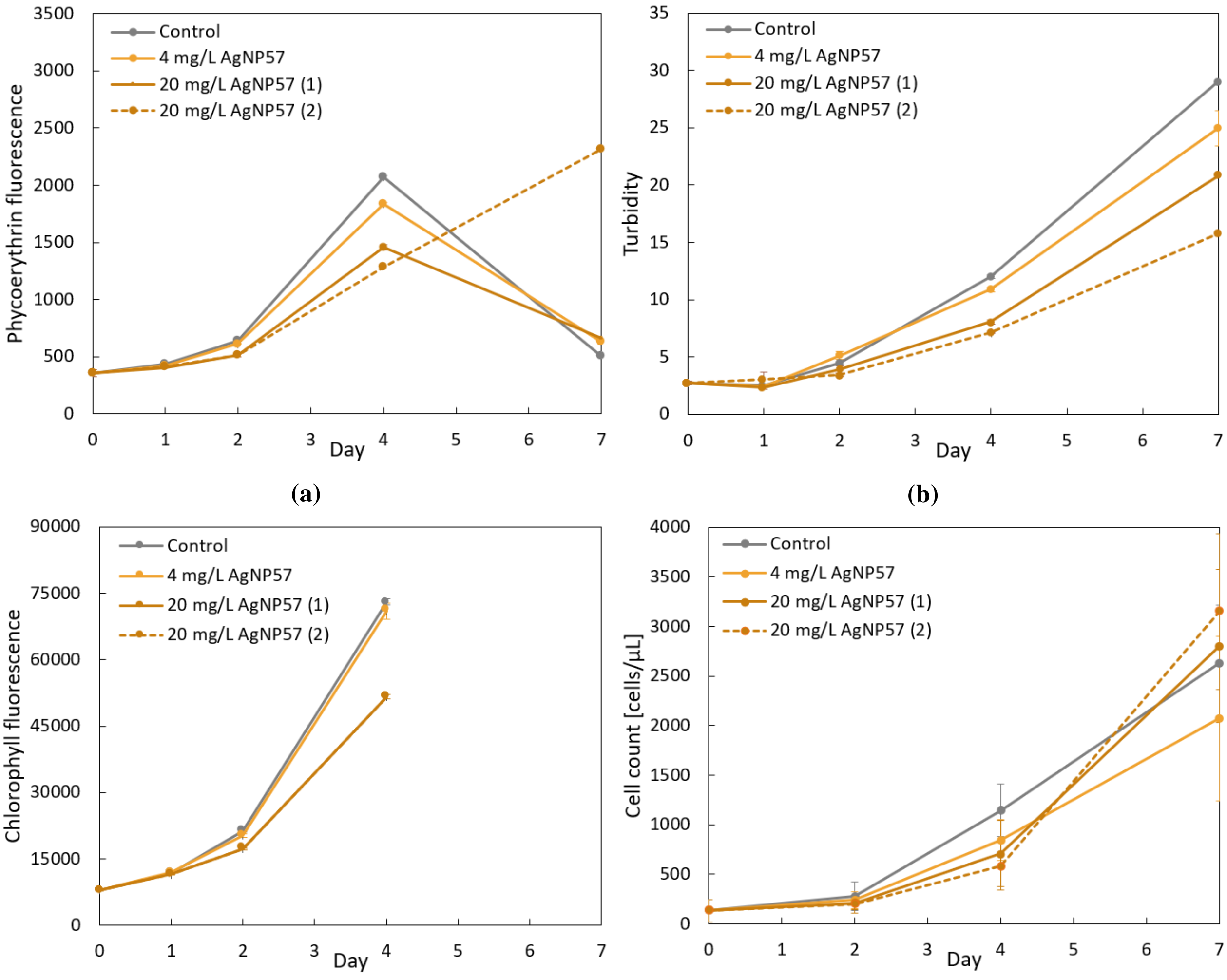

(a) (b)

(c) (d)

Figure 4.24: Measured (a) phycoerythrin fluorescence, (b) turbidity, (c) chlorophyll fluorescence and (d) cell count of algae cultures surrounded by 4 mg/L and 20 mg/L of the AgNP57 colloid. The error bars represents the standard deviation of repeated measurements. For 4 mg/L, the SD of replicate samples are also included.

As previously mentioned, a trend of lower pigment fluorescence and turbidity could be observed during the first 4 days of cultivation. This suggests that the conditions were less favourable for algal growth when surrounded by silver NPs. A reason for this might be the strong backscattering of the 20AgNP culture, causing too strong attenuation of the light before it enters the algal culture. As seen when imaging the silver colloids used in this experiment, the 20 mg/L AgNP57 suspension appears dark due limited transmission of light incident from the back (Figure 4.25).

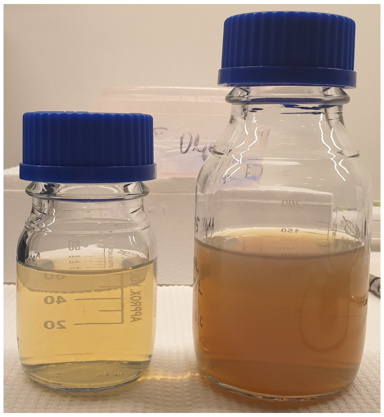

Figure 4.25: Photo of the two different concentrations of the AgNP57 suspension used in the growth experiment. From left to right, 4 mg/L and 20 mg/L.

4.7.4 Growth experiment with SNP256

In this last growth experiment, the potential light enhancing properties of the SNP256 particles were studied when diluted to a mass concentration of 40 mg/L. In contrast to the two previously discussed growth experiments, the obtained data did not show signs of a lag in growth during the first two days of cultivation. Instead, a noticeable increase in both the total pigment concentration and the turbidity of the cultures was observed already after the first day (Figure 4.26). The more rapid initial growth in this experiment could be the result of a more healthy start culture being used. In this experiment, the quantum yield of the initial *R. baltica* culture was 0.74, whereas in the studies using SNP192 and AgNP57, it was 0.68 and 0.66, respectively. This suggests that the start algae had a higher photosynthetic efficiency, making them able to grow and reproduce more rapidly. It should also be noted that the issue with inconsistent air supply was identified and fixed prior to this experiment, providing constant mixing and supply of CO_2 throughout the cultivation which also supports faster growth.

The growth continued for all cultures, and little significant difference in behavior was observed for 40SNP culture compared to the control culture. As seen by the plotted chl. *a* fluorescence in Figure 4.26 (c), the growth pattern appeared to correspond well with the general phases described by Monod [30], seemingly passing through the exponential growth phase before approaching the stagnation phase. After this, the chl. *a* fluorescence readings hit the instrumental limit, hence no more data points are provided. At day 7, the measured turbidity was seen to decrease for all cultures, but more so for the control algae than the 40SNP culture. This is likely a result of settling of the algal cells. As the growth starts to stagnate the algae tend to move less and can easily sink to the bottom, which may contribute to lower turbidity readings.

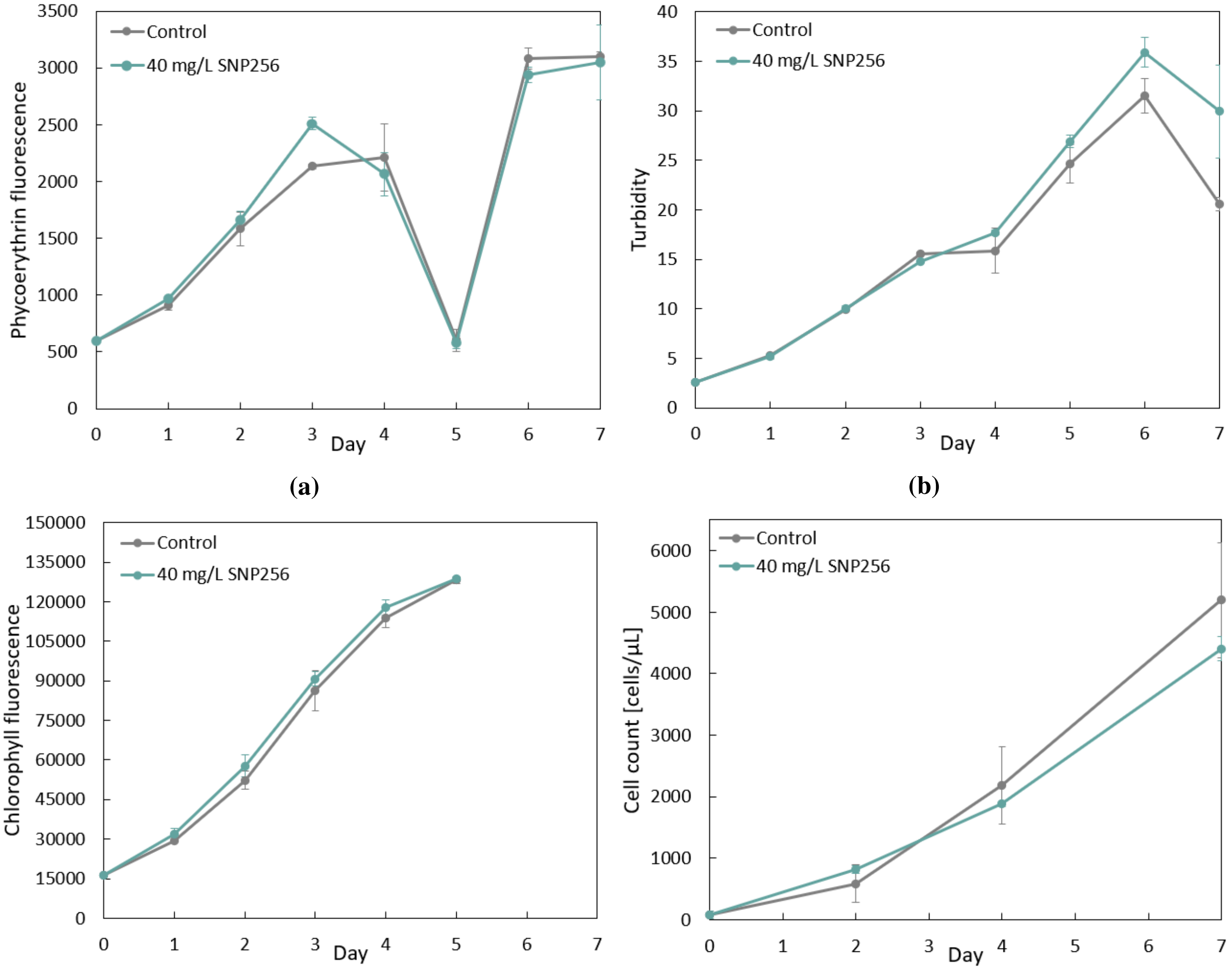

(a) **(b)**

(c) **(d)**

Figure 4.26: Measured (a) phycoerythrin fluorescence, (b) turbidity, (c) chlorophyll fluorescence and (d) cell count of algae cultures surrounded by 40 mg/L of the SNP256 sol. The error bars represents the combined standard deviation of the repeated measurements and replicate samples.

On day 4, a slight decrease in PE fluorescence in was recorded (Figure 4.26a), and the cultures had lost some of its pink color. The next day, the red pigment concentration had dropped dramatically, resulting in the cultures being green from chlorophyll. Suspecting that this was caused by limited nutrient availability, 100 µL of extra N and P was added to each of the cultivation vessels. As a result, the PE content went back up on day 6 and the cultures regained their red hue. This confirmed that the algae had become nutrient deficient. In Figure 4.27 the changing color of the *R. baltica* culture is shown. The photos were taken (a) on day 4, (b) on day 5 and (c) on day 6 after extra nutrients had been added.

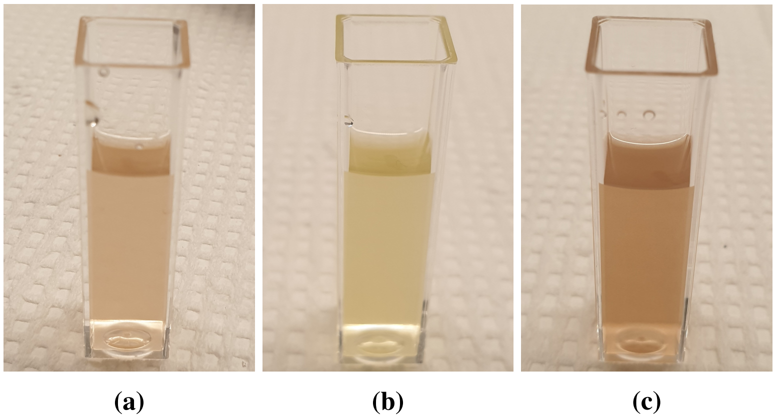
(a) (b) (c)

Figure 4.27: The change in color of *R. baltica* cultures when becoming nutrition limited. Photos are taken of the same algae culture (a) after detecting a slight decrease in PE content, (b) when nutrient deficient and (c) 1 day after adding 100 μL of extra N and P.

The nutrition deficiency in the algal cultures can have decreased the biomass productivity cell division rate of the algae, limiting the growth in this experiment [39]. Still, higher cell concentrations were recorded than in any other growth experiment (Figure 4.26d). In 7 days, the mean cell concentration of all cultures increased from 84 to 4802 cells/μL, almost a 60 fold increase. Again, this is likely due to good starting point of the initial culture and no issues with the air supply. No significant difference in the number of cells were, however, observed between the 40SNP culture and the control. Thus, no light enhancing effect was demonstrated even for larger silica particles.

5. Discussion

5.1 Nanoparticle synthesis

Amorphous, spherical silica nanoparticles have successfully been synthesized by the Stöber method. The NP size was easily tuned by adjusting the concentration of ammonia catalyst during synthesis, as predicted by literature [75]. Larger sizes as well as wider size distributions were obtained with higher ammonia concentrations. In the present work, silica sols with mean particle sizes of 95 ± 11, 192 ± 24 and 256 ± 40 nm were obtained.

Nanoparticles of metallic silver were successfully prepared by the reduction of silver nitrate by sodium citrate, following the classical Lee-Meisel citrate method. During the first 8 minutes of reaction, a rapid increase in the LSPR peak position was observed (Figure 4.10), resulting in the color evolution from light yellow to darker brown/gray. Based on the study of the nucleation and growth process of silver NPs in UV-VIS spectroscopy, a reaction time of 60 minutes was chosen for the application in this thesis. This corresponded with the reaction time originally proposed by Lee and Meisel [63]. The final silver colloid (AgNP57) was obtained with a mean particle size of 57 ± 14 nm, displaying localized surface plasmon resonance at 431 nm. Particles in this size region have also been reported by others [82]. Even though the same reaction time was applied, some variation in the LSPR peak position was observed for different batches. For the AgNP#4 sample boiled for 60 minutes and the AgNP57 colloid, the final λ_{max} values were 423 nm and 431 nm, respectively. Hence, there seems to be some difficulty in reproducing silver colloids by this method. This has also has been reported others, and according to Munro *et* al. [83], the absorbance spectra may vary greatly with λ_{max} ranging between 406-450 nm and an FWHM raging between 115 and 300 nm.

In terms of particle size and morphology, less uniform NPs were obtained in the preparation of silver particles compared to silica. The silver colloids contained mostly quasi-spherical particles, but other shapes such as cubes and rods were also present. Improved uniformity of the silver NPs could potentially be achieved by adopting a two-step synthesis or using a stronger reducing agent such as sodium borohydride [82, 110]. Better control of the silver particle morphology could also be obtained by adding a PVP capping agent during synthesis [66]. The variety of different shapes achieved in the present work presented some challenges related to the characterization of the silver particles. In both the particle size distribution analysis and the calculation of NP concentration based on gravimetry, perfectly spherical shapes are assumed. For the silver colloid, this is a rather large simplification, whereas for the silica sol the assumption is considered to be relatively accurate. Hence, for the AgNP57 colloid the mean particle size and the obtained NP concentration of 0.11 NPs/μm^3 may prove difficult to replicate.

5.2 Light scattering properties

The absorbance spectra recorded for SNP95, SNP192 and SNP256 were used as an indirect measure of scattering due to the non-absorbing nature of colloidal silica [101]. For all three silica sols a rise in extinction, or scattering, towards lower wavelengths was observed (Figure 4.3), as expected from Rayleigh theory [49]. The total scattering effect has been shown to increase with particle size (Figure 4.4) and NP concentration (Figure 4.3). For higher NP concentrations, the light attenuation in the forward direction becomes significant even for longer wavelengths (Figure 4.3). This suggests that a too high concentration may lead to poor illumination of the part of the PBR furthest away from the light source. There is, as demonstrated by Giannelli *et* al. [27], hence a trade-off between perpendicular scattering and the light penetration depth when choosing the NP concentration. When keeping the mass concentrations of the three sols the same (40 mg/L), higher intensities of the scattered light was observed for larger particle sizes (Figure 4.5). This demonstrated the size-dependent interaction of silica spheres with incoming light. The angular distribution of light scattered by silica NPs was also shown to be highly size-dependent. For the smallest particles of 95 nm the scattering pattern is more symmetric, whereas for larger particles light strongly scattered in the forward direction (Figure 4.15). When considering the size of silica NPs as scattering centers there is hence a trade-off between total scattering effect and the angular distribution of the scattered light. For an optimal light distribution inside microalgae cultures, the effect of total scattering versus angular distribution should, therefore, be investigated.

For the synthesized silver colloids, strong absorption and scattering of blue light was demonstrated. The recorded absorbance peak in the region of 400-450 nm is a result of the LSPR of silver NPs at these wavelengths. Whether the measured light attenuation was caused by absorption or backscattering was, however, not studied in this thesis. Calculations based on Mie theory performed by Santbergen *et* al. [61] does however indicate that the AgNP57 colloid mainly scatters incident light. They reported that the radiative efficiency of spherical silver NPs embedded in a medium with $\epsilon = 4$ was around 0.9-0.95 for diameters of 50-70 nm. That is, around 90-95% of the measured extinction of light was a result of backscattering rather than absorption. Although the particles in the AgNP57 colloid is dispersed in a different medium, the measured absorbance is likely to be mostly caused by scattering. The presence of less symmetrical particles affected the optical properties of the colloid, as demonstrated by the shoulder at 350 nm seen in the UV-VIS spectra (Figure 4.10, Figure 4.14).

Both the silica and silver particles displayed enhanced scattering of light in the blue region of the visible spectrum. This can potentially benefit microalgae biomass due to the wavelength-specific light absorption of algae. Generally, higher photosynthetic efficiencies are obtained with red and blue light rather than yellow and green light [35, 112]. The wavelength-selectivity of different microalgae strains is a widely studied topic. Spectral conversion from green to red has been reported by Wondraczek *et* al. [113] to enhance both the photosynthetic activity and reproduction rate of *Haematococcus pulicialis*. Another study by Mohsenpour *et* al. [114] demonstrated that whilst violet light was found to promote the growth of one type of algae, orange light gave the highest specific growth rate for another strain. For both strains, red light exhibited the least efficient conversion of light energy to biomass. In other studies, blue light has been found to increase the oil or lipid yield in certain microalgae, but can also inhibit cell growth and biomass production [115, 116, 117]. Enhancing light with wavelengths that are photosynthetically active is hence a promising strategy for improving the productivity of microalgae cultivation. As the silica NPs mainly scatter blue light, they may contribute to a more even supply of blue light throughout the culture. For microalgae with good absorption in the blue region, such *R. baltica* and other red algae, the use of silica or silver scatters seems especially promising. Stronger scattering and re-direction of energetic blue light by silica NPs might also be useful for limiting light supersaturation and photoinhibition.

5.3 Colloid stability

The effect of prolonged storage on the SNP95 sol stability was studied. After being stored in a dark environment at 6°C for 5 months, it appeared that some particle growth may have occurred and that the presence of aggregates had become more frequent. This suggests that the storage time affects the shape and size of silica NPs and thus also the scattering properties of the sol. However, only a slight reduction in absorbance intensity was recorded (Figure 4.17), indicating that the potential changes in particle size and morphology were not large enough to strongly alter the scattering properties of the sol. The temperature at which the silica sols were stored also seemed to have a slight effect on their scattering effect. When kept at either 6°C or room temperature for 1 week, a slight downwards shift in the UV-VIS spectra of the SNP192 and SNP256 sols were observed for the RT samples whilst the change in absorbance for the 6°C samples was negligible (Figure 4.20 (a) and (b)). This suggests that improved stability of the silica sols is achieved when stored at lower temperatures. During the microalgae growth experiments conducted at 20°C, the scattering properties of the silica NP suspensions may therefore have been altered slightly.

For the AgNP57 colloid, no noticeable change in absorbance was recorded after being stored for 1 week at either 6°C or at room temperature (Figure 4.20 (c)). During the growth experiment utilizing silver NPs the scattering properties are therefore not likely to have changed as a result of the higher temperature of 20°C. A factor that was found to greatly affect the stability of the silver colloids was the reaction time applied in the Lee-Meisel synthesis. Colloids prepared with a reaction times of 20 minutes or more appear to be stable for at least two weeks (Figure 4.10), and likely even longer. From literature, citrate reduced silver colloids are thought to be stable for around 6 months due to the electrostatic stabilization provided by citrate molecules [70]. When applying shorter reaction times, however, the absorbance intensity increased significantly during the 2 week period (Figure 4.11), indicating continued particle growth.

One factor that was not studied in this thesis is the effect of irradiance on the stability of the NP suspensions. As the main purpose of the nanoparticles ultimately is to use them in microalgae production systems to enhance or redistribute the incident radiation, this is a highly relevant aspect. From literature, silver is known to be highly photosensitive. Under controlled light irradiation, the shape and size of the particles can be altered, as documented for the conversion of silver nanospheres to triangular nanoprisms [118]. According to Grillet *et* al. [119], photoaging of silver NPs mainly involves the progressive formation of an oxide shell around the metallic core due to photo-assisted oxidation. For nanocubes, illumination also seems to cause rounding of the edges and corners. Photoaging can hence greatly affect the optical response of silver colloids, having been seen to cause dampening, broadening and a red-shift of the LSPR peak for silver spheres under illumination [119]. Another study by Shi *et* al. [120] found that light irradiation promoted particle growth due to silver ion release from smaller AgNPs and subsequent reduction and absorption onto larger particles. In addition, illumination was reported to cause agglomeration of the silver NPs by altering the surface potential and reducing the repulsion between individual particles. During the growth experiment with AgNP57, the irradiance supplied by LEDs may, therefore, have altered the morphology and thus the optical properties of the silver particles. In the study by Shi *et* al [120], a light intensity of 12,000 lux was used, which supplied enough energy to promote these changes. In the present study, white LEDs with a Photosynthetic Photon Flux Density (PPFD) of 100 μmol.m^{-2}.s^{-1} was used, corresponding to about 6,800 lux (when assuming a conversion factor from kilolux to PPDF of 14.6 [121]). The irradiance is hence almost half of that used by Shi *et* al. [120], still there is a possibility that the AgNPs may have changed during the growth experiment.

5.4 Measured effect of silica and silver NPs on *R. baltica* growth

In all four experiments, healthy growth of *R. baltica* was sustained, following typical stages of growth for batch cultures. After some time, nutrition availability became a limiting factor for denser cultures, demonstrated by a loss of the red PE pigment. No significant difference in the final concentration of *R. baltica* cells in the cultures surrounded by NPs and the controls were found in neither of the experiments. The desired effect of improved biomass production when applying silica or silver NP suspensions was therefore not demonstrated.

As previously discussed, both particle size and concentration greatly affect the scattering properties of silica and silver suspensions. The sizes of the silica NPs tested in this study are almost half the size of the NPs used by Giannelli *et* al [27], or smaller, and may have been insufficient to cause enough scattering to benefit the algae. For the smallest particles of 95 nm tested in the pilot experiment, the mass concentration was high (7217 mg/L) which may have led to poor light penetration. The more symmetric angular scattering distribution of SNP95 (Figure 4.15), with a considerable portion of backscattered light, suggests that shading of the algal cells might have counteracted any potential light redistributing effects.

For the growth experiment applying silver particles, a slight trend of lower pigment fluorescence and turbidity for higher AgNP57 concentrations could be seen (Figure 4.24 (a), (b) and (c)). This indicates slower growth in the cultures surrounded by silver NPs, possibly due to reduced light availability. Due to the plasmonic effect of the silver particles, incident light in the blue region will likely be backscattered before it even enters the culture. Despite the observed trend, no significant increase in cell concentration was found from the cell counting in Bürker chambers (Figure 4.24d). It should be mentioned that this analysis mainly is useful for providing information about the order of magnitude of the cell concentration and not a specific cell number due to the inherent uncertainty of this technique. For dense cultures, such as those obtained at the end of the AgNP57 growth experiment, counting the individual cells can be especially difficult, adding to the uncertainty of the presented data.

5.5 Photobioreactor setup

The Multi-Cultivator reactor setup with custom designed cultivation vessels allowed for easy monitoring of the algae as well as controllable conditions. By keeping the NP suspensions in the outer tube separated from the algae, toxic effects were avoided and recycling of the nanoparticles was possible. The ability to disassemble the inner and outer tubes allowed the glassware to easily be cleaned in between growth experiments. One drawback of this setup is however the lack of mixing provided in the nanoparticle compartment. For the SNP192 and SNP256 sols where settling might especially be an issue, this can significantly decrease the effect of the scattering particles as if using lower NP concentrations (Figure 4.3. In the presented work, efforts were made to minimize settling by manually re-dispersing any settled particles halfway through the SNP192 and SNP256 growth experiments. This was done by gently turning the cultivation vessels upside down a few times whilst covering the inner tube to avoid spillage of the cultures. For larger-scale applications, however, more sophisticated ways of providing mixing will likely be necessary, which would add to the production cost. Another drawback was the inconsistent air supply which proved to be an issue especially in the SNP192 and AgNP57 growth experiments. Using the MC setup, the individual valves controlling the airflow into each cultivation vessel was adjusted manually, making it challenging to provide identical flow rates and mixing regimes in all cultures. This can have made observing any potential effects of the NP suspensions even more difficult.

Even though no positive effect on biomass production was observed in this growth experiment, the AgNP57 colloid displayed strong backscattering properties which could have potential if implemented more suitably. A better way of implementing the silver NPs would be to place the particles on only the side of the cultivation vessels opposite to the light source. This could potentially be done by altering the vessels to include a vertical glass wall between the inner and outer tube, dividing the outer compartment in two. The NP suspension could then be added to the compartment facing away from the LEDs in the Multi-Cultivator. Such an approach would resemble the plasmonic mini-PBR used by Torkamani *et* al. [21] consisting of two petri dishes, one containing the algae culture and the other holding the Ag Np suspension, illuminated from above. This would however make it harder to disassemble the inner and outer tubes, a convenient feature of the cultivation vessels used in this thesis. Another way to implement silver nanoparticles could be to embed the NPs into a polymer film, as demonstrated by Estime *et* al [24] and place this in the compartment between the inner and outer tube. Alternatively, coating the spherical silver on either the outer wall of the inner tube or the inner wall of the outer tube could be considered. By implementing the silver NPs on only one side, the wavelength selective backscattering of silver NPs could be used to reduce transmission losses and improve the light utilization efficiency. By this method, however, no light distributing or diluting effect is provided before the light enters the culture. For high irradiance, problems related to supersaturation and photoinhibition therefore remains.

For the silica NPs with light mainly scattered in the forward direction, having them at the front and on the sides of the cultivation vessels appears to be beneficial. Their function is to redirect some of the incident light to improve the light transport inside the culture and protect the algae closest to the light source from supersaturation. By dividing the outer compartment of the cultivation vessels as mentioned, a potential approach could be to implement both the silica and silver suspensions on either side of the divider (Figure 5.1).

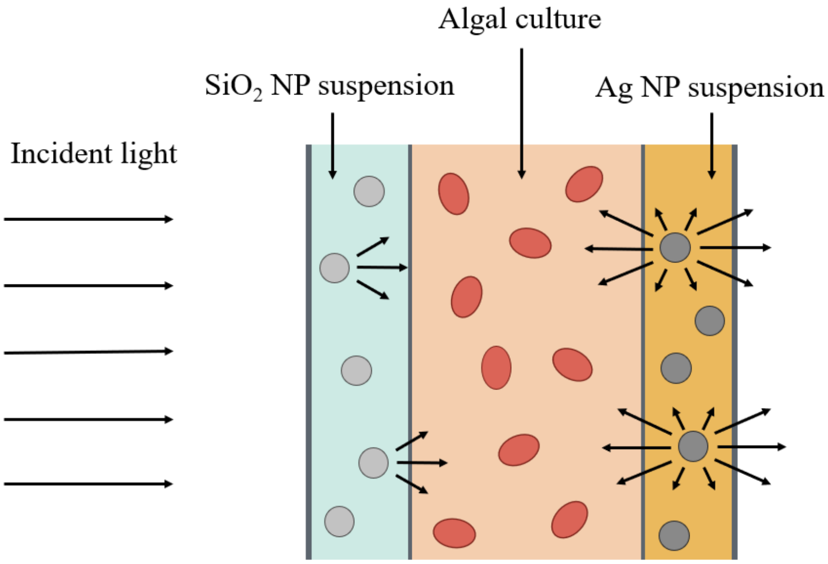

Figure 5.1: A potential approach where a silica NP suspension is implemented on side of the algal culture and a silver NP suspension on the other. Light is incident from the left and scattered by the NPs in the directions indicated.

The directions of light scattered by silica or silver NPs indicated by arrows are based on the angular scattering distribution of SNP256 and AgNP57, respectively (Figure 4.15). With this approach, the combined effect of a more homogeneous light distribution as well as amplification and backscattering of blue light can be achieved.

5.6 Other promising nanomaterials

In this thesis, only silica and silver NPs have been studied as potential light enhancing materials. Using silica as scattering material has multiple advantages. Firstly, spherical particles are easily synthesized by the Stöber method with good shape- and size-control. Silica is also affordable, which is an essential factor in making microalgae biomass production economically feasible. Additionally, it can be considered a green material that is found abundantly in nature, for example as hydrated silica ($SiO_2 \cdot 2H_2O$) in Diatom frustules [122]. Lastly, silica exhibits good material properties such as chemical and physical stability and compatibility with other materials [123]. One drawback, however, is that efficient scattering by silica nanospheres is limited to light of shorter wavelengths. Silver NPs, on the other hand, can be costly and difficult to prepare with precise size- and shape-control. But in return, their strong scattering properties makes them valuable for various applications. The strong shape- and size-dependency of the LSPR of Ag NPs also offers more control over the scattered wavelengths.

To combine the benefits of silica and silver, composite core-shell nanoparticles could be produced. With a silica core and silver shell, NPs with intense LSPR peaks can be obtained. The LSPR position can be tuned by varying the shell layer thickness, experiencing a red-shift for thinner shells [124]. It is therefore plausible that a mixture of NPs with different shell thicknesses can be used to facilitate scattering of light with various wavelengths. As microalgae generally have a high photosynthetic activity for blue and red light, enhancing light in both of these regions can be important for optimized biomass production [21]. Another way to achieve this is to use gold NPs with LSPR in the red region in combination with silver NPs. This was demonstrated by Eroglu *et* al. [22] who compared the backscattering effects of Ag NPs, Au nanorods, and a mixture of the two, and observed that the highest increase in biomass production was achieved when the light was dually scattered by the mixture. Gold NPs could also be used instead of silver, having the advantage of not showing significant long-term modifications of their optical response when subjected to illumination [119].

6. Conclusion

In this thesis, a new small-scale photobioreactor setup that allowed for the implementation of nanoparticles was developed by combining customized cultivation vessels with a Multi-Cultivator from PSI. By keeping the NP suspensions enclosed and separated from the culture medium, the NPs could be applied in a practical and environmentally safe way where concerns related to toxicity and waste disposal were circumvented. This also ensured good recyclability of the NP suspensions, enabling them to be used multiple times, thereby reducing long term material costs. When using this setup in growth experiments with the marine microalga *Rhodomonas baltica*, no enhancement of the cell concentration was found for cultures surrounded by either silica or silver NPs compared to the control cultures. The main objective of achieving higher biomass productivity due to improved light utilization when applying nanoparticles was therefore not reached. Investigation of the silica and silver NP suspension by spectrophotometry did, however, reveal optical properties that can be beneficial for microalgae biomass production. Spherical silica NPs have been demonstrated to increasingly scatter light towards lower wavelengths, giving higher scattering efficiencies for larger particles and higher NP concentrations. Quasi-spherical silver NPs have also been shown to display strong scattering of light in the blue region due to their localized surface plasmon resonance at these wavelengths. The LSPR curve of silver colloids was seen to change significantly throughout the NP formation reaction, demonstrating the effect of particle size and concentration on their scattering properties. The possibility to tailor the wavelength and intensity of the scattered light by tuning the geometrical features and concentration of silver NPs therefore has great potential that can be utilized in the optimization of microalgae biomass production.

7. Further work

Although some promising light scattering properties of silica and silver nanoparticles has been observed in this thesis, no positive effect on microalgal growth was recorded. To evaluate the potential of using such nanomaterials for this application, further tests should be run. Applying larger silica particles with higher scattering efficiencies might be needed to obtain large enough alterations of the light path for it to benefit the algae. Using different concentrations in future growth experiments could also be considered.

The focus of further work should also be aimed at optimizing the photobioreactor setup. Ways to alter the cultivation vessels used in this thesis to allow for a more suitable implementation of especially silver NPs should be considered. Keeping the plasmonic NPs on the back of the culture, on the opposite side of the light source, is likely to be more beneficial for microalgae growth. One suggested way to do this is to add a vertical divider in between the inner and outer tubes to provide two separate compartments surrounding the algae. Embedding nanoparticles into polymer films may also be a viable alternative that should be considered. If kept in separate compartments, applying both silica silver NPs on opposite sides of the algal culture represents an interesting approach that could be tested. The cultivation system could also be improved by providing mixing to the nanoparticle suspensions in order to avoid settling.

Lastly, further work should also aim to study other nanomaterials that display promising light enhancing properties. Scattering by silica-silver core-shell particles should be investigated and compared to that of pure Ag NPs. Based on this, the benefits related to the cost and convenience of using a silica core can be discussed. Using mixtures of different nanomaterials such as silver and gold NPs to facilitate backscattering of both blue and red light should also be investigated. Through growth experiments with suitable microalgae strains, the effect of different nanomaterials on biomass production can be evaluated and compared.

Bibliography

[1] M. I. Khan, J. H. Shin, and J. D. Kim. The promising future of microalgae: current status, challenges, and optimization of a sustainable and renewable industry for biofuels, feed, and other products. *Microbial cell factories*, 17(1):36, 2018.

[2] F. B. Metting. Biodiversity and application of microalgae. *Journal of Industrial Microbiology*, 17(5):477–489, November 1996.

[3] J. Benemann. Microalgae for Biofuels and Animal Feeds. *Energies*, 6(11):5869–5886, November 2013.

[4] S. S. Oncel. Microalgae for a macroenergy world. *Renewable and Sustainable Energy Reviews*, 26:241–264, October 2013.

[5] N. Mallick. Biotechnological potential of immobilized algae for wastewater N, P and metal removal: A review. *Biometals*, 15(4):377–390, December 2002.

[6] Y. Chisti. Biodiesel from microalgae. *Biotechnology Advances*, 25(3):294–306, May 2007.

[7] L. Moreno-Garcia, K. Adjallé, S. Barnabé, and G. S. V. Raghavan. Microalgae biomass production for a biorefinery system: Recent advances and the way towards sustainability. *Renewable and Sustainable Energy Reviews*, 76:493–506, September 2017.

[8] Y. Chisti. An unusual hydrocarbon. *Journal of the Ramsay Society*, 27-28:24–26, 1980.

[9] Millennium Ecosystem Assessment (Program), editor. *Ecosystems and human well-being: synthesis*. Island Press, Washington, DC, 2005. OCLC: ocm59279709.

[10] J. Singh and S. Gu. Commercialization potential of microalgae for biofuels production. *Renewable and Sustainable Energy Reviews*, 14(9):2596–2610, 2010. Publisher: Elsevier Ltd.

[11] Y. Sun, Q. Liao, Y. Huang, A. Xia, Q. Fu, X. Zhu, and Y. Zheng. Integrating planar waveguides doped with light scattering nanoparticles into a flat-plate photobioreactor to improve light distribution and microalgae growth. *Bioresource Technology*, 220:215–224, November 2016.

[12] F. C. Rubio, F. G. Camacho, J. M. F. Sevilla, Y. Chisti, and E. M. Grima. A mechanistic model of photosynthesis in microalgae. *Biotechnology and Bioengineering*, 81(4):459–473, 2003. Place: New York Publisher: Wiley Subscription Services, Inc, A Wiley Company.

[13] H. M. Amaro, A. C. Guedes, and F. X. Malcata. Advances and perspectives in using microalgae to produce biodiesel. *Applied Energy*, 88(10):3402–3410, October 2011.

[14] M. S. Chauton, K. I. Reitan, N. H. Norsker, R. Tveterås, and H. T. Kleivdal. A techno-economic analysis of industrial production of marine microalgae as a source of EPA and DHA-rich raw material for aquafeed: Research challenges and possibilities. *Aquaculture*, 436:95–103, 2015.

[15] Ling Xu, P. J. Weathers, X.-R. Xiong, and C.-Z. Liu. Microalgal bioreactors: Challenges and opportunities. *Engineering in Life Sciences*, 9(3):178–189, 2009.

[16] Q. Liao, L. Li, R. Chen, and X. Zhu. A novel photobioreactor generating the light/dark cycle to improve microalgae cultivation. *Bioresource Technology*, 161:186–191, 2014.

[17] J. E. W. Polle, S.-D. Kanakagiri, and A. Melis. tla1, a DNA insertional transformant of the green alga Chlamydomonas reinhardtii with a truncated light-harvesting chlorophyll antenna size. *Planta*, 217(1):49–59, 2003. Num Pages: 11.

[18] L. Wondraczek, A. Gründler, A. Reupert, K. Wondraczek, M. A. Schmidt, G. Pohnert, and S. Nolte. Biomimetic light dilution using side-emitting optical fiber for enhancing the productivity of microalgae reactors. *Scientific Reports (Nature Publisher Group); London*, 9:1–10, July 2019.

[19] Y.-C. Lee, K. Lee, and Y.-K. Oh. Recent nanoparticle engineering advances in microalgal cultivation and harvesting processes of biodiesel production: A review. *Bioresource Technology*, 184:63–72, 2015.

[20] J. Romann, J.-C. Valmalette, M. S. Chauton, G. Tranell, M.-A. Einarsrud, and O. Vadstein. Wavelength and orientation dependent capture of light by diatom frustule nanostructures. *Scientific Reports*, 2015.

[21] S. Torkamani, S. N. Wani, Y. J. Tang, and R. Sureshkumar. Plasmon-enhanced microalgal growth in miniphotobioreactors. *Applied Physics Letters*, 97(4), 2010.

[22] E. Eroglu, P. Eggers, M. Winslade, S. Smith, and C. Raston. Enhanced accumulation of microalgal pigments using metal nanoparticle solutions as light filtering devices. *Green Chemistry*, 15:3155–3159, October 2013.

[23] M. D. Ooms, Y. Jeyaram, and D. Sinton. Wavelength-selective plasmonics for enhanced cultivation of microalgae. *Applied Physics Letters*, 106(6):063902, February 2015.

[24] B. Estime, D. Ren, and R. Sureshkumar. Effects of plasmonic film filters on microalgal growth and biomass composition. *Algal Research*, 11:85–89, 2015.

[25] P. Matheu, S. H. Lim, D. Derkacs, C. Mcpheeters, and E. T. Yu. Metal and dielectric nanoparticle scattering for improved optical absorption in photovoltaic devices. *Applied Physics Letters*, 93(11), 2008.

[26] J. Lee, Y. Y. Kwon, E.-H. Choi, J. Park, H. Yoon, and H. Kim. Enhancement of light-extraction efficiency of organic light-emitting diodes using silica nanoparticles embedded in TiO matrices. *Optics express*, 22(S3):A705–A714, 2014.

[27] L. Giannelli and G. Torzillo. Hydrogen production with the microalga Chlamydomonas reinhardtii grown in a compact tubular photobioreactor immersed in a scattering light nanoparticle suspension. *International Journal of Hydrogen Energy*, 37(22):16951–16961, 2012.

[28] S. Tebbani, F. Lopes, R. Filali, D. Dumur, and D. Pareau. Microalgae. In *CO Biofixation by Microalgae*, pages 1–22. John Wiley & Sons, Inc, 2014.

[29] N. Bourne, C. A. Hodgson, and J. N. C. Whyte. Manual for Scallop Culture in British Columbia. page 232, 1989.

[30] J. Monod. The Growth of Bacterial Cultures. *Annual Review of Microbiology*, 3(1):371–394, 1949. _eprint: https://doi.org/10.1146/annurev.mi.03.100149.002103.

[31] K. Maxwell and G. Johnson. Chlorophyll fluorescence - a practical guide. *Journal Of Experimental Botany*, 51(345):659–668, 2000. Publisher: OXFORD UNIV PRESS.

[32] D. Iluz and Z. Dubinsky. Quantum Yields in Aquatic Photosynthesis. *Photosynthesis*, June 2013. Publisher: IntechOpen.

[33] B. Genty, J.-M. Briantais, and N. R. Baker. The relationship between the quantum yield of photosynthetic electron transport and quenching of chlorophyll fluorescence. *Biochimica et Biophysica Acta (BBA) - General Subjects*, 990(1):87–92, January 1989.

[34] J. Masojídek, G. Torzillo, and M. Koblížek. Photosynthesis in Microalgae. In *Handbook of microalgal culture:applied phycology and biotechnology*, pages 20–39. Wiley Blackwell, 2 edition, 2013.

[35] A. M. Lehmuskero, M. S. Chauton, and T. Boström. Light and photosynthetic microalgae: A review of cellular- and molecular-scale optical processes. *Progress in Oceanography*, 2018.

[36] A. H. Arias, A. Souissi, O. Glippa, M. Roussin, D. Dumoulin, S. Net, B. Ouddane, and S. Souissi. Removal and Biodegradation of Phenanthrene, Fluoranthene and Pyrene by the Marine Algae Rhodomonas baltica Enriched from North Atlantic Coasts. *Bulletin of Environmental Contamination and Toxicology*, 98(3):392–399, March 2017.

[37] P. C. Southgate and J. S. Lucas. *Aquaculture: farming aquatic animals and plants*. Wiley-Blackwell, Chichester, 2nd ed. edition, 2012. Pages: XVI, 629.

[38] X. Wang, H. K. Fosse, K. Li, M. S. Chauton, O. Vadstein, and K. I. Reitan. Influence of Nitrogen Limitation on Lipid Accumulation and EPA and DHA Content in Four Marine Microalgae for Possible Use in Aquafeed. *Frontiers in Marine Science*, 6, 2019. Publisher: Frontiers.

[39] G. Breuer, P. P. Lamers, D. E. Martens, R. B. Draaisma, and R. H. Wijffels. The impact of nitrogen starvation on the dynamics of triacylglycerol accumulation in nine microalgae strains. *Bioresource Technology*, 124:217–226, November 2012.

[40] A.J. Lewitus and D.A. Caron. Relative effects of nitrogen or phosphorus depletion and light intensity on the pigmentation, chemical composition, and volume of Pyrenomonas salina (Cryptophyceae). *Mar. Ecol. Prog. Ser.*, 61:171–181, 1990.

[41] A. F. da Silva, S. O. Lourenço, and R. M. Chaloub. Effects of nitrogen starvation on the photosynthetic physiology of a tropical marine microalga Rhodomonas sp. (Cryptophyceae). *Aquatic Botany*, 91(4):291–297, November 2009.

[42] M. Prussi, M. Buffi, D. Casini, D. Chiaramonti, F. Martelli, M. Carnevale, M. R. Tredici, and L. Rodolfi. Experimental and numerical investigations of mixing in raceway ponds for algae cultivation. *Biomass and Bioenergy*, 67:390–400, 2014.

[43] J. N. Rogers, J. N. Rosenberg, B. J. Guzman, V. H. Oh, L. E. Mimbela, A. Ghassemi, M. J. Betenbaugh, G. A. Oyler, and M. D. Donohue. A critical analysis of paddlewheel-driven raceway ponds for algal biofuel production at commercial scales. *Algal Research*, 4(1):76–88, 2014.

[44] Y.-K. Lee and C.-S. Low. Effect of photobioreactor inclination on the biomass productivity of an outdoor algal culture. *Biotechnology and Bioengineering*, 38(9):995–1000, 1991. _eprint: https://onlinelibrary.wiley.com/doi/pdf/10.1002/bit.260380906.

[45] Q. Huang, F. Jiang, L. Wang, and C. Yang. Design of Photobioreactors for Mass Cultivation of Photosynthetic Organisms. *Engineering*, 3(3):318–329, June 2017.

[46] E. Molina, J. Fernández, F. G. Acién, and Y. Chisti. Tubular photobioreactor design for algal cultures. *Journal of Biotechnology*, 92(2):113–131, December 2001.

[47] F. G. A. Fernández, F. G. Camacho, J. A. S. Pérez, J. M. F. Sevilla, and E. M. Grima. A model for light distribution and average solar irradiance inside outdoor tubular photobioreactors for the microalgal mass culture. *Biotechnology and Bioengineering*, 55(5):701–714, 1997. _eprint: https://onlinelibrary.wiley.com/doi/pdf/10.1002/%28SICI%291097-0290%2819970905%2955%3A5%3C701%3A%3AAID-BIT1%3E3.0.CO%3B2-F.

[48] M. V. Tjønneland. Optimizing Microalgae Biomass Production; Using Nanomaterials for Enhanced Light Transport. Project report in TMT4500, Department of Materials Science and Engineering, NTNU - Norwegian University of Science and Technology, December 2019.

[49] E. Hecht. *Optics: Pearson New International Edition*. Pearson Education UK, 2013.

[50] M. Kerker. *The scattering of light and other electromagnetic radiation*, volume 16 of *Physical chemistry*. Academic Press, New York, 1969.

[51] C. F. Bohren and D. R. Huffman. *Absorption and Scattering of Light by Small Particles*. Wiley-VCH Verlag GmbH, Weinheim, Germany, 2007.

[52] R. K. Iler. *Chemistry of Silica - Solubility, Polymerization, Colloidal and Surface Properties and Biochemisty*. John Wiley & Sons, 1979.

[53] R. J. de Kok and D. M. Stam. The influence of forward-scattered light in transmission measurements of (exo)planetary atmospheres. *Icarus*, 221(2):517–524, 2012.

[54] W. Hergert and T. Wriedt. *The Mie Theory: Basics and Applications*, volume 169 of *Springer series in optical sciences ;*. Springer Berlin Heidelberg : Imprint: Springer, Berlin, Heidelberg, 1st ed. 2012. edition, 2012.

[55] G. Mie. Beiträge zur Optik trüber Medien, speziell kolloidaler Metallösungen. *Annalen der Physik*, 330(3):377–445, 1908.

[56] A. Usami. Theoretical simulations of optical confinement in dye-sensitized nanocrystalline solar cells. *Solar Energy Materials and Solar Cells*, 64(1):73–83, September 2000.

[57] L. Tonks and I. Langmuir. Oscillations in Ionized Gases. *Physical Review*, 33(2):195–210, February 1929.

[58] C. F. Bohren. How can a particle absorb more than the light incident on it? *American Journal of Physics*, 51(4):323–327, April 1983.

[59] K. A. Willets and R. P. Van Duyne. Localized Surface Plasmon Resonance Spectroscopy and Sensing. *Annual Review of Physical Chemistry*, 58(1):267–297, 2007.

[60] S. Pillai, K. R. Catchpole, T. Trupke, and M. A. Green. Surface plasmon enhanced silicon solar cells. *Journal of Applied Physics*, 101(9), 2007.

[61] R. Santbergen, T. L. Temple, R. Liang, A. H. M. Smets, R. A. C. M. M. van Swaaij, and M. Zeman. Application of plasmonic silver island films in thin-film silicon solar cells. *Journal of Optics*, 14(2):024010, January 2012. Publisher: IOP Publishing.

[62] S. Link and M. A. El-Sayed. Shape and size dependence of radiative, non-radiative and photothermal properties of gold nanocrystals. *International Reviews in Physical Chemistry*, 19(3):409–453, July 2000.

[63] P. C. Lee and D. Meisel. Adsorption and surface-enhanced Raman of dyes on silver and gold sols. *Journal of Physical Chemistry*, 86(17):3391–3395, 1982.

[64] S. Link and M. A. El-Sayed. Spectral Properties and Relaxation Dynamics of Surface Plasmon Electronic Oscillations in Gold and Silver Nanodots and Nanorods. *The Journal of Physical Chemistry B*, 103(40):8410–8426, October 1999.

[65] A. Šileikaitė, J. Puiso, I. Prosycevas, and S. Tamulevičius. Investigation of Silver Nanoparticles Formation Kinetics During Reduction of Silver Nitrate with Sodium Citrate. *Medziagotyra*, 15, January 2009.

[66] B. Wiley, Y. Sun, B. Mayers, and Y. Xia. Shape-Controlled Synthesis of Metal Nanostructures: The Case of Silver. *Chemistry – A European Journal*, 11(2):454–463, 2005.

[67] Kl Kelly, E. Coronado, Ll Zhao, and Gc Schatz. The optical properties of metal nanoparticles: The influence of size, shape, and dielectric environment. *Journal Of Physical Chemistry B*, 107(3):668–677, 2003.

[68] H. E. Bergna and W. O. Roberts. *Colloidal silica: fundamentals and applications*, volume v. 131 of *Surfactant science series ;*. CRC Taylor & Francis, Boca Raton, FL, 2006.

[69] G. Cao and Y. Wang. *Nanostructures and Nanomaterials: Synthesis, Properties and Applications*, volume 2. World Scientific Publishing Co. Pte. Ltd., 2011.

[70] C. S. S. R. Kumar. *Raman Spectroscopy for Nanomaterials Characterization*. Springer Science & Business Media, March 2012.

[71] C. J. Brinker. *Sol-gel science: the physics and chemistry of sol-gel processing*. Academic Press, Boston, 1990.

[72] D. W. Schaefer. Polymers, Fractals, and Ceramic Materials. *Science*, 243(4894):1023–1027, February 1989.

[73] Aqueous and Nonaqueous Sol-Gel Chemistry. In M. Niederberger and N. Pinna, editors, *Metal Oxide Nanoparticles in Organic Solvents: Synthesis, Formation, Assembly and Application*, Engineering Materials and Processes, pages 7–18. Springer London, London, 2009.

[74] C. J. Brinker. Hydrolysis and condensation of silicates: Effects on structure. *Journal of Non-Crystalline Solids*, 100(1-3):31–50, March 1988.

[75] W. Stöber, A. Fink, and E. Bohn. Controlled growth of monodisperse silica spheres in the micron size range. *Journal of Colloid And Interface Science*, 26(1):62–69, 1968.

[76] Q. Guo, D. Huang, X. Kou, W. Cao, L. Li, L. Ge, and J. Li. Synthesis of disperse amorphous SiO2 nanoparticles via sol–gel process. *Ceramics International*, 43(1, Part A):192–196, January 2017.

[77] T. Matsoukas and E. Gulari. Dynamics of growth of silica particles from ammonia-catalyzed hydrolysis of tetra-ethyl-orthosilicate. *Journal of Colloid and Interface Science*, 124(1):252–261, July 1988.

[78] H.-C. Wang, C.-Y. Wu, C.-C. Chung, M.-H. Lai, and T.-W. Chung. Analysis of parameters and interaction between parameters in preparation of uniform silicon dioxide nanoparticles using response surface methodology. *Industrial & Engineering Chemistry Research*, 45(24):8043–8048, 2006.

[79] D. Qi, C. Lin, H. Zhao, H. Liu, and T. Lü. Size regulation and prediction of the SiO2 nanoparticles prepared via Stöber process. *Journal of Dispersion Science and Technology*, 38(1):70–74, 2017.

[80] M. U. Rashid, M. K. H. Bhuiyan, and M. E. Quayum. Synthesis of silver nano particles (Ag-NPs) and their uses for quantitative analysis of vitamin C tablets. *Dhaka University Journal of Pharmaceutical Sciences*, 12(1):29–33, 2013.

[81] Dan V. Goia and E. Matijević. Preparation of monodispersed metal particles. *New Journal of Chemistry*, 22(11):1203–1215, January 1998.

[82] S. Rinaldi and L. Latterini. Development of versatile synthetic procedures to prepare colloidal silver nanoparticles with defined properties. In *Silver Nanoparticles: Synthesis, Uses and Health Concerns*. Nova Science Publishers, Inc., 2013.

[83] C. H. Munro, W. E. Smith, M. Garner, J. Clarkson, and P. C. White. Characterization of the Surface of a Citrate-Reduced Colloid Optimized for Use as a Substrate for Surface-Enhanced Resonance Raman Scattering. *Langmuir*, 11(10):3712–3720, October 1995.

[84] Y. Wan, Z. Guo, X. Jiang, K. Fang, X. Lu, Y. Zhang, and N. Gu. Quasi-spherical silver nanoparticles: Aqueous synthesis and size control by the seed-mediated Lee–Meisel method. *Journal of Colloid and Interface Science*, 394:263–268, March 2013.

[85] G. Oberdorster, E. Oberdorster, and J. Oberdorster. Nanotoxicology: An emerging discipline evolving from studies of ultrafine particles. *Environmental Health Perspectives*, 113(7):823–839, 2005.

[86] K.-H. Cho, J.-E. Park, T. Osaka, and S.-G. Park. The study of antimicrobial activity and preservative effects of nanosilver ingredient. *Electrochimica Acta*, 51(5):956–960, November 2005.

[87] A. L. Incoronato, A. Conte, G. G. Buonocore, and M. A. Del Nobile. Agar hydrogel with silver nanoparticles to prolong the shelf life of Fior di Latte cheese. *Journal of Dairy Science*, 94(4):1697–1704, April 2011.

[88] D. K. Tiwari, J. Behari, and P. Sen. Application of Nanoparticles in Waste Water Treatment. page 17, 2008.

[89] L. J. Hazeem, G. Kuku, E. Dewailly, C. Slomianny, A. Barras, A. Hamdi, R. Boukherroub, M. Culha, and M. Bououdina. Toxicity Effect of Silver Nanoparticles on Photosynthetic Pigment Content, Growth, ROS Production and Ultrastructural Changes of Microalgae Chlorella vulgaris. *Nanomaterials (Basel, Switzerland)*, 9(7):914–, 2019. Place: Switzerland Publisher: MDPI AG.

[90] S. Manzo, S. Buono, G. Rametta, M. Miglietta, S. Schiavo, and G. Francia. The diverse toxic effect of SiO 2 and TiO 2 nanoparticles toward the marine microalgae Dunaliella tertiolecta. *Environmental Science and Pollution Research*, 22(20):15941–15951, 2015.

[91] K. Fujiwara, H. Suematsu, E. Kiyomiya, M. Aoki, M. Sato, and N. Moritoki. Size-dependent toxicity of silica nano-particles to Chlorella kessleri. *Journal of Environmental Science and Health, Part A*, 43(10):1167–1173, July 2008.

[92] M. G. de Morais and J. A. V. Costa. Carbon dioxide fixation by Chlorella kessleri, C. vulgaris, Scenedesmus obliquus and Spirulina sp. cultivated in flasks and vertical tubular photobioreactors. *Biotechnology Letters*, 29(9):1349–1352, September 2007.

[93] A. P. Carvalho, I. Pontes, H. Gaspar, and F. X. Malcata. Metabolic relationships between macro- and micronutrients, and the eicosapentaenoic acid and docosahexaenoic acid contents of Pavlova lutheri. *Enzyme and Microbial Technology*, 38(3):358–366, February 2006.

[94] Sigma-Aldrich. Ammonium hydroxide solution ACS reagent, 28.0-30.0% NH3 basis. Last accessed May 2020. URL https://www.sigmaaldrich.com/catalog/product/sigald/221228?lang=en&region=NO.

[95] VWR Chemicals. Ethanol 96% (v/v), TechniSolv®, pure. Last accessed May 2020. URL https://uk.vwr.com/store/product/2357969/ethanol-96-v-v-technisolv-pure.

[96] Sigma-Aldrich. Tetraethyl orthosilicate reagent grade, 98%. Last accessed May 2020. URL https://www.sigmaaldrich.com/catalog/product/aldrich/131903.

[97] A.G. Blackman, L.R. Gahan, G. Alyward, and T. Findlay. *Aylward and Findlay's SI chemical data*. John Wiley & Sons Australia, Ltd, 7th edition edition, 2014.

[98] B. N. Khlebtsov, V. A. Khanadeev, and N. G. Khlebtsov. Determination of the Size, Concentration, and Refractive Index of Silica Nanoparticles from Turbidity Spectra. *Langmuir*, 24(16):8964–8970, August 2008.

[99] PubChem. Citric acid. Last accessed May 2020, URL https://pubchem.ncbi.nlm.nih.gov/compound/Citric-acid.

[100] Sigma-Aldrich. Sodium citrate tribasic dihydrate ACS reagent 99.0%.

[101] B. E. Bonnelycke and W. B. Dandliker. Light scattering of colloidal silica. *Journal of Colloid Science*, 14(6):567–571, December 1959.

[102] E. D. Palik. *Handbook of Optical Constants of Solids*. Academic Press, 1997.

[103] T. A. Scott. Refractive Index of Ethanol–Water Mixtures and Density and Refractive Index of Ethanol–Water–Ethyl Ether Mixtures. *The Journal of Physical Chemistry*, 50(5):406–412, May 1946.

[104] W. K. W. Li. Temperature Adaptation in Phytoplankton: Cellular and Photosynthetic Characteristics. In P. G. Falkowski, editor, *Primary Productivity in the Sea*, Environmental Science Research, pages 259–279. Springer US, Boston, MA, 1980.

[105] NORCCA. Rhohomonas baltica NIVA-5/91. Last accessed May 2020, URL https://niva-cca.no/shop/cryptophyceae/rhodomonas/niva-5-91.

[106] R. R. L. Guillard and J. H. Ryther. Studies of marine planktonic diatoms: I: Cyclotella nana Hustedt, and Detonula confervacea (cleve) Gran. *Canadian Journal of Microbiology*, 8(2):229–239, April 1962.

[107] R. R. L. Guillard. Culture of Phytoplankton for Feeding Marine Invertebrates. In W. L. Smith and M. H. Chanley, editors, *Culture of Marine Invertebrate Animals: Proceedings — 1st Conference on Culture of Marine Invertebrate Animals Greenport*, pages 29–60. Springer US, Boston, MA, 1975.

[108] S. Kruszewski and M. Cyrankiewicz. Aggregated Silver Sols as SERS Substrates. *Acta Physica Polonica A*, 121(1A):A68–A74, 2012.

[109] L. Mikac, M. Ivanda, M. Gotić, T. Mihelj, and L. Horvat. Synthesis and characterization of silver colloidal nanoparticles with different coatings for SERS application. *Journal of Nanoparticle Research*, 16(12):2748, December 2014.

[110] W. Meng, F. Hu, X. Jiang, and L. Lu. Preparation of silver colloids with improved uniformity and stable surface-enhanced Raman scattering. *Nanoscale Research Letters; Heidelberg*, 10(1):1–8, February 2015.

[111] X. Dong, X. Ji, H. Wu, L. Zhao, J. Li, and W. Yang. Shape Control of Silver Nanoparticles by Stepwise Citrate Reduction. *The Journal of Physical Chemistry C*, 113(16):6573–6576, April 2009.

[112] A. M. Detweiler, C. E. Mioni, K. L. Hellier, J. J. Allen, S. A. Carter, B. M. Bebout, E. E. Fleming, C. Corrado, and L. Prufert-Bebout. Evaluation of wavelength selective photovoltaic panels on microalgae growth and photosynthetic efficiency. *Algal Research*, 9:170–177, 2015.

[113] L. Wondraczek, M. Batentschuk, M. A. Schmidt, R. Borchardt, S. Scheiner, B. Seemann, P. Schweizer, and C. J. Brabec. Solar spectral conversion for improving the photosynthetic activity in algae reactors. *Nature Communications*, 4(1):2047, 2013.

[114] S. Mohsenpour, B. Richards, and N. Willoughby. Spectral conversion of light for enhanced microalgae growth rates and photosynthetic pigment production. *Bioresource Technology*, 125:75–81, 2012.

[115] M. Atta, A. Idris, A. Bukhari, and S. Wahidin. Intensity of blue LED light: A potential stimulus for biomass and lipid content in fresh water microalgae Chlorella vulgaris. *Bioresource Technology*, 148:373–378, 2013.

[116] C.-H. Shu, C.-C. Tsai, W.-H. Liao, K.-Y. Chen, and H.-C. Huang. Effects of light quality on the accumulation of oil in a mixed culture of Chlorella sp. and Saccharomyces cerevisiae. *Journal of Chemical Technology & Biotechnology*, 87(5):601–607, 2012.

[117] C.-Y. Chen, Y.-C. Chen, H.-C. Huang, C.-C. Huang, W.-L. Lee, and J.-S. Chang. Engineering strategies for enhancing the production of eicosapentaenoic acid (EPA) from an isolated microalga Nannochloropsis oceanica CY2. *Bioresource Technology*, 147:160–167, 2013.

[118] R. Jin, Y.-W. Cao, C. A. Mirkin, K. L. Kelly, G. C. Schatz, and J. G. Zheng. Photoinduced Conversion of Silver Nanospheres to Nanoprisms. *Science*, 294(5548):1901–1903, November 2001. Publisher: American Association for the Advancement of Science Section: Report.

[119] N. Grillet, D. Manchon, E. Cottancin, F. Bertorelle, C. Bonnet, M. Broyer, J. Lermé, and M. Pellarin. Photo-Oxidation of Individual Silver Nanoparticles: A Real-Time Tracking of Optical and Morphological Changes. *The Journal of Physical Chemistry C*, 117(5):2274–2282, February 2013. Publisher: American Chemical Society.

[120] J. Shi, B. Xu, X. Sun, C. Ma, C. Yu, and H. Zhang. Light induced toxicity reduction of silver nanoparticles to Tetrahymena Pyriformis: Effect of particle size. *Aquatic Toxicology*, 132-133:53–60, May 2013.

[121] I. Ashdown. Photometry and Photosynthesis: From Photometry to PPFD (Revised). *Wordpress Blog*, November 2015.

[122] P. J. Lopez, J. Desclés, A. E. Allen, and C. Bowler. Prospects in diatom research. *Current Opinion in Biotechnology*, 16(2):180–186, April 2005.

[123] R. Ghosh Chaudhuri and S. Paria. Core/shell nanoparticles: classes, properties, synthesis mechanisms, characterization, and applications. *Chemical Reviews*, 112(4):2373–2433, April 2012.

[124] S. M. Bilankohi. Optical Scattering and Absorption Characteristics of Silver and Silica/ Silver Core/shell Nanoparticles. *Oriental Journal of Chemistry*, 31(4):2259–2263, December 2015.

Appendices

A Particles used for PSD determination in ImageJ

FESEM images used in the particle size distribution calculations in ImageJ has been combined with an overlay showing which particles was included in the analyses and their outlines. The basis for the PSD of SNP95, SNP192 and AgNP57 are given in Figures A.1, A.2 and A.3, respectively.

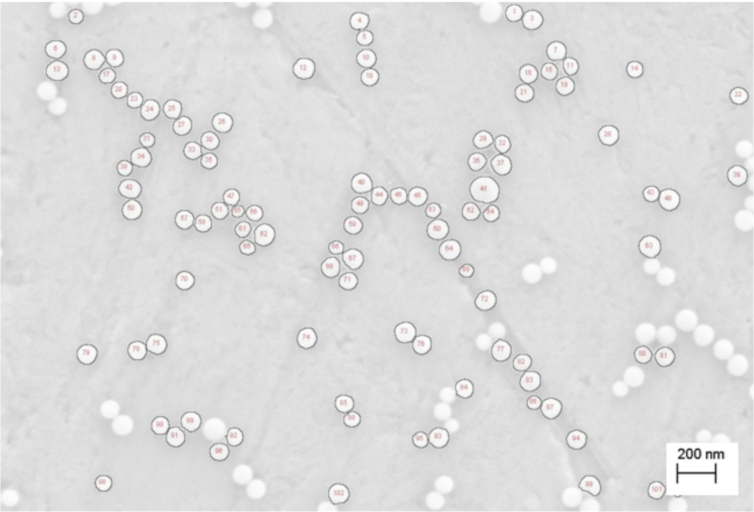

Figure A.1: Overlay of the particle circumferences used in the SNP95 PSD determination.

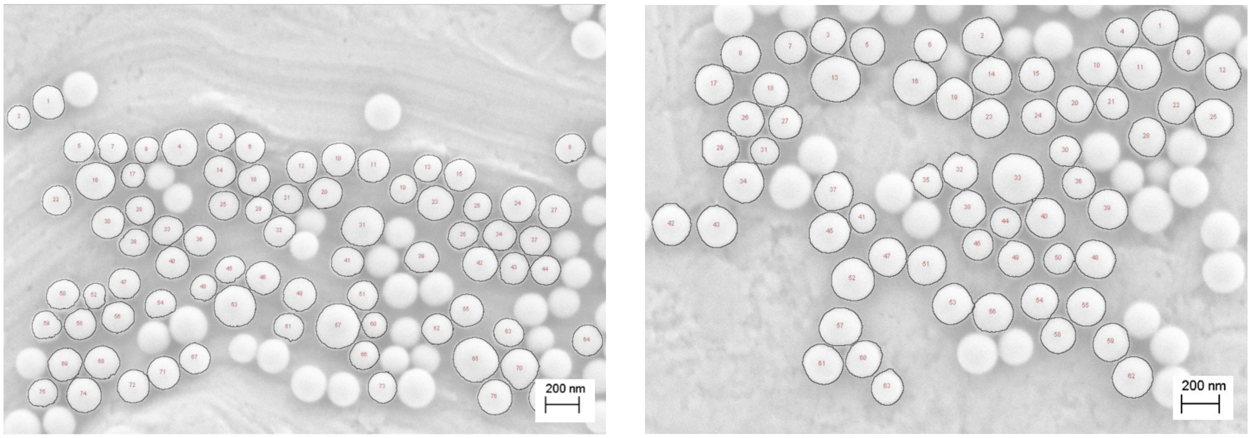

(a) **(b)**

Figure A.2: Overlay showing the particles used in the SNP192 PSD determination. Using two FESEM images, (a) and (b).

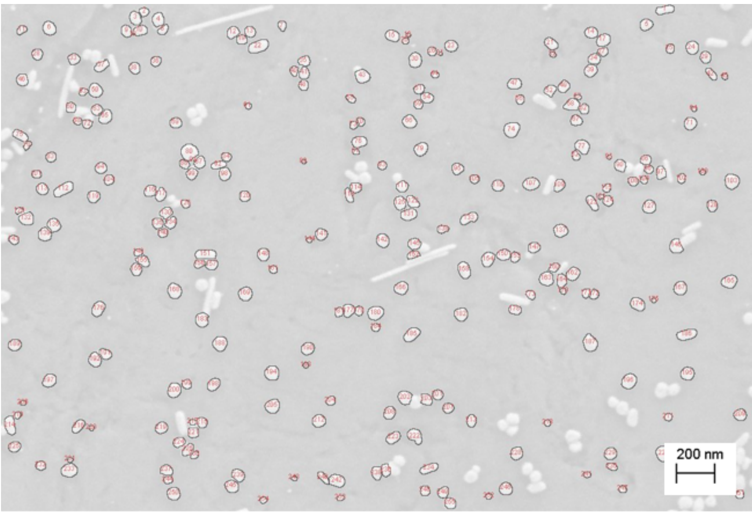

Figure A.3: Overlay of the particle circumferences used in the AgNP57 PSD determination.

B Calculation of NP concentrations

B. 1 Mass concentration of silver NPs

After heating 1 mL samples at 150°C for 1 hour, the mass was registered to determine the mass concentration of silver. Water, oxygen and nitric acid (HNO3) are removed from the samples at this temperature. Based on equation 2.23 and the boiling/decomposition temperatures in Table 3.5, sodium nitrate ($NaNO_3$) and citric acid ($C_6H_8O_7$) will also remain after heating. Assuming a complete reaction, silver nitrate is the limiting factor, hence any unreacted TSC ($Na_3C_6H_5O_7$) will also be present in the sample. To account for this, the weight percentage of Ag, w_{Ag} in the heat treated sample is calculated. First, the number of moles of silver nitrate reacted during synthesis, $n_{\text{AgNO}_3,0}$, is calculated.

$$n_{\text{AgNO}_3,0} = \frac{m_{\text{AgNO}_3,0}}{M_{\text{m}}^{\text{AgNO}_3}} \tag{1}$$

When $m_{\text{TSC,0}}$ is the mass of TSC added during synthesis, the total mass left after heating becomes

$$\begin{aligned} m_{\text{tot}} =& m_{\text{TSC}} + m_{\text{Ag}} + m_{\text{C}_6\text{H}_8\text{O}_7} + m_{\text{NaNO}_3} \\ & \left(n_{\text{TSC,0}} - \frac{1}{4} n_{\text{AgNO}_3,0} M_{\text{m}}^{\text{TSC}}\right) + n_{\text{AgNO}_3,0}\left(M_{\text{m}}^{\text{Ag}} + \frac{1}{4} M_{\text{m}}^{\text{C}_6\text{H}_8\text{O}_7} + \frac{3}{4} M_{\text{m}}^{\text{NaNO}_3}\right) \end{aligned} \tag{2}$$

and the mass fraction of silver, w_{Ag}, in the sample can be computed.

$$w_{\text{Ag}} = \frac{m_{\text{Ag}}}{m_{\text{tot}}} \tag{3}$$

For AgNP57, w^{Ag} = 0.30, based on the masses added during synthesis provided in section 3.2 and material properties in Table 3.5. Hence, the mass concentration of silver, $\text{c}_{\text{m}}^{\text{Ag}}$, is approximately 30$\%$ of the measured mass per mL in the samples after heating.

B. 2 NPs per cubic micron

From the obtained mass concentrations (directly from measured masses for the silica colloids, or as calculated in the previous section for silver) the number of NPs per cubic micron were calculated. First, the mean volume, V^{NP}, of the NPs were calculated from the mean diameter, d, obtained in the PSD analysis, assuming a perfect sphere.

$$V_{\text{NP}} = \frac{4}{3}\pi\left(\frac{d}{2}\right)^3 \tag{4}$$

Using the density, ρ, of silica (Table 3.2) or silver (Table 3.5), the mean mass of the NPs were calculated. For silver, this becomes

$$m_{\text{NP}} = V_{\text{NP}} \rho_{\text{Ag}}. \tag{5}$$

The number of NPs per unit volume (1 mL) was then calculated from the mass of Ag in the 1 mL samples, m^{Ag}, and divided by $10^{1}2$ to get the unit of cubic microns.

$$c = \frac{m_{\text{Ag}}}{m_{\text{NP}}} \frac{1}{10^{12}} \tag{6}$$

Similarly, the number of NPs per cubic microns are calculated for the silica sols.

C Aggregates observed in the AgNP#3 colloid

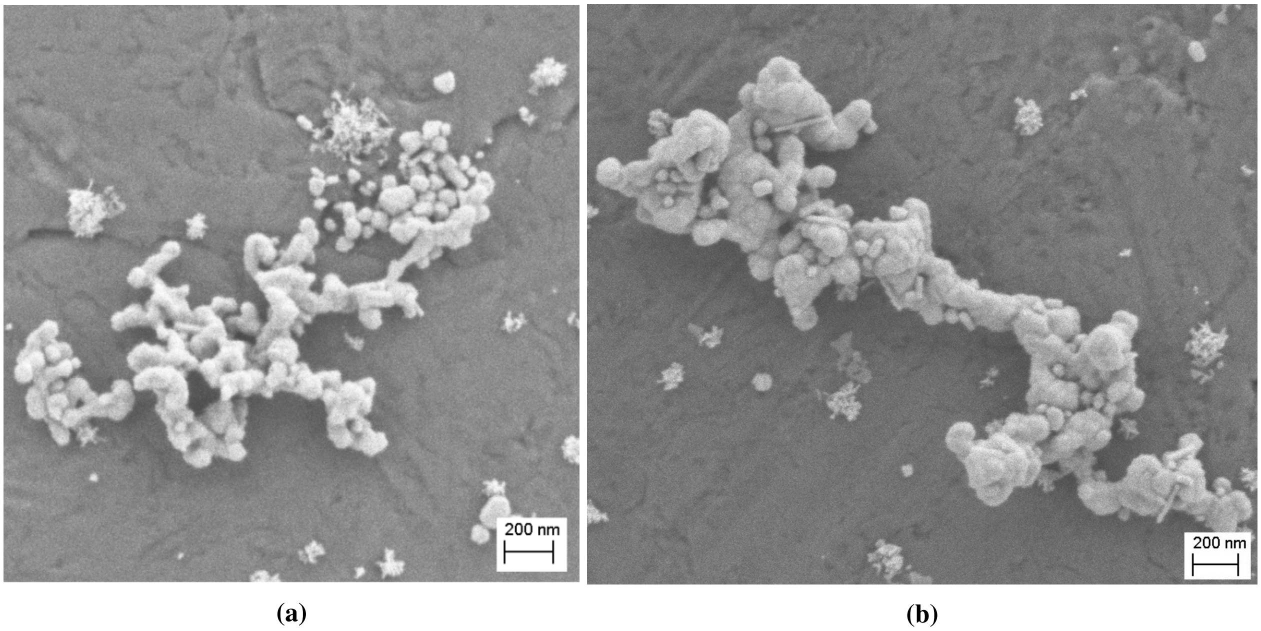

(a) (b)

Figure C.1: FESEM images of aggregated particles observed in the AgNP#3 colloid.

Maren Valestrand Tjønneland

Optimizing Microalgae Biomass Production; Using Nanomaterials for Enhanced Light Transport

NTNU
Kunnskap for en bedre verden